Multifunctional vertical interconnections of multilayered flexible substrates for miniaturised POCT devices

Multifunctional Vertical Interconnections of Multilayered Flexible Substrates for Miniaturised POCT Devices

BY

Xiaolong Zhang

A Doctoral Thesis

Submitted in partial fulfilment of the requirements for the award of

Doctor of Philosophy of Loughborough University

June 2016

Supervisor: Prof. Changqing Liu

Wolfson School of Mechanical, Electrical and Manufacturing Engineering

Loughborough University

CERTIFICATE OF ORIGINALITY

This is to certify that I am responsible for the work submitted in this thesis, that the original work is my own except as specified in acknowledgements or in footnotes, and that neither the thesis nor the original work contained therein has been submitted to this or any other institution for a degree.

…… (Signed)

20/11/2016

…… (Date)

Abstract

Point-of-care testing (POCT) is an emerging technology which can lead to an eruptive change of lifestyle and medication of population against the traditional medical laboratory. Since living organisms are intrinsically flexible and malleable, the flexible substrate is a necessity for successful integration of electronics in biological systems that do not cause discomfort during prolonged use. Isotropic conductive adhesives (ICAs) are attractive to wearable POCT devices because ICAs are environmentally friendly and allow a lower processing temperature than soldering which protects heat-sensitive components. Vertical interconnections and optical interconnections are considered as the technologies to realise the miniaturised high-performance devices for the future applications. This thesis focused on the multifunctional integration to enable both electrical and optical vertical interconnections through one via hole that can be fabricated in flexible substrates. The functional properties of the via and their response to the external loadings which are likely encountered in the POCT devices are the primary concerns of this PhD project.

In this thesis, the research of curing effect on via performance was first conducted by studying the relationship between curing conditions and material properties. Based on differential scanning calorimetry (DSC) analysis results, two-parameter autocatalytic model (Sestak-Berggren model) was established as the most suitable curing process description of our typical ICA composed of epoxy-based binders and Ag filler particles. A link between curing conditions and the mechanical properties of ICAs was established based on the DMA experiments. A series of test vehicles containing vias filled with ICAs were cured under varying conditions. The electrical resistance of the ICA filled vias were measured before testing and in real time during thermal cycling tests, damp heat tests and bending tests. A simplified model was derived to represent rivet-shaped vias in the flexible printed circuit boards (FPCBs) based on the assumption of homogenous ICAs. An equation was thus proposed to evaluate the resistance of the model. Vias with different cap sizes were also tested, and the equation was validated. Those samples were divided into three groups for thermal cycling test, damp heat ageing test

and bending test. Finite element analysis (FEA) was used to aid better understanding of the electrical conduction mechanisms. Based on theoretical equation and simulation model, the fistula-shape ICA via was fabricated in flexible PCB. Its hollow nature provides the space for integrations of optical or fluidic circuits. Resistance measurements and reliability tests proved that carefully designed and manufactured small bores in vias did not comprise the performance. Test vehicles with optoelectrical vias were made through two different approaches to prove the feasibility of multifunctional vertical interconnections in flexible substrates. A case study was carried out on reflection Photoplethysmography (rPPG) sensors manufacturing, using a specially designed optoelectronic system. ICA-based low-temperature manufacture processes were developed to enable the integration of these flexible but delicate substrates and components. In the manufacturing routes, a modified stencil printing setup, which merges two printing-curing steps (vias forming and components bonding) into one step, was developed to save both time and energy. The assembled probes showed the outstanding performance in functional and physiological tests.

The results from this thesis are anticipated to facilitate the understanding of ICA via conduction mechanism and provide an applicable tool to optimise the design and manufacturing of optoelectrical vias.

Keywords: Point-of-care testing, flexible substrate, vertical interconnections, Isotropic conductive adhesives, optical vias

List of Publications

1. **X. Zhang**, S. Hu, C. Liu, V. Azorin-Peris, and R. Imms, 'Electrically conductive adhesive enable to manufacture high performance patch probe for non-invasive physiological assessment', *Electronic System-Integration Technology Conference (ESTC), 2012 4th*. pp. 1–4, 2012.

2. A. Alzahrani, S. Hu, V. Azorin-Peris, R. Kalawsky, **X. Zhang**, and C. Liu, 'A novel yet effective motion artefact reduction method for continuous physiological monitoring', *Progress in Biomedical Optics and Imaging - Proceedings of SPIE*, vol. 8936, p. 89360G–89360G–16, 2014

Acknowledgement

From the start of my PhD study to the delivery of this thesis was a long and challenging journey. I would like to take this opportunity to express my sincere thanks to the people who have helped me in the process of my research.

I owe my deepest gratitude and appreciation to my supervisors, Prof. Changqing Liu, for providing me with the opportunity to pursue my PhD. His expertise, continuous support and patience have guided me in the way of my research. I would also like to thank Prof. Fengshun Wu from Huazhong University of Science and Technology (HUST), for his strong support when I was an exchange researcher in HUST. Besides, special thanks to my friends in both Loughborough and Wuhan. Without your help and company, my life in PhD study would be rather boring and miserable.

This research was supported by a Marie Curie International Research Staff Exchange Scheme Project within the 7th European Community Framework Programme, No. PIRSES-GA-2010-269113, entitled “Micro-Multi-Material Manufacture to Enable Multifunctional Miniaturised Devices (M6)”. And my thanks are also due to the Wolfson School of Mechanical, Electrical and Manufacturing Engineering of Loughborough University in support of my studentship.

Finally, I wish to express my sincere gratitude to my parents and my wife for their patience, encouragement, deep understanding and support. Their love is essential for me to finish this long journey and get ready for a new career.

Loughborough, UK Xiaolong Zhang

Table of Content

List of Tables

List of Figures

Glossary of Abbreviations

POCT	Point-of-care testing
RFID	Frequency Identification
EMI	Electromagnetic interferences
PCB	Printed circuit board
ICA	Isotropically conductive adhesive
FEA	Finite element analysis
OLED	Organic light emitting diodes
OPV	Organic photovoltaic
OTFTs	Organic thin film transistors
PPG	Photoplethysmography
LoC	Lab-on-chip
μTAS	Micro total analysis system
LED	Light emitting diodes
PI	Polyimide
PEEK	Polyetheretherketone
PES	Polyethersulphone
PEN	Polyethylene Naphthalate
PET	Polyethylene Terephthalate
CTE	Coefficient of Thermal Expansion
PTH	Plated-through hole
LANs	Local Area Networks
FSOI	Free-space Optical Interconnect
SOI	Silicon on insulator

WDM	Wavelength-division multiplexing
ECAs	Electrically conductive adhesives
ACA	Anisotropic conductive adhesive
ACF	Anisotropic conductive film
COG	Chip on glass
COF	Chip on flex
PMMA	Poly (methyl methacrylate)
IUPAC	International Union of Pure and Applied Chemistry
MMA	Methylmethacrylate
FPCB	Flexible printed circuit board
DSC	Differential scanning calorimetry
TG	Thermogravimetry
DTA	Differential thermal analysis
Tg	Glass transition temperature
DMA	Dynamic mechanical analyser
FE	Finite element
wt%	Weight fractions
SEM	Scanning Electron Microscope
DMF	Dimethyl Formamide
THF	Tetrahydrofuran
PD	Photodiode
CVD	Cardiovascular disease
WHO	World Health Organization

Chapter 1 Introduction

1.1 Research background

1.1.1 Flexible electronics in POCT device

Point-of-care testing (POCT) also called near-patient testing or out-of-laboratory testing. It is an analytical test undertaken at or near the site of a patient where is far from a hospital laboratory [1]. POCT aims to improve medical and economic outcomes and to shorten turnaround time (time from test order to patient treatment) [1]. POCT comes to use mainly due to the traditional diagnostic laboratory cannot meet the increasing demand by both the well and the sick to manage their health and feel good, by monitoring a variety of functions of the human body and activities related data (speed and acceleration) in daily lives, or during recovery from illness [1–3]. There are different kinds of POCT devices (Fig.1. 1), from networked bench-top multi-analyte instruments to simple hand-held glucose meters [2–4]. Light-weight and deformable flexible electronic circuits play an essential and critical role in the development of conformable sensors, bendable displays and other dynamic flexing applications. Many topics related to applications were researched, like multilayer flexible polymer circuit fabrication [5], integration of monitoring, recording and wireless communication functions on flexible substrates [6, 7]. Furthermore, a Paper-Based Frequency Identification (RFID) enabled sensing device was demonstrated by Georgia Institute of Technology [8]. There are both great needs and challenges for flexible electronics in POCT devices when it comes to integration into everyday items as well as miniaturising and shaping to fit the human body. POCT is expected to provide accurate, precise, and reliable results similar to the traditional laboratory testing that it is intended to replace [3, 9]. Therefore, the trend toward miniaturisation must be coupled with increased reliability of performance. Adding calibration and noise reduction modules [9] increases the packaging density and requires reliable fine pitch interconnections. The low-temperature manufacturing process is needed to maintain the performance of heat-sensitive sensing elements, such as electrodes in a uric acid test strip (80^{o}C) [10], electrochemical

biosensors (60°C) for nitrite quantification [11], and a polymer field effect transistor (65°C) for pH measurement [12].

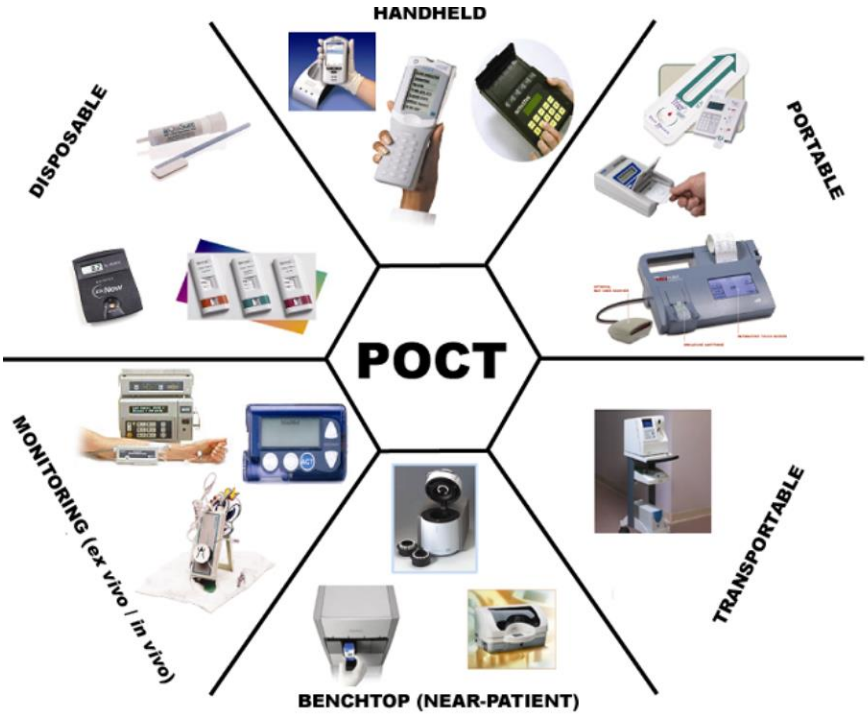

Fig.1. 1 Schematic catalogue of Point-of-Care Testing devices

1.1.2 Vias in flexible electronics

In electronic circuits, a via (path or road in Latin) is a conductive connection between different layers through a small opening in insulating layers. Therefore, via is also considered as the abbreviation for vertical interconnect access. There are limitations in interconnect density, bandwidth, signal integrity and thermal management with conventional technology. Vias enabled three-dimensional integration can effectively reduce the length of the chip to chip interconnection and help fulfil the call for increasing performance, shrinking size, saving power, and reducing cost [13–15].

Recently, printed electronics as a new class of flexible electronics are emerging to meet the growing demands of more flexible biomedical and industrial devices. It is an all-printed system on a flexible polymer substrate mainly include conductive circuitries, passive components and functional units such as chemical sensors, organic light emitting diodes (OLED), flexible displays, organic thin film transistors (OTFTs) and organic photovoltaic (OPV) solar cells [16–19]. When forming multi-layer conductive circuitry, addictive patterning process such as screen

printing or inkjet printing is used to print conductive patterns on each layer and fill vias for vertical interconnection between layers [20]. The vias in flexible substrates combine components with highly different materials properties: rigid vs. flexible. The electronic contacts at the interface will be subjected to very high tensile and shear deformations. The practical utility of vias in the flexible circuit has been developed despite the fact that little is known about the influence of mechanical stress induced by bending or rolling upon the electrical stability of the vias.

1.1.3 Isotropically conductive adhesive

Isotropically conductive adhesive (ICA) mainly consists of a polymeric resin (usually epoxy) that provides mechanical properties such as adhesion and mechanical strength, and conductive fillers (most commonly silver particles) that conduct electricity. ICA achieves electrical conductivity during the polymer curing process caused by the shrinkage of polymer binder and the removing of lubrication layers [21]. ICA is a promising alternative to tin-lead alloys solder. It equally provides electrical conductivity in all directions like alloy solder and offers many advantages over conventional solder technology. There are three significant ones:

- Environmentally friendly: Use of ICAs eliminates Lead and the flux in normal soldering processes [21]. Silver and epoxy are less toxic than Lead.
- Fewer processing steps: ICAs do not require flux and cleaning, thus offering a simpler and cheaper processing [22].
- Lower processing temperature: ICAs have low processing temperatures, usually in the range of 100-150^{o}C or even room temperature. Such low process temperatures provide great freedom in design, enabling the use of heat-sensitive and low-cost components and substrates [22, 23].

Due to these advantages, researchers are trying to apply ICA-based interconnects in POCT devices. An ICA was used to make the vertical electrical interconnects in the optical sensor array for wound monitoring [20]. UV-cure ICA was used to achieve room temperature bonding in a pH sensor [12].

1.1.4 Optical interconnects

Optical sensors are more attractive than their electronic counterparts in POCT applications due to several advantages: the resistance to harsh environments, the immunity concerning EMI (electromagnetic interferences), the high sensitivity and the non-contact mechanism [3, 24]. However, the use of optical sensors always implies the integration of a light source, sensors and electronic circuitry. The cost, size and reliability are the critical packaging problems [25–28] which hinder the implementation in many possible and practical applications.

1.2 Aim and objectives

Lightweight and thin flexible electronic circuits play an essential and critical role in the development of wearable miniaturised POCT devices. Conductive paste filling is a straightforward and effective solution for vertical interconnections in flexible electronics and embedded electronics. Moreover, optical interconnect is worth researching because of its great potential for reliable, high-performance optical sensing applications.

This PhD project was focusing on the multifunctional interconnects in flexible substrates to enable the miniaturisation of combined optical and electronic systems intended for POCT. Moreover, it was highly concerned that the functional properties of the micro-scale deposits of materials and their response to the external loadings or inputs to the systems which are likely encountered in the wearable POCT devices. The aim of this research are defined as below:

To research the integration of electrical and optical via in the flexible circuit by a low-temperature manufacturing technique, and investigate the performance, thermal reliability and bending durability of the via.

The detailed objectives to achieve the aim have been given as follow:

- Thoroughly literature review to gain an understanding of POCT technology, flexible electronics and interconnection technology.
- To research an ICA-based manufacturing technique that enables vertical electrical interconnection in flexible circuits.

- To develop a theoretical model to explain the effect of different parameters, such as via diameter, overlap area and thickness, on the electrical performance of via.
- To experimentally verify the factors on electrical performance and reliability of vias.
- To establish a feasible architecture of multifunctional vias, and fabricate optoelectrical vertical interconnects.

1.3 Structure of the thesis

Based on the research objectives, the structure of the thesis is established and presented in Fig.1. 2. The relationships between chapters are illustrated in the flow chart. A brief summary of each chapter is provided below.

Chapter 1 summarises the background of flexible electronics for POCT devices and identifies challenges and requirements related to interconnection in flexible electronics. The research aims and objectives are defined by those challenges and requirements. An overview of the thesis is presented at the end of this chapter.

In Chapter 2, a literature review was undertaken to gain knowledge of flexible electronics and interconnection technology. Different vertical interconnect technologies are summarised, to identify the strengths and novel features of the technique developed in this thesis. The materials, theories and techniques used in following chapters are also reviewed in detail.

Chapter 3 gives an insight into the geometry effect on conduction within the ICA vertical interconnects. The important geometry factor which would be expected to affect the electrical resistance of the vias is identified by finite element analysis and theoretical calculation. A whole set of manufacturing processes was developed to produce the test vehicles. Temperature cycling test, damp heat test and bending test were conducted to investigate the robustness and reliability of the vias.

In Chapter 4, the relationship between curing condition and vias performance was researched. Cure kinetic model of as-received ICA materials was established to guide the design of curing parameters. Resistances of ICA vias cured under selected conditions were measured before and in real time during temperature cycling test, damp heat test and bending test.

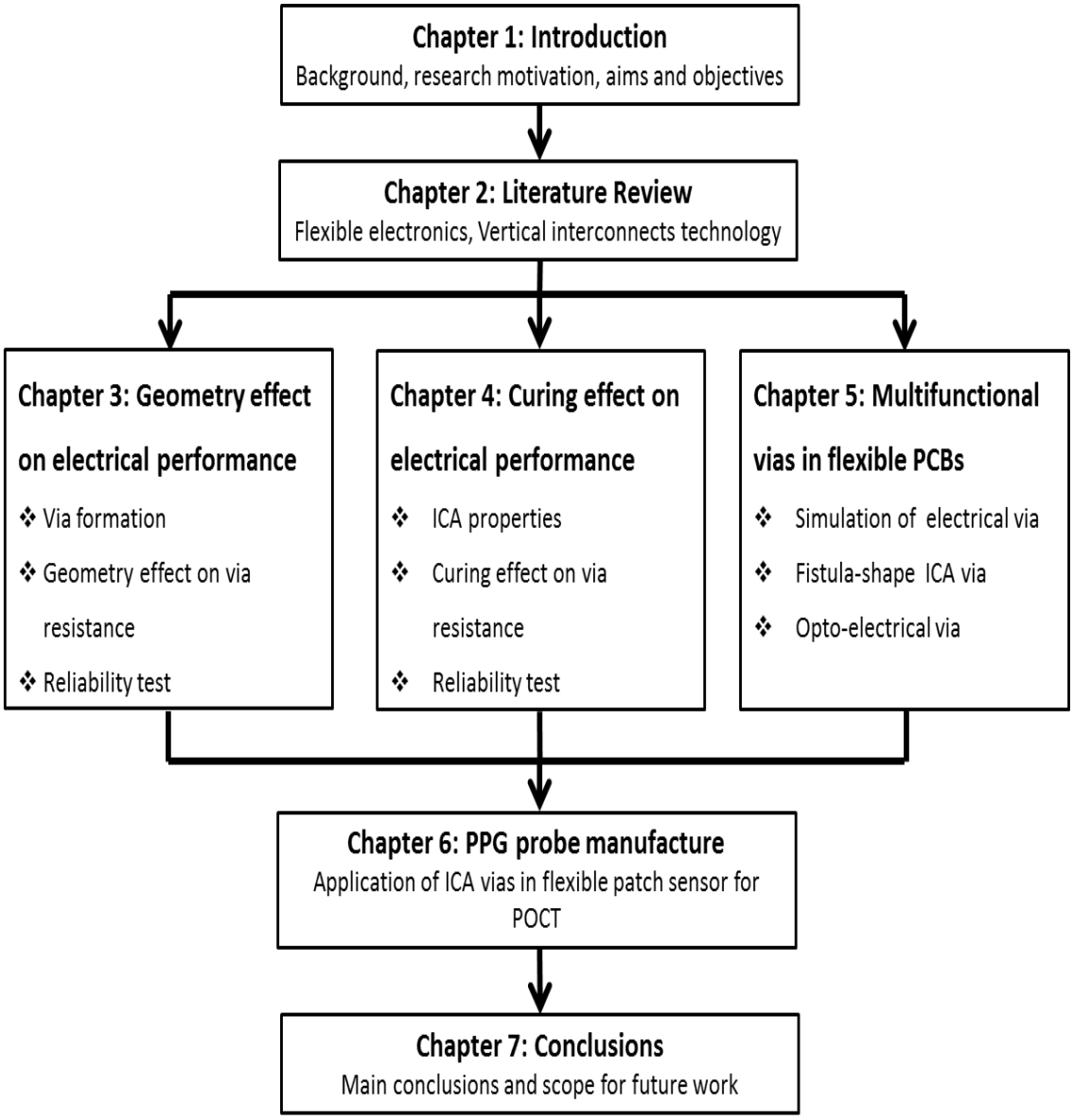

Fig.1. 2 Overview of the thesis structure.

The feasibility of multifunctional vertical interconnects in flexible substrates was investigated in Chapter 5. Firstly, the concept of fistula-shape ICA via was proposed, since its hollow nature provides the space for integrations of the optical or fluidic circuit. Moreover, finite element model of fistula-shape ICA via was built to aid the design of vias. Then fistula-shape ICA vias were manufactured by mechanical drilling into solid vias. Finally, optoelectrical vertical interconnections were achieved by the integrating optical vias into the fistula-shape ICA vias.

Chapter 6 presents a case study where Photoplethysmography (PPG) sensor using specially designed optoelectronic sensor was assembled on flexible PCB by ICAs. A low-temperature manufacture route was established to realise the design and ensure the reliability of

performance. Electrical test and physiological assessments of the optoelectronic sensor are also presented in this chapter.

Finally, Chapter 7 summarises the main conclusions of the work presented in this thesis and provides recommendations for future work.

Chapter 2 Literature review

2.1 Point-of-care testing and Photoplethysmography

Point-of-care testing (POCT) also called near-patient testing or out-of-laboratory testing. It is an analytical test undertaken at or near the site of a patient where is far from a normal hospital medical laboratory [1]. POCT comes to use mainly due to the traditional diagnostic laboratory cannot meet the increasing demand by both the well and the sick to be informed and active participants in their health maintenance and the management of their illnesses [2, 3]. POCT provides a quick and convenient solution for a variety of clinical settings, for example, the operating theatre, critical care unit, maternity unit, outpatient clinic, emergency department and disaster response [2]. It aims to improve medical and economic outcomes, and to shorten turnaround time (time from test order to patient treatment) [1]. There are different kinds of POCT devices, from networked bench-top multi-analyte instruments to simple hand-held glucose meters [2, 3] Table.2.1 shows the different tests that POCT device can conduct. Delivering reliable results when used correctly by personnel not trained in clinical laboratory practice is an essential requirement if the POCT devices are used for sports or home care. An ideal POCT device should be the optimisation of cost, accuracy and reliability, storage and handling, data quality and medical implications [1].

Table.2. 1 Examples of point-of-care tests

Sample	Examples
Whole blood	Glucose, troponin I, blood gases, activated clotting time, platelet function
Urine	β HCG (pregnancy test), glucose, ketones, nitrites
Faeces	Occult blood
Saliva	Nicotine metabolites, drugs of abuse
Exhaled breath	Ethanol, basic spirometry
Other	electrocardiogram, temperature

Source [1]

POCT devices collect clinical parameters through three main detection methods: optical methods, electrochemical methods, and mass spectrometry methods. Among these methods, electrochemical and optical methods are the most frequently utilised due to their selectivity and sensitivity [29, 30]. Not like embedded electrochemical sensors, optical sensors can be non-contact and reusable, which broaden the application of optical methods. Typical optical detection methods comprise the light property modulation detections and the direct detection by monitoring the light properties including fluorescence, absorbance, and luminescence-based methods [30].

Fig.2. 1 Optical Workstation at Lawrence Livermore National Laboratory, United States [31]

While microscopes, lasers, spectrophotometers, lenses, and filters can be precisely arranged and aligned in a lab (Fig.2.1) [30, 32, 33], such a system is hard to miniaturise into a low-cost, portable, and robust device for POCT. Thanks to the rapid development of low-cost and high-performance optoelectronics like CCD cameras, laser diodes, photodiodes, light emitting diodes (LED), as well as recent innovations in microfluidic integration and nanoscale materials. The optical detection methods are becoming more practical for Point-of-Care diagnostics. Many groups have shown good results with LED-induced fluorescence by incorporating integrated lenses, waveguides and filters into their microfluidic designs [33]. Onur Mudanyali *et al.* demonstrated a compact and lightweight digital rapid-diagnostic-test device based on LED

illumination and cell phone camera. Inserted test strips can be imaged in reflection or transmission modes [34].

Photoplethysmography (PPG) is a simple and low-cost optical technique which is used to detect blood volume changes in the microvascular bed of tissue [35]. The basic form of PPG technology requires only a few optoelectronic components: a light source to illuminate the tissue (e.g. skin), and a photodetector to measure the small variations in light intensity passing through or reflected from skin tissue [35, 36]. PPG is most often employed non-invasively and operates at a red or/and a near infrared wavelength. The most recognised PPG waveform feature is the peripheral pulse, which is synchronised to each heartbeat [35–37]. While the absorbance of some tissues (e.g., bone, muscle) is a constant and can be termed as the DC component of the PPG signal, the absorbance of arterial blood pulsations can be considered as an AC component. PPG signals reflect the pulsatile action of arteries through the interaction between oxygenated haemoglobin and photons. These photon-tissue interactions should present a unique pattern for each individual [36]. After decades of development, the PPG device has moved from torch bulb to advanced optoelectronics and has a widespread clinical application, for example, pulse oximeters, vascular diagnostics and digital beat-to-beat blood pressure measurement systems [37]. A lot of miniaturised devices using PPG technology have been developed, like wireless finger clip PPG probe [38], ear-worn heart rate monitoring patch [39], Ankle Systolic Pressure Measurement cuff [40], wristwatch-type heart rate monitoring device [41, 42], Finger-Ring PPG sensing device [43]. Moreover, now the PPG technology is moving on towards the imaging PPG [44–46] and 3D imaging PPG [47].

2.2 Flexible electronics

Flexible electronics are emerging as important applications for future displays [48, 49], robotics [50], in vivo diagnostics [51–53], advanced therapies [54, 55] and energy harvesting [49, 56].

The materials and technologies behind flexible substrates are an important consideration for flexible electronics. The use of these substrates can significantly reduce the overall substrate thickness and weight and most of all they can ease the assembly [4–7], increase the module compactness and can be applied to a flat, a curved and even to a dynamic surface. The flexible substrates also open the way to roll-to-roll fabrication techniques [4], increasing the process

throughput and reducing the cost of fabrication [6, 20]. Besides of the lightweight and deformability, substrates need to be solvent resistant to survive the standard optical photolithography process. Additional requirements for substrates include moisture resistance and low cost (allowing large area, mass production). Table.2.2 compares some of the most critical properties of some key plastic substrates [57, 58]. One of the main challenges for plastic as a next generation substrate is the substantially reduced processing temperature window. The maximum processing temperature, shown in Table.2.2, is related to the glass transition temperature (Tg) above which inelastic deformation takes place, and the substrate no longer retains its original dimension.

Table.2. 2 Comparison of plastic substrates.

T_{Max} (°C) *	Material	Properties
250	Polyimide (PI)	Expensive, high CTE**, good chemical resistance, orange colour, high moisture absorption
240	Polyetheretherketone (PEEK)	Expensive, good chemical resistance, amber, low moisture absorption
190	Polyethersulphone (PES)	Expensive, good dimensional stability, poor solvent resistance, clear, moderate moisture absorption
160	Polyethylene Naphthalate (PEN)	Inexpensive, moderate CTE, good chemical resistance, clear, moderate moisture absorption
120	Polyethylene Terephthalate (PET)	Inexpensive, moderate CTE, good chemical resistance, clear, moderate moisture absorption

*T_{Max}: a maximum processing temperature, **CTE: the Coefficient of Thermal Expansion

2.3 Electrical vertical interconnects

In electronic circuits, a via is a conductive connection between different layers through a small opening in insulating layers. Via is also considered as the abbreviation for vertical interconnect

access. Demands for increasing performance, smaller size, reduced power, and reduced cost cannot be met with conventional packaging and interconnect technologies. There are limitations in interconnect density, thermal management, bandwidth, and signal integrity with conventional technology [59]. Vias enabled three-dimensional integration can effectively reduce the overall length of interconnects and fulfil the requirements above [60, 61]. There are several methods of via hole formation, such as mechanical drill or punch [62, 63], laser drill [63–65], photolithography [66, 67] and plasma-etching [68]. Aside from the variety of methods utilised to form vias in the dielectric layers, metallisation of these vias can also be accomplished by several techniques.

The most commonly used via filling technologies in the PCB industry are based upon electroplating or filling with conductive pastes [14, 61, 69]. The drawback of electrodeposited copper in the vias is the potential cracking of the very thin copper layer coated on the via sidewalls[70, 71]. The significant coefficient of thermal expansion (CTE) differences between barrel copper and the surrounding dielectric material within the plated-through hole (PTH) results in major reliability concerns under thermal loading. Once the thermo-mechanical stresses due to the mismatch of the CTE exceeds the limit of the plated barrel copper strength, failures such as circumferential barrel cracks, land corner cracks and pad lifting occur [69, 70]. Moreover, the environmentally hazardous chemicals are used during such plating processes [72].

Conductive pastes which use silver or other conductive particles have been used to make solid vias which electrically interconnect circuit layers. This process is environmentally friendlier than plated through-hole process, and the cost of facilities is very low [73]. Conductive pastes filled vias have a relatively high electrical resistance compared with plated through holes because filled paste has significantly higher resistivity and contact resistance than plated metal layer [72] [73]. Screen printing is most commonly employed to fill the paste since it is a quick and cost-effective additive patterning process which is often available from existing PCB producer [62, 73]. Researchers are now put great interest in inkjet printing method in order to miniaturise the vias and move forward to printed electronics [65, 74, 75].

2.4 Optical interconnects

Optical signals have got very high carrier frequencies (200-1000 THz for corresponding free-space wavelengths of 1.5 μm to 300 nm) as opposed to the electrical signals [76–78]. The short wavelength of light allows the use of dielectric waveguides to guide the optical signal. Therefore, optics avoid the metal waveguides that are essential for confining the radio-frequency waves of electrical interconnections and hence also avoid the resistive loss physics that dominates the propagation loss and distortion of electrical lines [77–80]. Frequency-dependent cross-talk and reflection can be avoided by high-speed modulation of optical beams [77, 81]. From a transmitter to a receiver, the efficiency of optical transmission is affected by connector loss, splice loss and attenuation in transmission medium [82, 83]. Within the optical material, the attenuation is caused by absorption (intrinsic and extrinsic absorption), scattering (Rayleigh and Mie scattering) and bending (macro- and micro- bending) [82]. In principle, all attenuation mechanisms can be traced back to the multi-length scale structure of the material itself (e.g. atomic structure, point defects, second-phase inclusions) or structures arising from the fabrication and design [82, 84, 85]

At the long end of the interconnect hierarchy such as in the long-haul (telecom) and Local Area Networks (LANs), the optical fibre has already replaced the electrical cables. However, at the lower end of the hierarchy such as in the card to card, board to board, chip to chip and on-chip levels, copper based electrical wires still dominate [76–80]. In the past three decades, various groups in academic and industries have vigorously researched different ways of implementing optical interconnection in board-to-board, chip-to-chip and even in intra-chip levels. Figure 2.2 illustrates distance ranges for various interconnects and preferred optical techniques for implementing them [86]. Although a large number of architectures have been proposed for optical interconnects, most of them fall into one of the following two categories [78, 87–90], as follows:

• Free-space Optical Interconnect (FSOI) System

• Guided-wave Optical Interconnect System

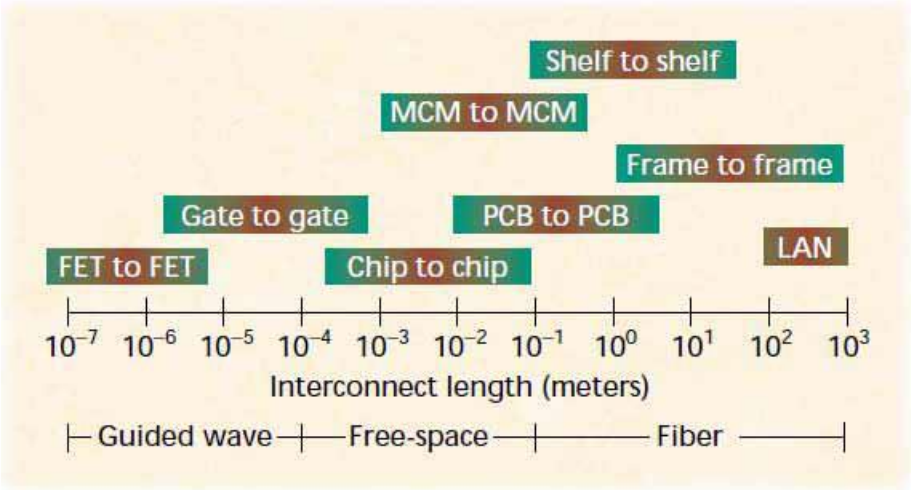

Fig.2. 2 Distance ranges required for various interconnects and preferred optical techniques for implementing them

In free space optical interconnects, light propagates from source to detector through a bulk medium. Lenses, mirrors and holograms are the typical passive optical elements to provide a communication channel for free-space interconnects. Such interconnection has the capacity for high interconnection density but has disadvantages including the need for 3D alignment between detectors and signal beams and high diffraction related cross-talk [91]. Free-space optical interconnections have been found very suitable for chip to chip and board level interconnects because of (i) the potential to fully utilize the large spatial bandwidth and parallelism of optics, (ii) no mutual interference (light beams can cross in space with no interference), (iii) flexible networks since they are not connected to physical paths, and most of all, (iv) the abllity of using simple imaging optics which produces light-power efficiency, very low signal skew, simpler architectures, and permit chip-like integration [86, 92].

In guided-wave optical interconnects, optical fibres/waveguides integrated into the planar substrate, are used as the main physical paths for the optical signals to travel on- and off-chip. Micro-mirrors fabricated at the transmitting/receiving ends may be used to direct the optical signal from light sources into fibres/waveguides or direct optical signal onto photodetectors [93]. The major drawbacks of fibre/waveguide based systems at the chip to chip and board levels are the relatively low interconnection density, cross-talk between adjacent waveguides, severe coupling losses, and losses due to bending and looping of fibre [82, 94]. For integrated waveguides, an important problem is the coupling of light into and out of the waveguides due to

reflection loss in each interface. Additionally, the density of a waveguide array is mainly limited by the coupling-induced cross-talk between adjacent waveguides [78, 95]. Moreover, both fibre-based and waveguide integrated optical interconnects at the chip to chip and board levels have very limited interconnectivity and fan-in/fan-out channels since they are much like wires and require physical paths between every two points. Fortunately, use of submicron size silicon waveguides using silicon on insulator (SOI) technology [96], and wavelength-division multiplexing (WDM) [97, 98] can alleviate the problem of density and can provide high bandwidth required for future generation integrated circuit systems.

2.5 Materials for vias

2.5.1 Electrically conductive adhesives (ECAs)

Electrically conductive adhesive (ECA) is a promising alternative to tin-lead alloys solder [21–23] and via filler material [72, 73]. They consist of a polymeric resin (e.g. epoxy, silicone, or polyimide) that provides mechanical properties (e.g. adhesion, mechanical strength, and impact strength) and conductive fillers (e.g. silver, gold, nickel or copper particles) that conduct electricity. Electrically conductive adhesives possess many advantages over conventional solder technology. They are environmentally friendly, require fewer processing steps (reducing processing cost), and allow a lower processing temperature (enabling the use of heat-sensitive and low cost components and substrates) and smaller distances between the electrical lines in circuits (enabling the manufacture of smaller devices), greater creep resistance and energy damping [21–23, 99, 100].

ECA can be categorised into two main kinds: anisotropic conductive adhesives (ACAs), sometimes in a film form, called anisotropic conductive film (ACF) and isotropic conductive adhesives (ICAs), which are shown in Fig.2.3 [21].

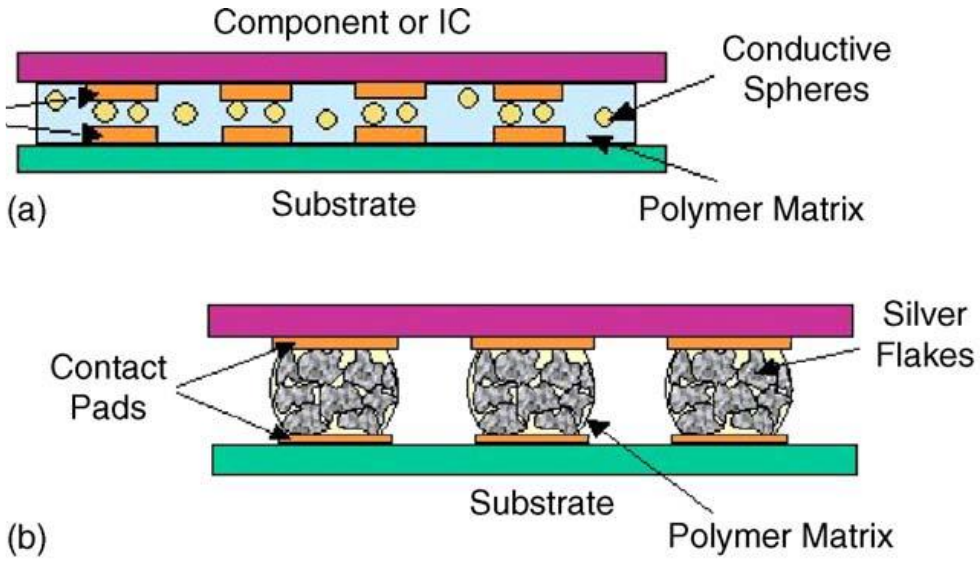

Fig.2. 3 Schematic illustrations of (a) ACA and (b) ICA

The difference between ACA and ICA is based on the percolation theory of conductive filler loading level. The percolation threshold depends on the shape and size of the fillers, but typically in the order of 15–25% volume fraction [21]. For ICAs, the loading level of conductive fillers exceeds the percolation threshold, providing electrical conductivity in all directions. ICAs achieve electrical conductivity during the polymer curing process caused by the shrinkage of polymer binder [21, 23]. While for ACA/ACF, the low volume loading is insufficient for inter-particle contact and prevents conductivity in the X–Y plane of the adhesive. Therefore, they provide a uni-directional electrical conductivity in the vertical or Z-axis. The conductive particles in ACAs/ACF bridge the two conductor surface when pressure is applied with heat treatment. Because of the anisotropy, ACA/ACF may be deposited over the entire contact region, an ultra-fine pitch interconnection (<0.04 mm) could be achieved easily [21]. Both adhesive types can be adapted as interconnection materials for surface mount technology processes, such as flip–chip bonding, chip on glass (COG) and chip on flex (COF) technologies in electronic packaging industries [21–23].

Main limitations of current ECAs like limited current carrying capability, poor impact resistance, unstable contact resistance and poor mechanical strength in various climatic and environmental conditions are major obstacles which prevent ECAs from becoming a general replacement for solders in electronic applications [21–23, 99–101]. Recently, some progress has been made in clarifying the mechanisms underlying the conductivity fatigue and the limited current-carrying

capability of conductive adhesives. Because galvanic corrosion is the main cause of conductivity fatigue, oxygen scavengers, corrosion inhibitors, and sacrificial additives (alloys with lower corrosion potential) have been used to stabilise the contact resistance and improve the reliability of conductive adhesives [21, 102, 103]. To enhance the current-carrying capability of conductive adhesives, self-assembled monolayers with high current density were incorporated into the interface between metal fillers and substrates; the electrical conductivity and current-carrying capability of the resulting adhesives can compete with those of traditional solder joints [21, 99]. Another critical property for electronic components is able to withstand impacts generated by, for example, dropping, strong vibration, or mechanical shock. Most commercial ICAs have poor impact strength due to their high filler loading [104]. Thus, components that are assembled with conductive adhesives tend to separate from the substrate upon being subjected to a sudden shock [101, 104]. The impact strength of conductive adhesives may be increased by simply decreasing the filler loading [21]. However, such a process reduces the electrical conductivity of the conductive adhesives due to percolation threshold. A Recent development was reported that impact performance is closely related to damping property [105]. Conductive adhesives were developed using resins of low Young's modulus to absorb the impact energy developed during the drop [105]. However, the glass transition temperature (Tg) of these adhesives reduced to below room temperature. Furthermore, elastomer-modified epoxy resins with enhanced loss modulus (high tan delta values) were also used to enhance the damping properties and the impact performance of ICAs [106].

2.5.2 PMMA

Poly (methyl methacrylate) (PMMA), having the IUPAC (International Union of Pure and Applied Chemistry) name of poly [1-(methoxycarbonyl)- 1-methyl ethylene] from the hydrocarbon standpoint, and poly (methyl 2-methylpropenoate) from the ester standpoint, is a synthetic polymer from the methylmethacrylate (MMA) monomer as illustrated in Figure 2.4 [107].

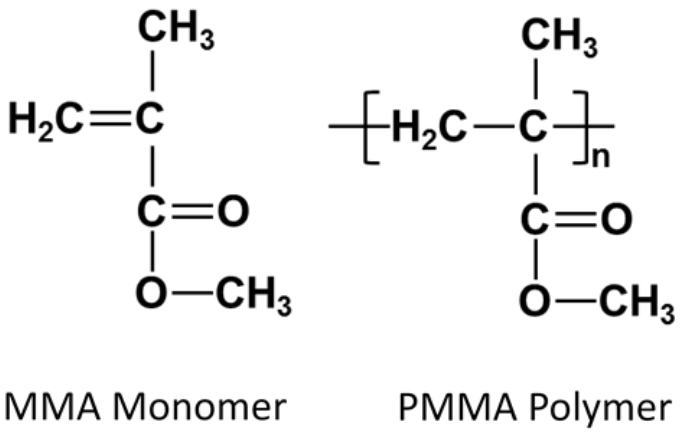

Fig.2. 4 The structures of MMA and PMMA

PMMA possesses very good optical properties, with a refractive index of 1.490, and a good degree of compatibility with human tissue [107]. It also has very good thermal stability and is known to withstand temperatures as high as 100 ^{o}C and as low as -70 ^{o}C [108]. In the field of mechanical strength, PMMA has a high Young's Modulus and a low elongation at breakage which make it one of the hardest thermoplastics with high scratch resistance [107, 109]. This polymer has a reasonable resistance to chemicals, being unaffected by the aqueous solution of most laboratory chemicals. However, it has a low resistance to chlorinated and aromatic hydrocarbons, esters, or ketones [108, 109].

PMMA is one of the amorphous polymers that belong to the acrylate family. It is a clear, colourless polymer with a glass transition temperature range of 100 ^{o}C to 130 ^{o}C, and a density of 1.20 g/cm3 at room temperature. This polymer melts at 130 ^{o}C, with a water absorptivity of 0.3%, moisture absorption at equilibrium of 0.3 to 0.33%, and a linear shrinkage mould of 0.003 to 0.0065 cm/cm [108–110]. Commercial PMMA is the cross-linking mixture of isotactic PMMA/ syndiotactic PMMA, atactic PMMA/ syndiotactic PMMA, and atactic PMMA/ isotactic PMMA. Sometimes, a copolymer of plasticiser/PMMA, with the highest percentage of PMMA, is used just to make it more flexible for wider applications. Therefore, the properties of commercial PMMA, such as glass transition temperature (Tg) and solubility vary widely [111, 112].

2.5.3 Optical fibre

Optical fibre is usually composed of a core material and a cladding material. The optical property that keeps the signal in the core is total internal reflection caused by a difference in

optical refractive index between two materials [84, 98]. There are two main types of fibre: single-mode, with a core diameter of approximately 7μm; and multimode, with a core diameter of 50μm or larger [85, 98]. Single-mode fibre has a higher bandwidth than multimode because the light can only travel in a single mode (or 'pathway') within the core. Multimode fibre can allow tens to hundreds of different modes in one core. The advantage of the smaller core size is a higher bandwidth for longer-distance transmission or higher data rate while the disadvantage is more demanding assembly tolerances [82, 85].

Plastic fibre has been available for many years. It has many advantages over the glass like cost and ease of connection [85], except the optical attenuation (loss per metre) performance. For example, PMMA plastic fibre has an attenuation of 150 dB/km at 650 nm [82]. So plastic fibre is not suitable for long-distance use. However, there has been a lot of progress, which may allow more broad deployment of plastic fibre over short distances, either within the home or to directly connect integrated circuits [113].

Various loss mechanisms introduce losses in an optical fibre [82], including absorption, scattering, dispersion and bending. Because the former three are governed by fibre materials, manufacturing process and light source, they are considered as constants in the testing system. The cause of fibre bending loss [82] is shown in Fig.2.5. When the fibre is bent, the part of the optical signal, which no longer meets the total reflection conditions, is transmitted from the fibre core to the cladding and then lost. It can be divided into macro-bending loss and micro-bending loss [82]. The macro-bending loss of polymer optical fibre is caused by the bending of the fibre axis. The micro-bending loss of polymer optical fibre is caused by small-scale bending or distortions. The micro-bend may be produced in the manufacturing process, which occurs randomly along the fibre axis. Some micro-bending losses may be temperature related, tensile related or crush related and they are reversible once the cause is removed. Therefore, theoretical analysis of micro-bending loss is difficult to make, which has much uncertainty [114, 115]. Taking the feasibility of experimental conditions into account, the following major research is macro-bending loss, referred to as bending loss.

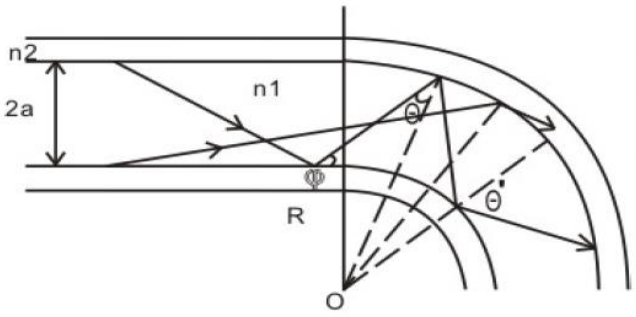

Fig.2. 5 The schematic diagram of macro-bending of optical fibre

According to D.Marcuse's theory [115], when the bending radius of bending fibre is R, the bending loss coefficient is:

$$2\alpha_B = \frac{\sqrt{\pi}u^2}{e_m W^{3/2} V^2 \sqrt{R} K_{m-1}(Wa) K_{m+1}(Wa)} \exp[-\frac{2}{3}(\frac{W^3}{\beta^2} R)]$$

(when m=0,e_m=2; when m≠0, e_m=1) 2.1

After the specific fibre and light source are selected, in addition to bending radius R, the other parameters are constants. D.Marcuse's formula can be simplified to

$$2\alpha_B = A\frac{\exp(B \cdot R)}{\sqrt{R}} \quad 2.2$$

$A = \frac{\sqrt{\pi}u^2}{e_m W^{3/2} V^2 K_{m-1}(Wa) K_{m+1}(Wa)}$ and $B = -\frac{2W^3}{3\beta^2}$ are both constants, which can be determined by the selected system.

It can be concluded from Equation 2.2: the bending loss of fibre is inversely proportional to the bending radius.

2.6 Thermal analysis

Defined by ICTAC (the International Confederation for Thermal Analysis and Calorimetry), Thermogravimetry (TG) is an experimental technique in which the mass change of a substance is measured as a function of temperature while the substance is subjected to a controlled

temperature programme [116]. TG curves are recorded by using a thermobalance [117]. A schematic illustration of a thermobalance is shown in Fig.2.6.

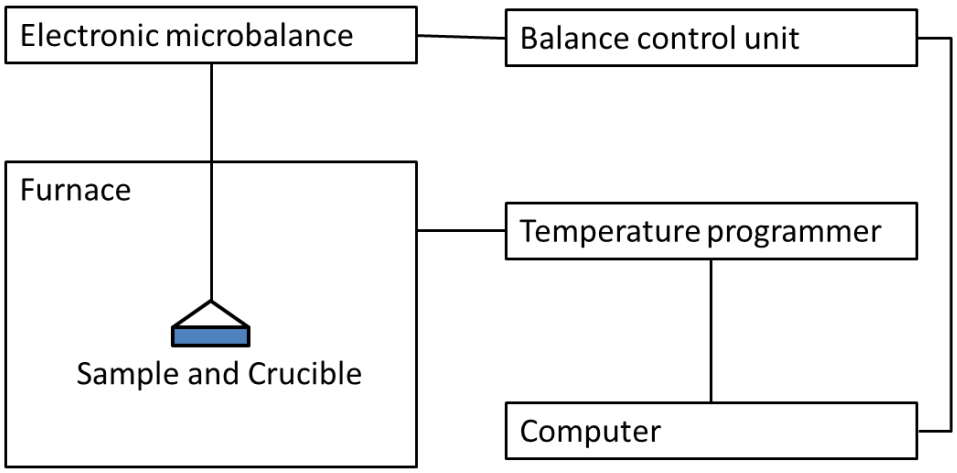

Fig.2. 6 Schematic diagram of thermobalance system

The reaction represented in TG curve appears to cover a range of temperature, because the reaction in the solid state is relatively slow and the temperature is always rising with respect to time. The steepest mass loss is only the point where the reaction is the fastest and doesn't indicate the start of the reaction. Ideally, the heating rate should be low so that reaction can take place over a narrow range of temperature. The sample size should be as small as possible and should be spread evenly and thinly.

There are, of course, reactions that may involve no mass change. These can be detected by differential thermal analysis (DTA) and differential scanning calorimetry (DSC). These techniques are based on a simple concept: to obtain information on thermal changes in a sample by heating or cooling it along with an inert reference [116]. Fig.2.7 is a schematic representation of DTA/DSC apparatus. There are four major parts: 1) DTA/DSC sensors and amplifier, 2) the furnace and its temperature sensor, 3) the programmer and 4) the recorder or data acquisition device.

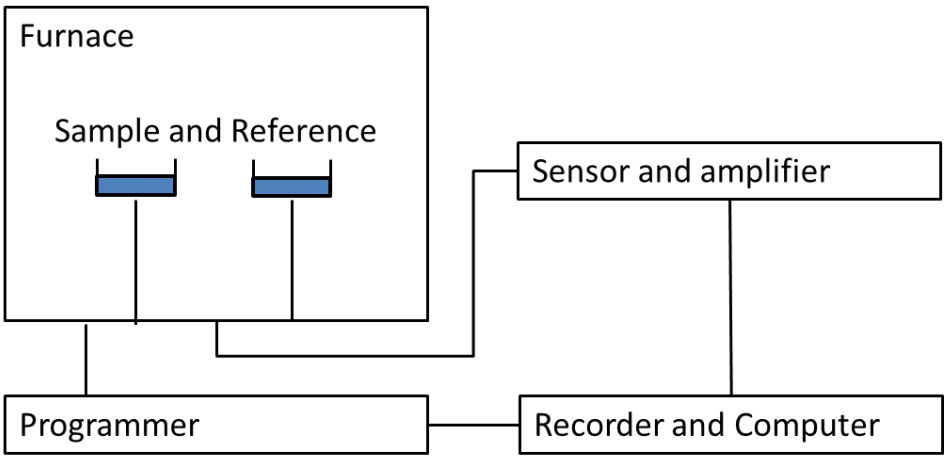

Fig.2. 7 Schematic diagram of DTA/DSC apparatus

The difference between DTA and DSC is the signal obtained from the equipment. The DTA monitors the difference in temperature between the sample and reference, while the DSC records the difference in heat flow (power) [116, 117] There are mainly two types of DSC [116]:

Power-compensation: the sample and reference are separated from each other and have their own individual heaters and temperature sensors. The temperature difference between the sample and reference is eliminated by supplying differential thermal power.

Heat flux: the sample and the reference are heated by the same heater, and the temperature difference is measured. Then the temperature difference is converted into a power difference by the built-in algorithm.

DTA and DSC are qualitative tools but also can be used as a quality analyser for identifying substances. DTA/DSC is applied to study a wide range of materials (Table 2.3) [116], and especially useful in the investigation of polymeric materials with curing processes, glass transitions, crystallinity and melting behaviour and polymerisation [116, 118].

Table.2. 3 Materials studied by DTA and DSC

Polymers, glasses and ceramics	Oils, fats and waxes
Clays and minerals	Coal, lignite and wood
Liquid crystals	Explosives, propellants and pyrotechnics
Pharmaceuticals	Biological materials
Metals and alloys	Nature products
Catalysts	

2.7 Summary

POCT as an emerging technology can lead to an eruptive change of lifestyle and medication of population against the traditional medical laboratory. Since living organisms are intrinsically flexible and malleable, flexibility is a necessity for successful integration of electronics in biological systems. Flexible electronics reduce overall sizes, weights, and enable conformal shapes of health care devices that do not cause discomfort during long-term use. The photonic components included in the POCT system can enable the miniaturisation of optical detection, while the flexible circuit expands its applications. Having all components integrated on one flexible substrate, the detection platform can be bent into 3D structure directly and changed for different application easily by adjusting the angle and distance of components.

Vertical interconnections increase the package density enormously, and optical interconnections break the limits of the electrical circuit. Both technologies will become more and more important with the increasing demands on performance in the future.

Electrically conductive adhesive is identified as a promising material to develop a low-temperature processing technique which can protect flexible substrates, plastic fibres and dedicate optoelectronics.

Chapter 3 Geometry effect on electrical performance of ICA vias

3.1 Introduction

In this chapter, a whole set of manufacturing processes was developed to produce the test vehicles. Stencil printing was used for ICA via formation because it was a rapid and flexible deposition method in lab and can be adopted into industrial manufacture. Finite element analysis and theoretical calculation were used to describe the relationship between resistance and via geometry. ICA filled vias were made into flexible PCBs (FPCBs) to research a geometry effect on the resistance of vias. Temperature cycling test, damp heat test and bending test were conducted to investigate the robustness and reliability of the vertical interconnections.

3.2 Experimental and modelling details

3.2.1 Numerical modelling of ICA vias

It can be concluded from previous researches [21–23] that silver particles form a complicated network in the ICA filled via. Thus the model simplification is needed in order to calculate of the via resistance by finite element analysis (FEA). All the silver particles were assumed spheres, and only the bulk resistance was considered:

$$\pi R^2 \times H \times \omega \times \rho_{ICA} = \frac{4}{3}\pi r^3 \times \rho_{Ag} \times N \qquad 3.1$$

Where R is the radius of the via hole, H is the height of the via hole, r is the radius of the silver sphere, ρ_{ICA} is the density of ICA, ρ_{Ag} is the density of the silver, ω is the silver weight percentage. When set $r = 2.5\mu m = 0.0025mm$, the number of sphere can be calculated from equation 3.1, $N = 479$.

As shown in Fig.3.1, 500 spheres were distributed randomly within a cylindrical space (diameter: 0.05mm, height: 0.09mm) by Matlab (The MathWorks, Inc.) programming (Appendices 1), and their coordinates were recorded in the database. Then APDL command stream (Appendices 2) was used to input the coordinates of the spheres into the FEA software

ANSYS (ANSYS, Inc.) and generate the model (Fig.3. 2). Considering the deformation of contacted particles, the centre distance between each two spheres is set to be larger than the 90% of sphere diameter

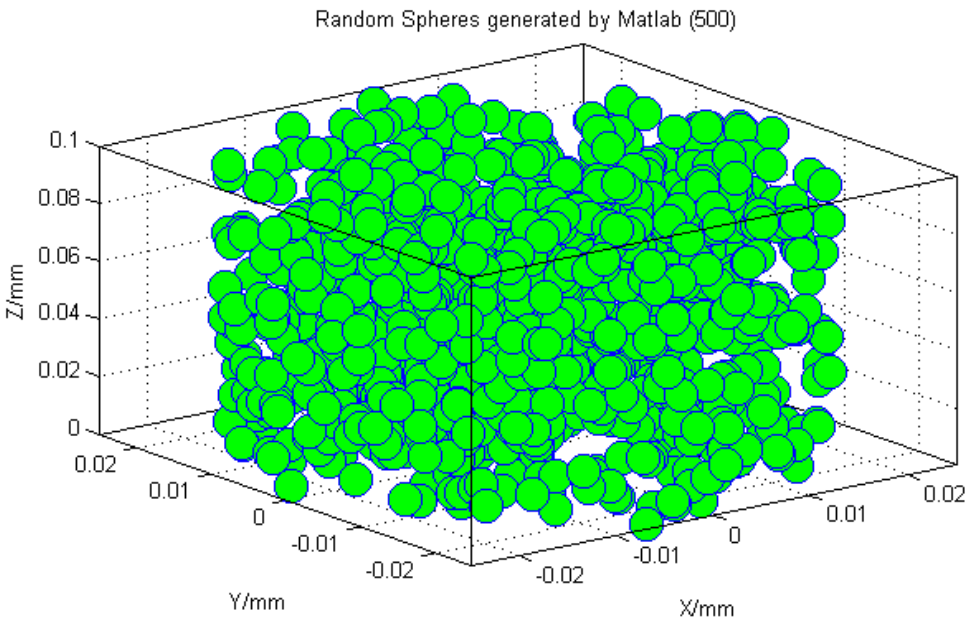

Fig.3. 1 Illustration of random spheres

Table.3. 1 Parameters in the model

Parts	quantity	Dimensions（mm）			
		Length（L）	Width（W）	Height（H）	Diameter（D）
copper	2	1.05	0.40	0.018	—
substrate	1	2.00	1.00	0.054	—
Via hole	1	—	—	0.09	0.05
particle	500	—	—	—	0.0025

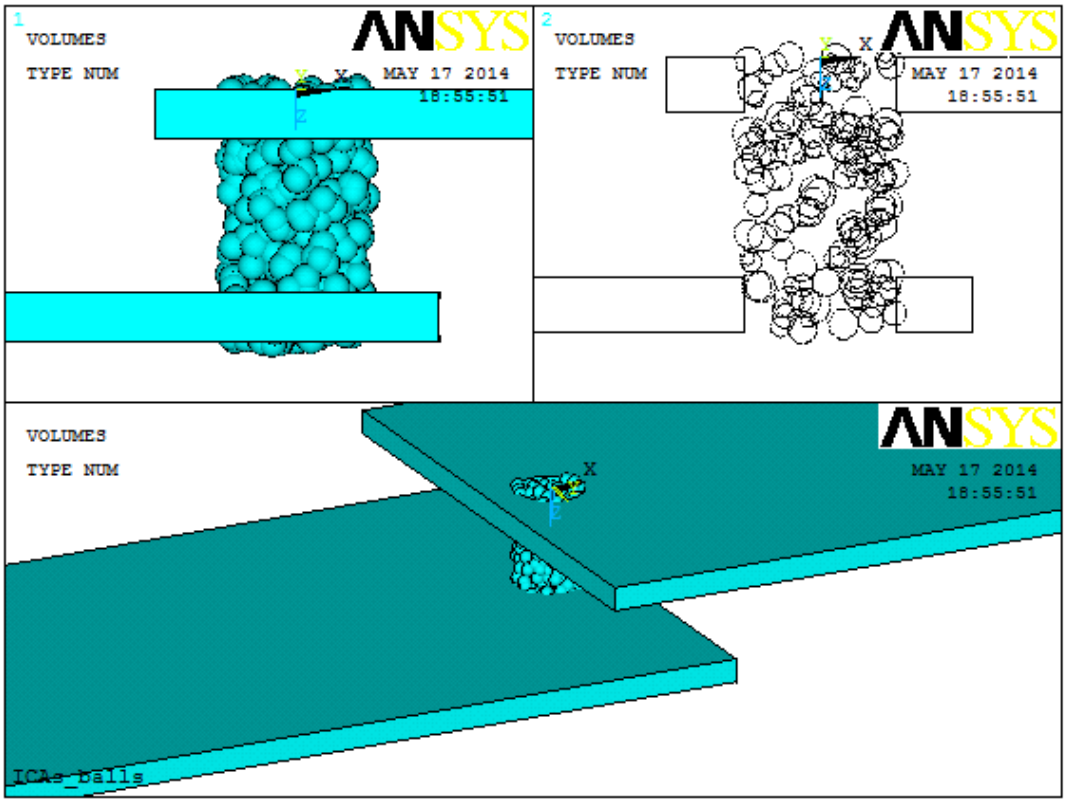

Fig.3. 2 ANSYS model of random spheres via fill

There were some problems in parts union, which stopped the simulation. Thus two models (Fig.3.25) contained fewer particles chains were built to illustrate the basic concept. The top copper track was added a 0.5V load and the bottom track is grounded.

Simplified models were built by assuming ICA as a homogeneous material. As shown in Fig.3.3, only conductive parts, copper track and ICA fill, were taken into modelling. Moreover, a 1μm thick layer of high resistivity material was added between the ICA fill and copper track to represent the interface resistance.

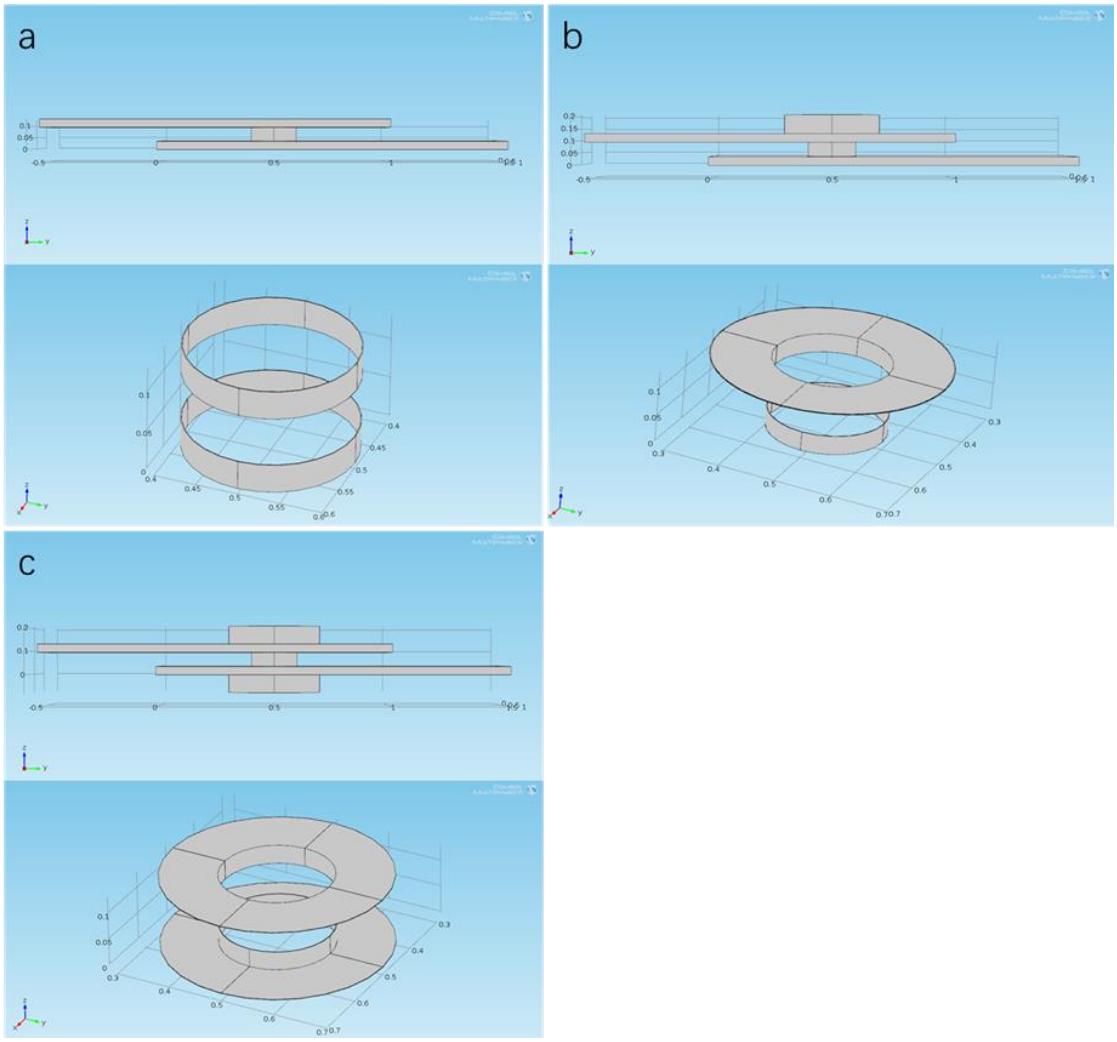

Fig.3. 3 Simplified models of FPCB vertical interconnection and close-up views of the interface layer, a) no-cap model, b) single-cap model, c) double-caps model.

Table.3. 2 Dimensions of the simplified model

Parts	Dimensions（mm）			
	Length（L）	Width（W）	Height (H)	Diameter(D)
Copper track	1.500	1.000	0.035	—
Via hole	—	—	0.130	0.200
ICA cap	—	—	0.080	0.400/0.600/ 0.800

The geometry information of the model is listed in Table.3.2. Finite element analysis (FEA) in this chapter focuses on electrical properties of via fill. To simplify FE modelling and calculation, the simulations were conducted in the AC/DC Physics Module of COMSOL Multiphysics (COMSOL Inc.). Table.3.3 lists necessary material properties for FEA.

Table.3. 3 Electrical properties of materials

Materials	Conductivity（S/m）	Relative permittivity
Copper	5.998e7	1
ICA	1.449e5	1
Interface layer	1.450e3	1

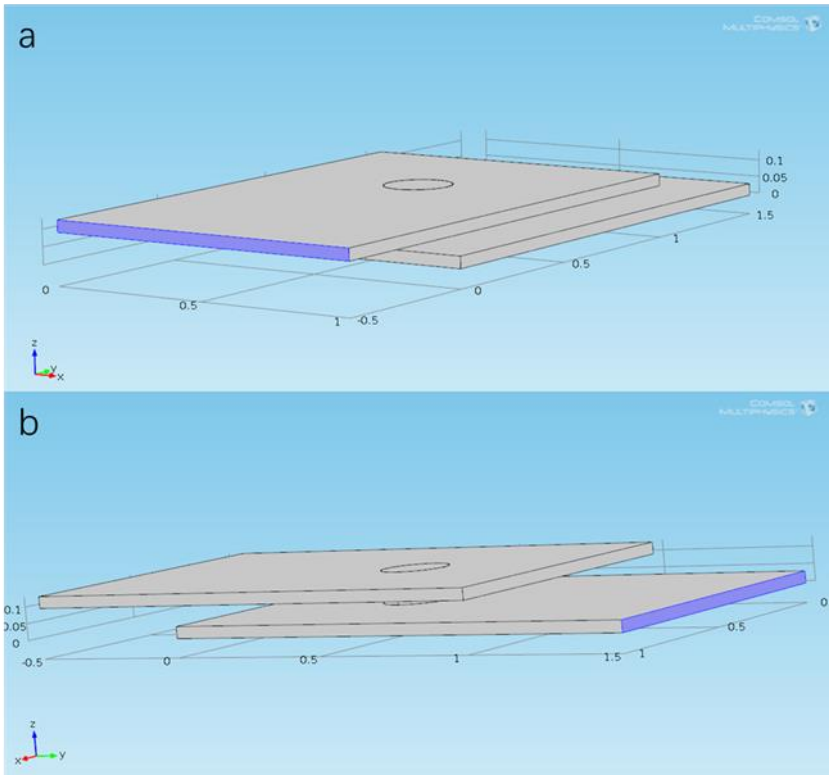

Fig.3. 4 a) The terminal end of copper track, b) the ground end of copper track

In a real condition, the current flow into one end of a copper track and flow out from one end of the other track. Hence, a 0.5A current was applied at the terminal end of the copper track (Fig.3.4 a). The free tetrahedral element was used to mesh irregular shapes precisely. In this research, the via fill was the main part of the investigation, and current crowding happens at

contacting part between copper and via fill. Therefore, ICA fill and interface should be meshed much finer than others (Fig.3.5,3.6).

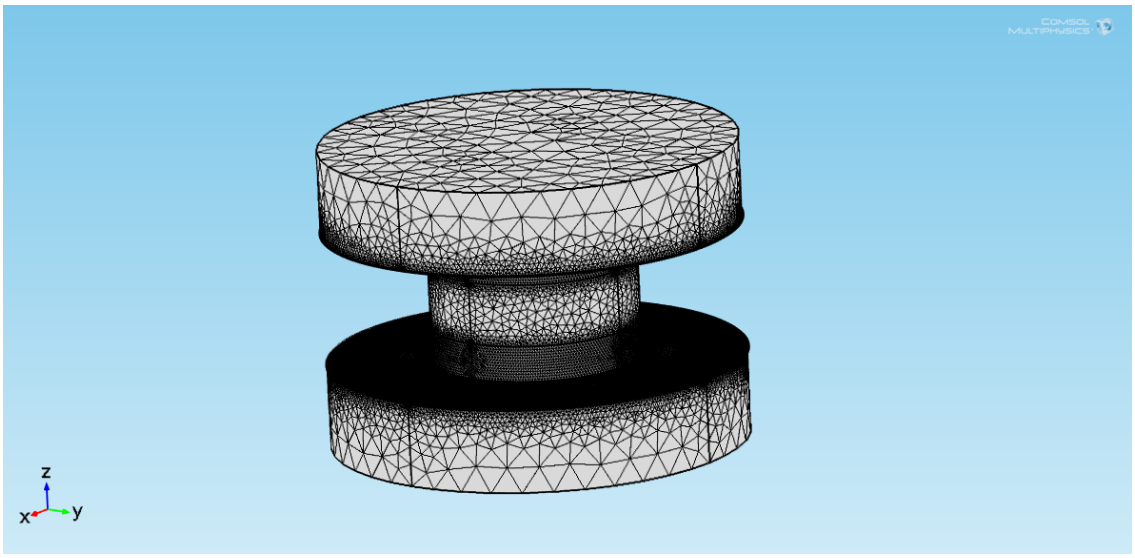

Fig.3. 5 The mesh of via fill

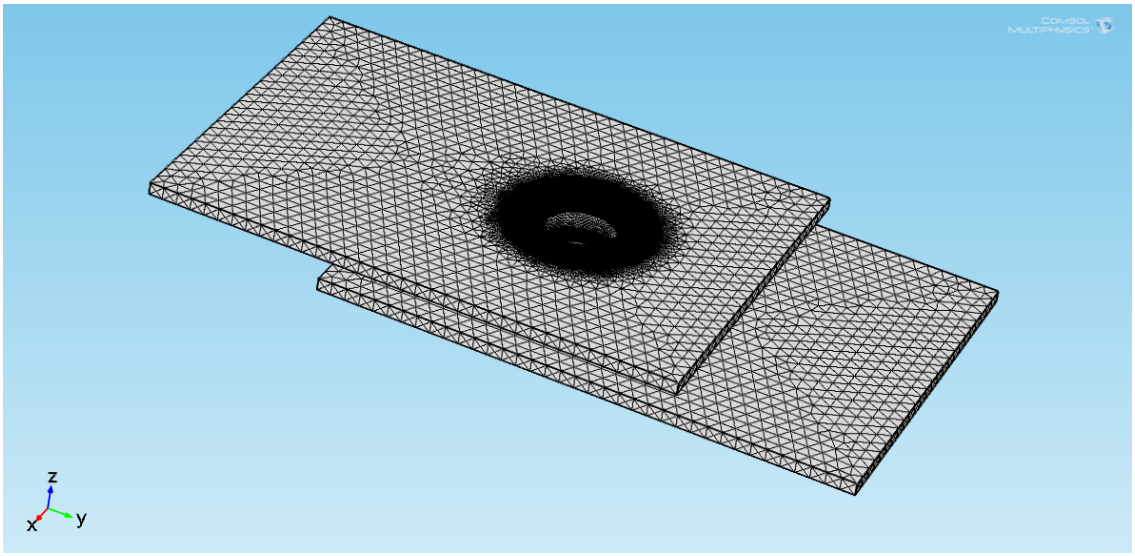

Fig.3. 6 The mesh of copper track

3.2.2 Testing vehicle

The PCB of test vehicle for vertical electrical connection was manufactured by the subtractive method (Fig.3. 7). 130 μm thick double-sided copper clad PI laminate was used as the FPCB substrate; its copper thickness is 35 μm.

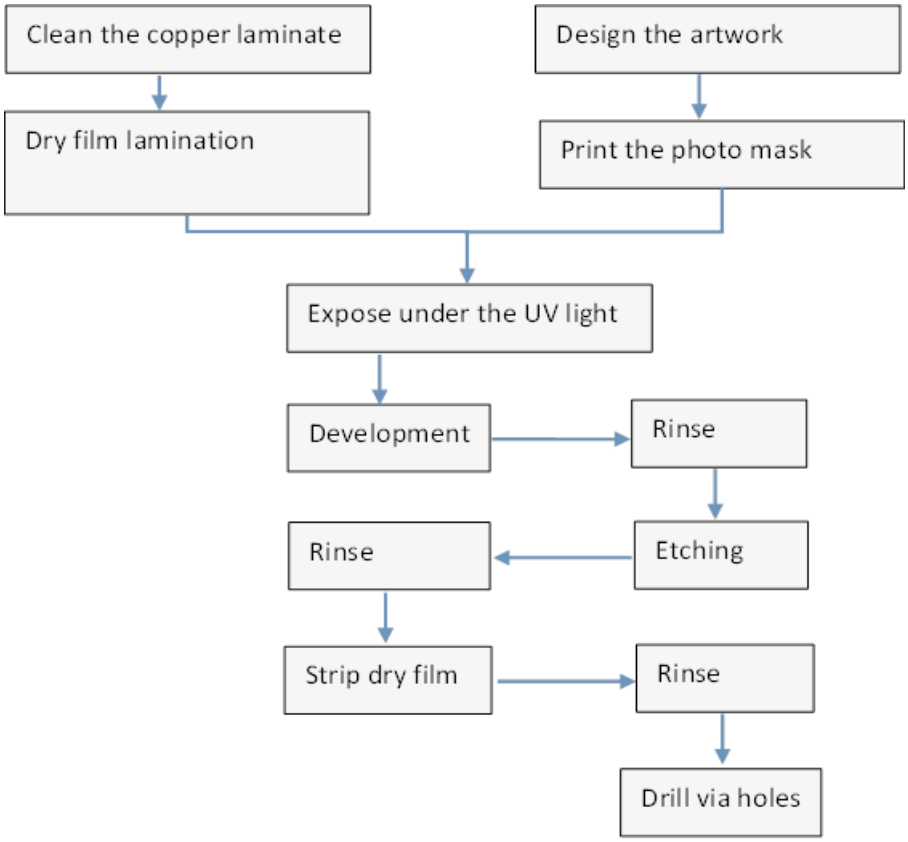

Fig.3. 7 Subtractive PCB manufacture processes

The unexposed part of a dry film is dissolved in developer because the photosensitive layer in the dry film is negative. Therefore, the photomask was printed as a negative plot of the artwork (Fig.3. 8). The exposure, development, etching, dry film stripping and rinse processes were carried within a multifunctional PCB manufacture machine (Fig.3. 9), model: STR-FII (STR Electronics Tech. Co., Ltd. China)

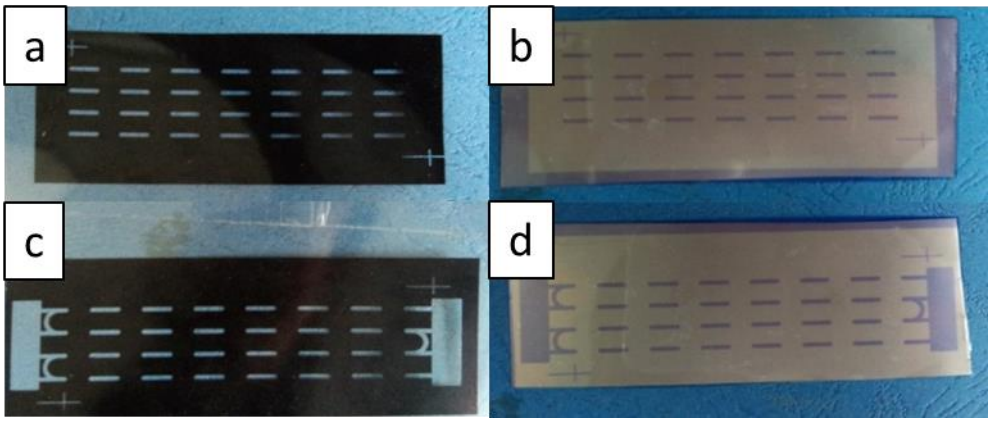

Fig.3. 8 a) Bottom photomask, b) copper laminate with dry film after exposure (bottom), c) top photomask, d) copper laminate with dry film after exposure (top)

Fig.3. 9 PCB manufacture machines

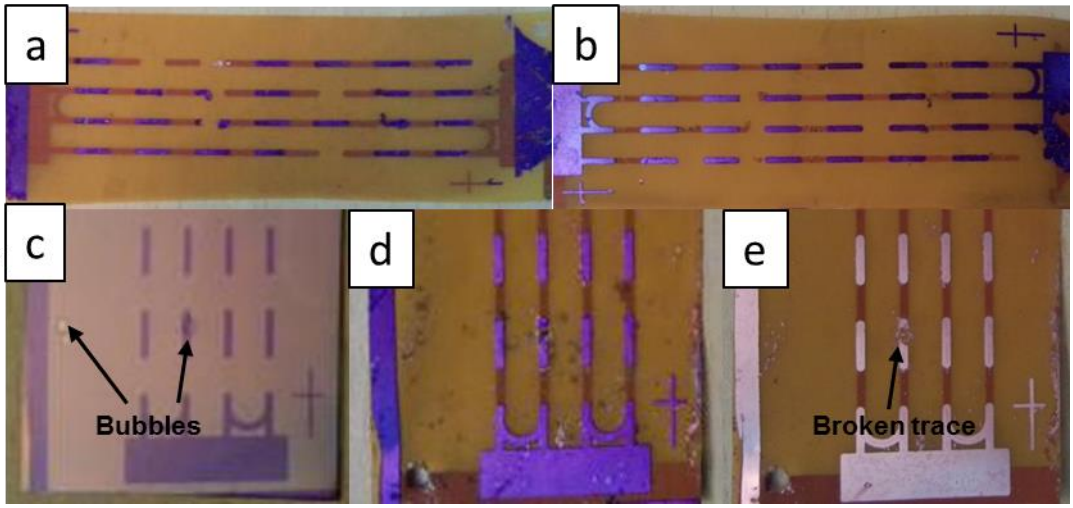

Fig.3. 10 Desired patterns were etched away (a: bottom side, b: top side), the trapped air bubble broke the trace pattern (c: after lamination, d: after development, e: after etching)

Dry film lamination was crucial to the FPCB manufacture. The exposed dry film would be washed away during the development or etching due to the poor adhesion (Fig.3. 10.a and b). Wrinkles and trapped air bubbles could break the patterns (Fig.3. 10.c, d and e). Changing the exposure time or the development temperature could not fix the above problems. To improve the adhesion, after attaching the dry films to the copper laminates, they were put on a heating stage, swept by a rubber blade at 50 ^{o}C. The FPCB was redesigned smaller to gain a better control of the wrinkles and bubbles during manual dry film lamination. The number of vias was

reduced to 20, and the pattern area was only one-third of the first design (Fig.3.11.a). Later the number of vias was reduced further to improve stencil printing and gain the area for test lead (Fig.3.11.b). The optimised exposure time is 100 seconds, and the temperature of developer solution was at 35 ^{o}C.

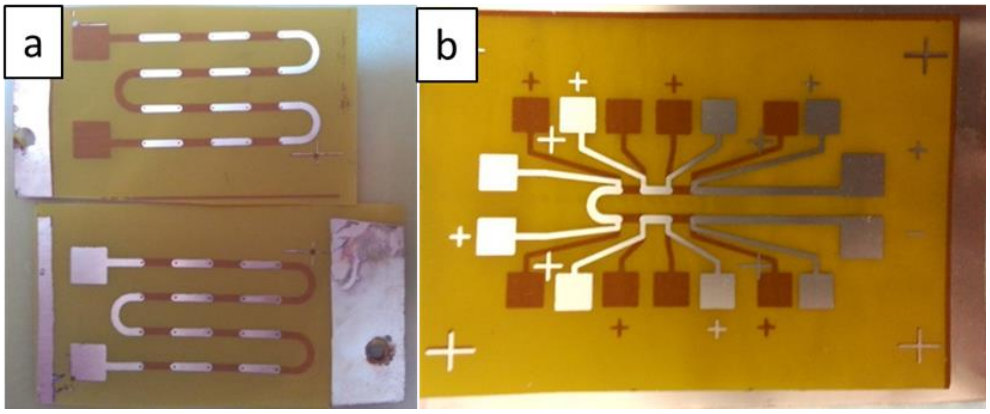

Fig.3. 11 a) 20 vias FPCB, B) 8 vias FPCB

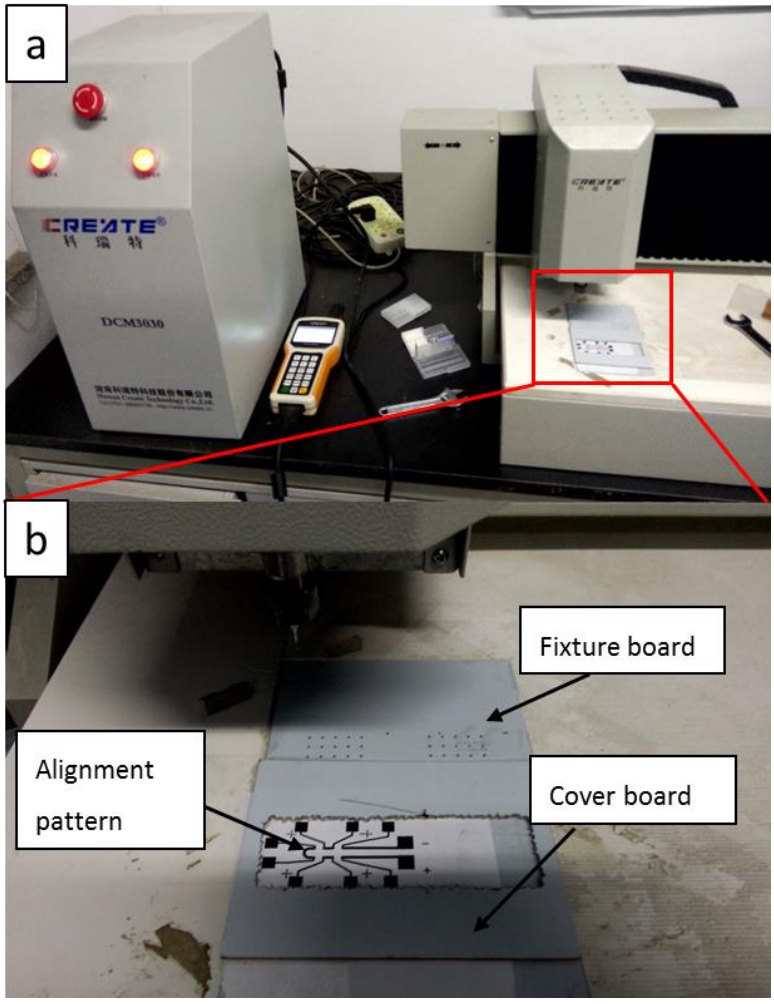

Fig.3. 12 a) Numerical control drilling machine, b) a close look at fixture board

Alignments holes (Φ0.9 mm) and via holes (Φ0.2 mm) were drill by a numerical control drilling machine (Fig.3.12.a), DCM 3030 (Hunan Create Technology Co., Ltd.). The FPCBs were put on the fixture board and matched the alignment pattern, and then the rectangle ring board covered and fixed the FPCB. (Fig.3.12.b)

3.2.3 Adhesive deposition by stencil printing

Right before the vias filling, an ICA strip (0.2 mm wide, 0.2 mm thick) was printed on the resistivity test board for resistivity calibration (Fig.3.13). The test strip was cured at 100 ^{o}C for 10 minutes.

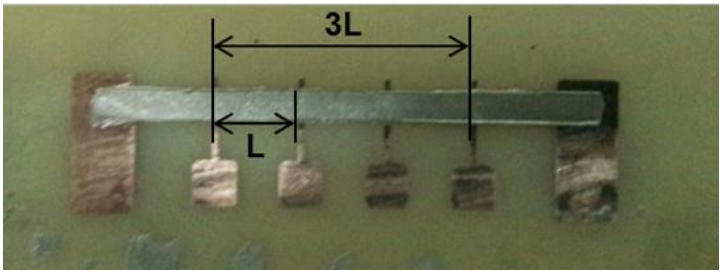

Fig.3. 13 ICA strip printed on the resistivity test board, L=5mm

There were three stencil printing arrangements: the first one was to form a cap around the via by printing from one side (Fig.3.14. A), the second one was to form caps on each side by print from both sides (Fig.3.14. B), the last one was to ensure ICA only contacts the side wall of the copper track by post-scrape.

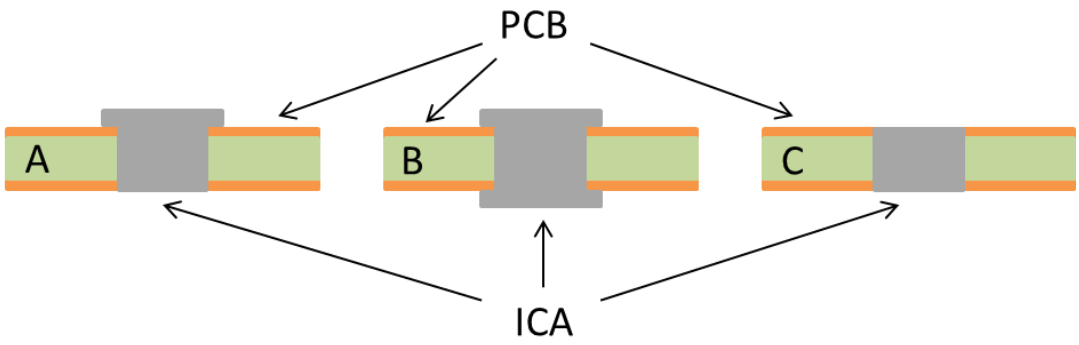

Fig.3. 14 Via structures formed by different stencil printing arrangement, A) single cap B) double caps C) no cap

PET stencil, drilled by numerical control drilling machine, was first tried. The stencil and FPCB were aligned and fixed on the mounting plate by two alignment pins (Fig.3.15). Then a metal blade covered by plastic tape was used to print the ICA.

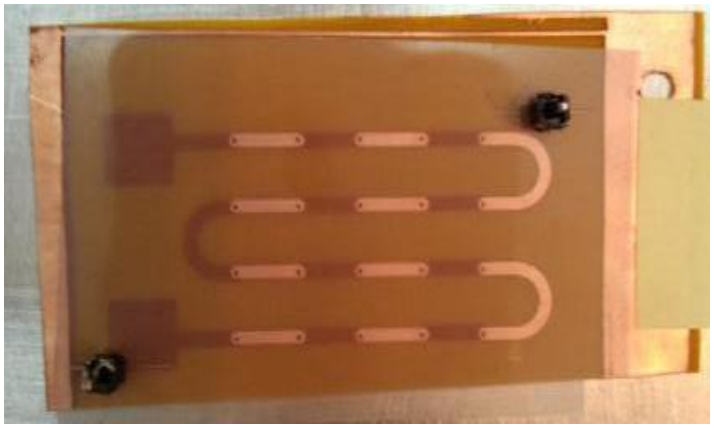

Fig.3. 15 The PET stencil and FPCB fixed on the mounting plate

The test vehicles manufactured by the PET stencil printing were not completely electrical connected. Several series of the vias were picked out and measured by a multimeter. The average resistances are listed in Table.3.4.

Table.3. 4 The average resistances of vias

Stencil printing arrangement	Stencil thickness	Stencil aperture Φ0.4 mm	Stencil aperture Φ0.6 mm
Double side printing	0.1 mm	84 mΩ	58 mΩ
	0.2 mm	213 mΩ	70 mΩ
Single side printing	0.1 mm	104 mΩ	104 mΩ
	0.2 mm	250 mΩ	163 mΩ

It could be concluded that the resistances of vias with the ICA caps on both sides are lower than the resistances of vias with only one cap. The resistances of the vias formed by Φ0.6 mm stencil aperture were lower than the vias formed by Φ0.4 mm stencil aperture.

The printing quality also affected the resistance of the vias. The PET stencil was easily warped during the printing, which caused the misalignment. Misalignment between the stencil and FPCB would lead to partially filled vias which owned much larger resistance (Fig.3.16). The

burrs at the stencil opening, generated during the mechanical drilling, reduced the ICA deposition. These abnormal points had been ruled out when calculating the average resistance. Most ICA was left in the 0.2 mm thick stencil apertures during printing because of the high aspect ratio and rough aperture wall. Therefore, the resistances of the vias filled by 0.2 mm thick stencil were larger and varied.

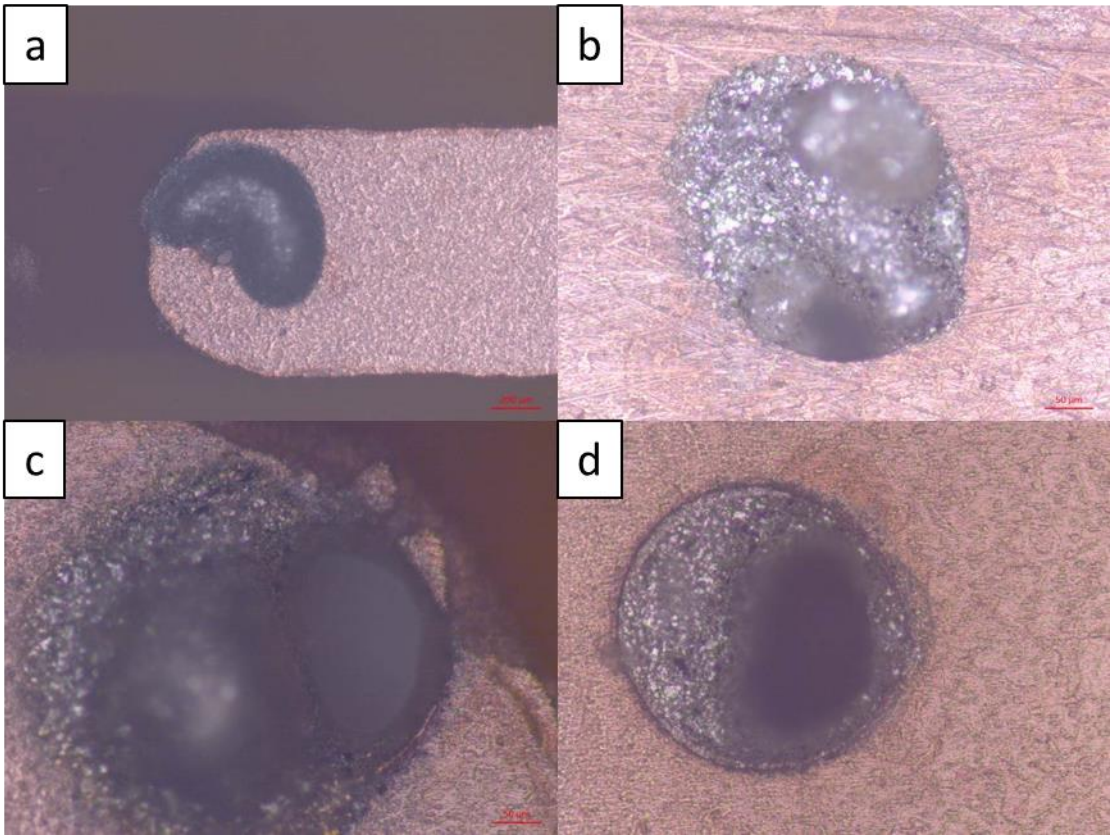

Fig.3. 16 Optical image of partially filled vias: a) top side of a via printed by 0.1 mm thick stencil, (50X), b) bottom side of a via printed by 0.1 mm thick stencil (200X), c) top side of a via printed by 0.2 mm thick stencil (200X), d) bottom side of a via printed by 0.2 mm thick stencil (200X)

In order to improve the printing quality, laser drilled stainless steel stencils were adopted (Fig.3.17). There were four alignment pins on the mounting plate to ensure the alignment between the FPCB and stencil.

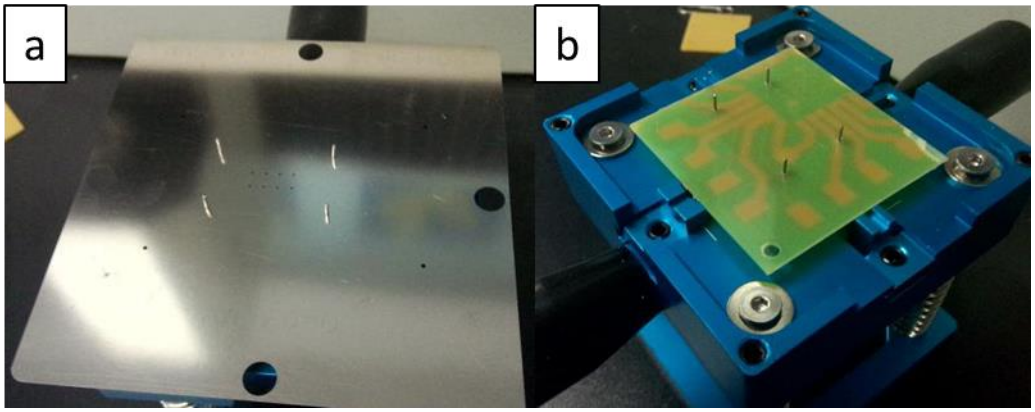

Fig.3. 17 a) Stainless steel stencil, b) mounting stage

Reduction in the number of vias in each test vehicle increased the yield of complete deposition in stencil printing. Together with the mounting plate, the stainless steel stencil with Φ0.2 mm aperture was successfully used in vias filling (Fig.3.18). Four stainless steel stencils with different thickness (T) and aperture diameters (Φ) were used to make the trial test vehicles. All test vehicles were electrical connected; their overall resistances are listed in Table.3.5.

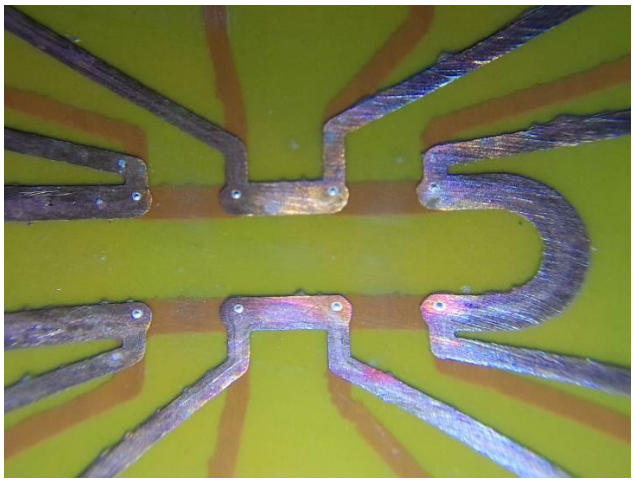

Fig.3. 18 Vias filled by 0.1 mm thick stainless steel stencil with Φ0.2 mm aperture

Table.3. 5 The overall resistances of test vehicles made by stainless steel stencils

Stencil size / Printing arrangement	Stencil aperture Φ=0.2 mm		Stencil aperture Φ=0.6 mm	
	Thickness T=0.1 mm	Thickness T=0.12 mm	Thickness T=0.1 mm	Thickness T=0.12 mm
Double caps	1.754 Ω	2.460 Ω	1.402 Ω	2.404 Ω

It can be seen from Table.3.5, the 0.1 mm thick stencil provided a better ICA deposition under our available techniques. According to the above trials and analysis, a batch of test vehicles was made for following tests using the 0.1 mm thick stainless steel stencil with different apertures (Φ0.4 mm, Φ 0.6 mm and Φ 0.8 mm).

3.2.4 Testing equipment and techniques

- Electrical test

The resistance of the vias was measured by using Kelvin Four-terminal sensing (KFTS) method (Fig.3.19). The current source is Keithley 2260A 30-36, Its current accuracy is 0.1%+5mA. The voltage sensor is a digital multimeter (TH1952, Tonghui Electronic Co., Ltd.) with the accuracy of 0.5%+1digit.

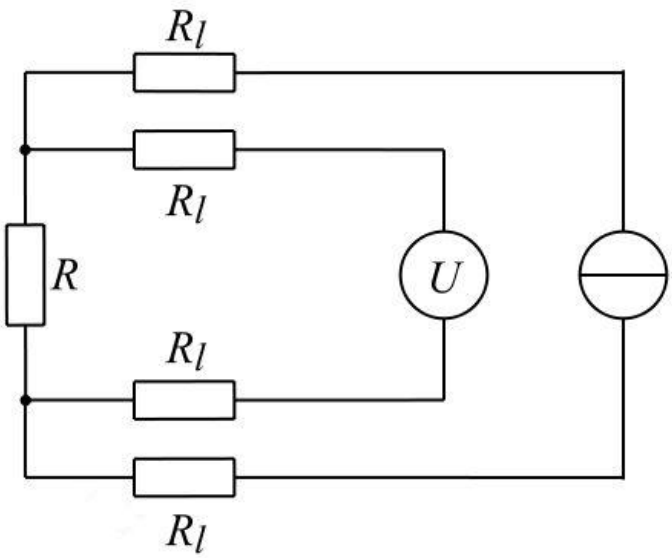

Fig.3. 19 Theoretical illustration of Kelvin Four-terminal sensing

- Thermal cycling

As shown in Fig.3.20, the test vehicles were put in the air-to-air temperature cycle test chamber (NT531A, Kusumoto Chemicals Corporation ETAC Division, Japan) for thermal shock cycling. A connection reliability evaluation system (MLR22, Kusumoto Chemicals Corporation ETAC Division, Japan) was connected to the test vehicles to monitor the resistances. The thermal shock operation was programmed to do the cyclic shift between -40 °C and 125 °C, upper and lower soak times are 30 minutes, corresponding to BS ISO 16525-7.

- Damp heat, steady state testing

The test vehicles were kept in the environment of 85 °C and 85% relative humidity (Fig.3.21), in accordance with BS ISO 16525-7. Via resistances were monitored twice a day.

- Bending test

Bending experiments were performed by flexing the samples around cylinders having radii of 100 and 5 mm, respectively. Test vehicles were bent to the cylinders and recovered, count as one bending cycle. There were five bending strategies: one cycle and standing for resistance stabilisation, five cycles in a row, ten cycles in a row, forty cycles in a row and fifty cycles in a row. The resistance of the circuit was monitored simultaneously.

Fig.3. 20 Temperature cycle test system

Fig.3. 21 85 °C/85RH test chamber and the digital multimeter with a computer for real-time recording

3.3 Results and discussions

3.3.1 Electrical simulations of ICA vias

As shown in the Fig.3.22, Significant voltage drop appear on the top copper track when the conduction channels increase to three. It's because the resistance of the ICA part decreased and the voltage ratio of the whole circuit become smaller. The current density increased at the particles connected to several branch conduction channels or the particles connected the main connection channel and the copper track. Although the conductive network is randomly connected, electrons always tend to pass through the path of the lowest resistance. Generally, the resistance of shorter particles chain is lower because of less particle and inter-particle resistances. Therefore, current in ICA vias would exhibit similar characteristics like in homogeneous conductive material.

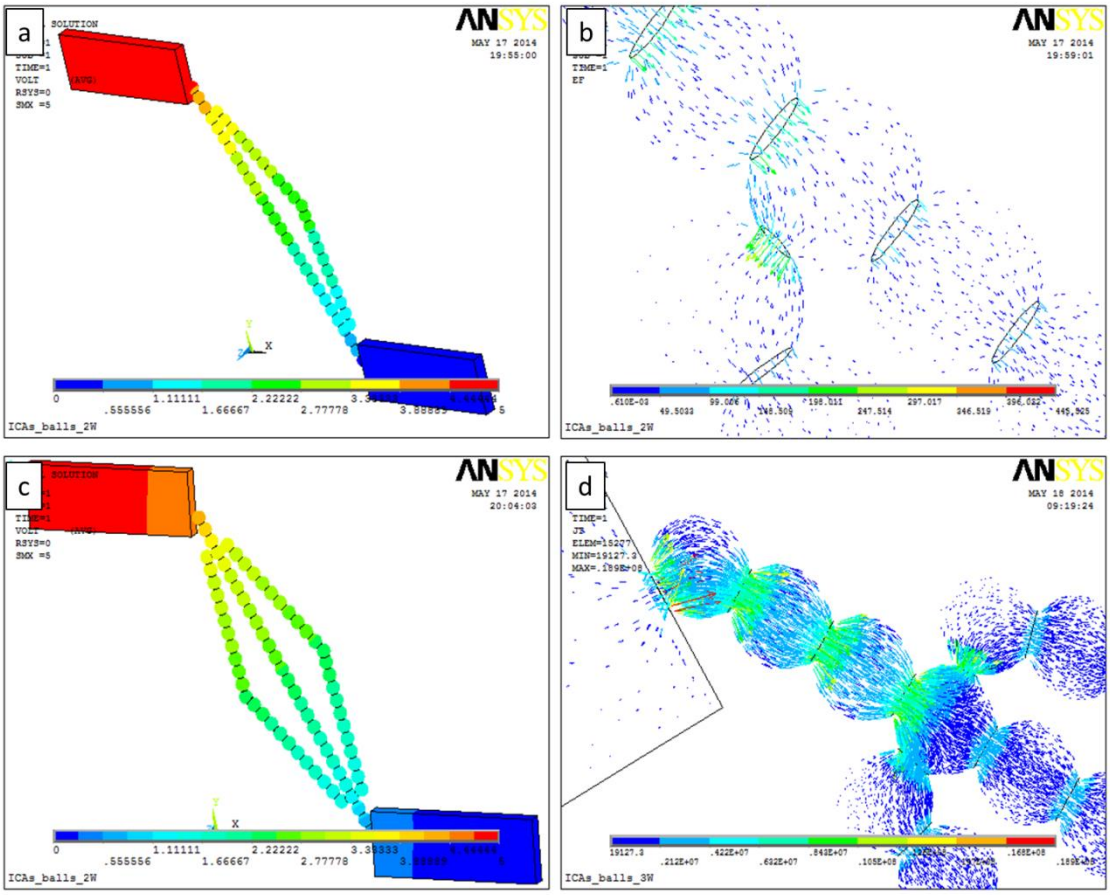

Fig.3. 22 a) Electrical potential of two channels model, b) Electrical current density of two channels model in vectors, c) Electrical potential of three channels model, d) Electrical current density of three channels model in vectors

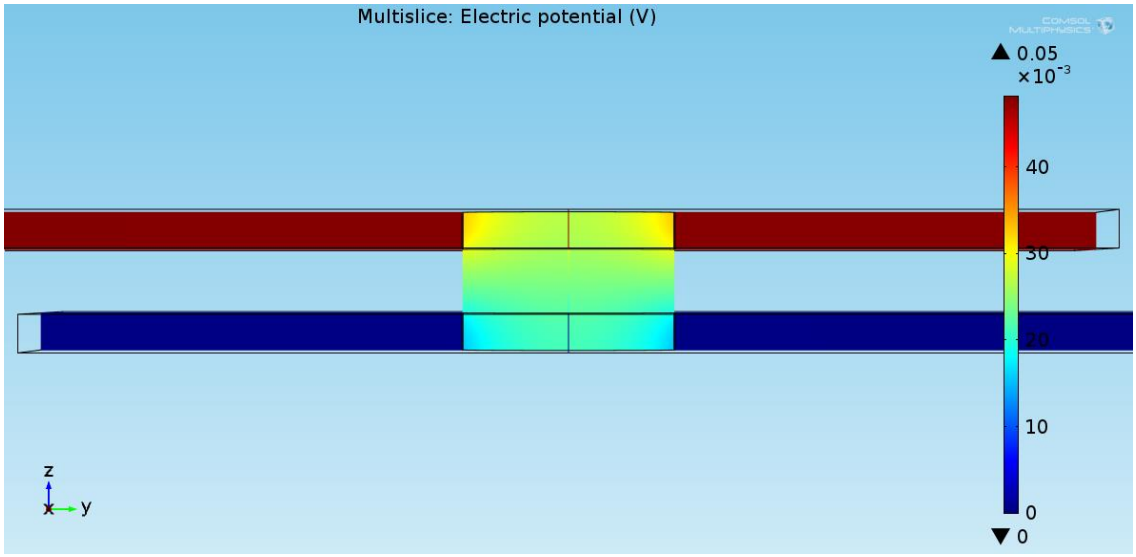

Fig.3. 23 Electrical potential diagram of the whole model (no cap)

Fig.3.23 shows the electrical potential in homogeneous via fill. There was a voltage drop from the edge to centre in a horizontal plane, and the voltage gradient in vertical direction increased

from the centre to edge. The resistivity of the ICA was much higher than the copper trace, resulting in an effective iso-potential Cu land. Combining current density analysis (Fig.3.24), it could be concluded that the current density increases rapidly around the ICA-copper contact area and most current flow through the outer tubular part of the ICA fill.

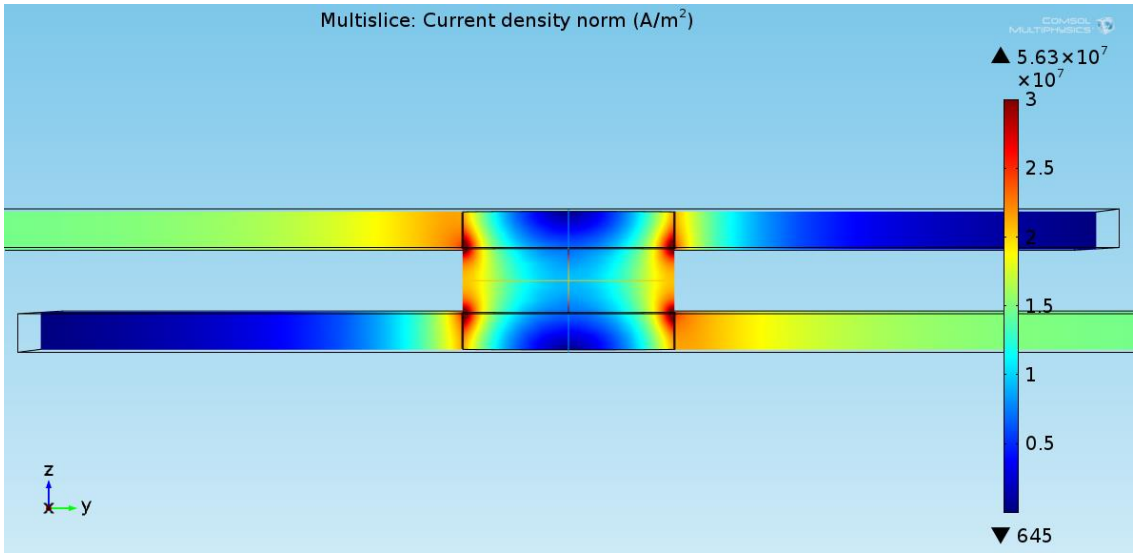

Fig.3. 24 Electrical current density of the whole model (no cap)

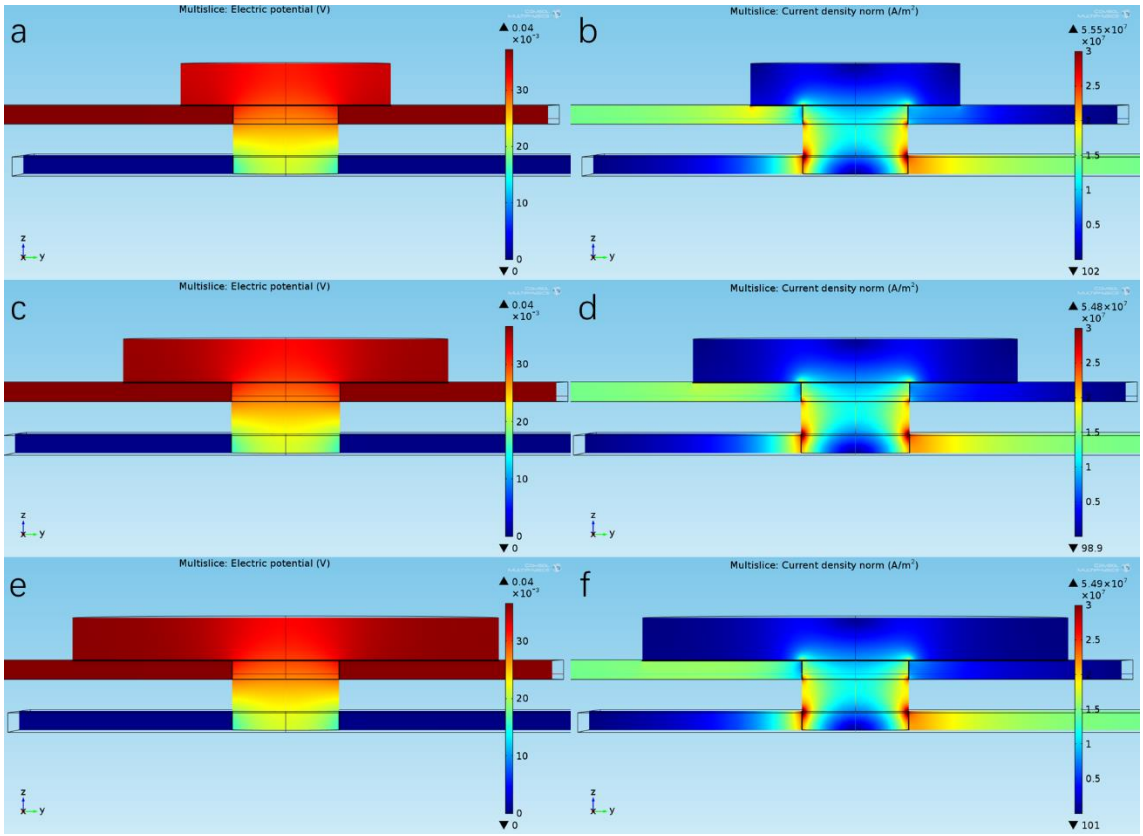

Fig.3. 25 Electrical current density distributions in via fill

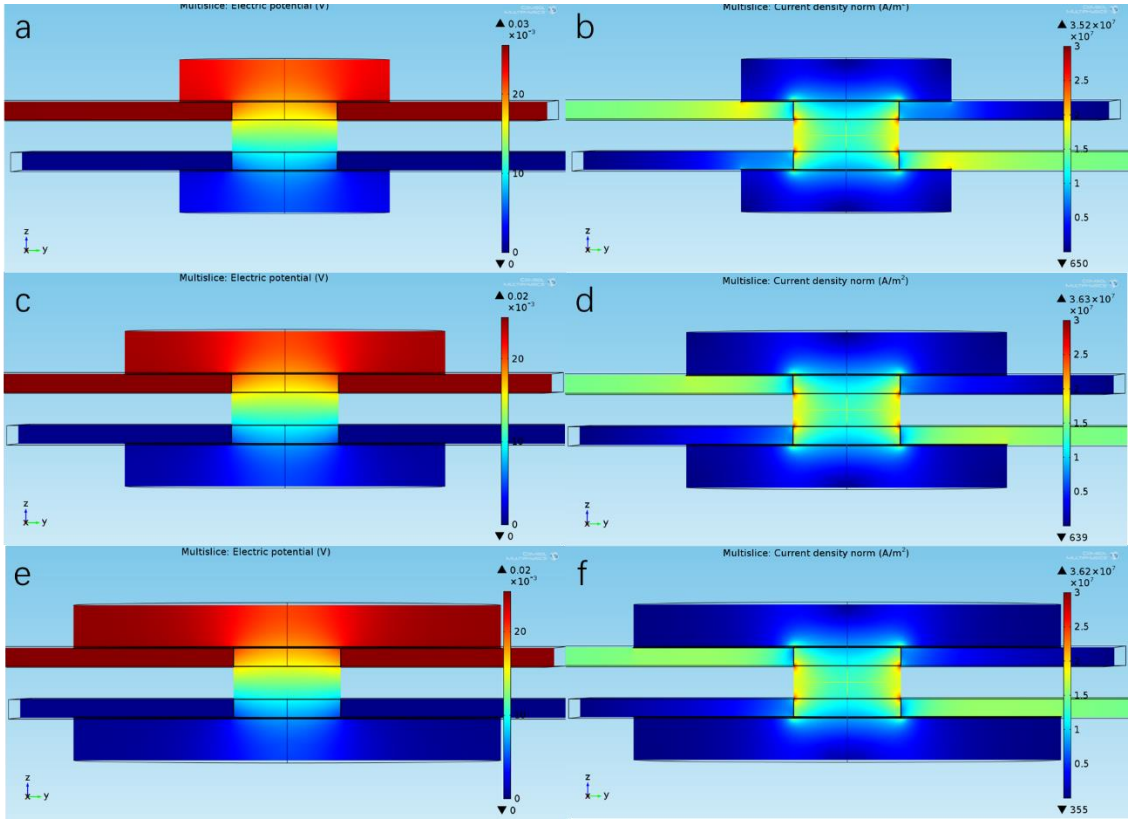

Fig.3. 26 a) Electrical current density of the whole via fill, b) x-z cross-section of the via fill

The resistance of model was calculated by the software built-in equation and the via resistance versus cap diameter was plotted in Fig.3.27. Simulation results reveal that cap structure can ease the current crowding and reduce the total resistance. Such geometry effect was significant from no cap to ø0.4mm and faded away from ø0.4mm to ø0.8mm

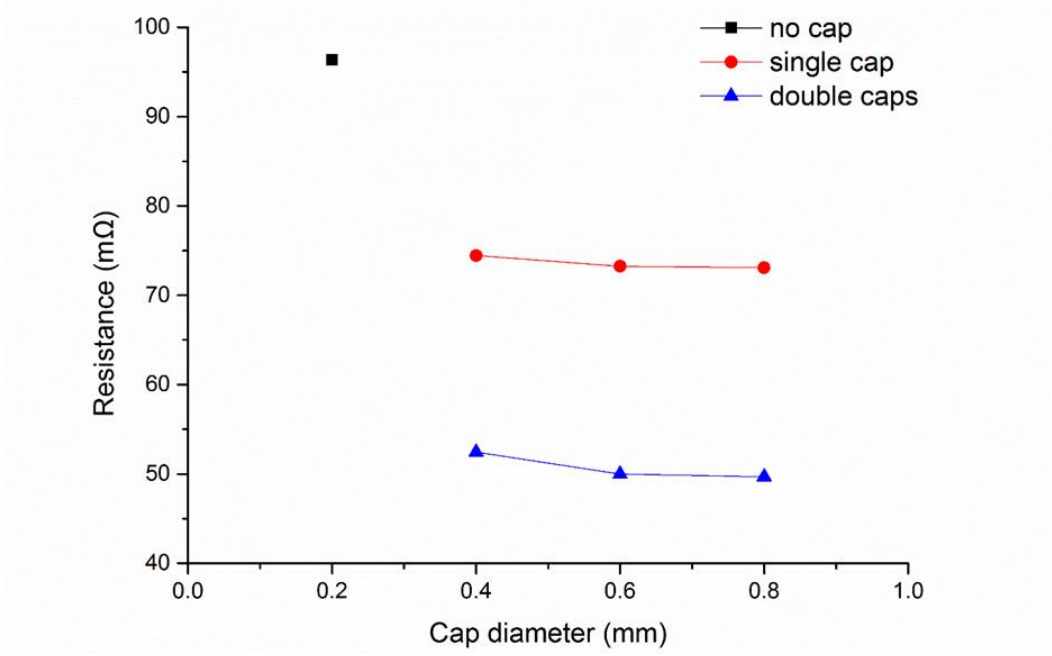

Fig.3. 27 Computational resistance versus cap diameter

3.3.2 Theoretical calculation of ICA vias resistance

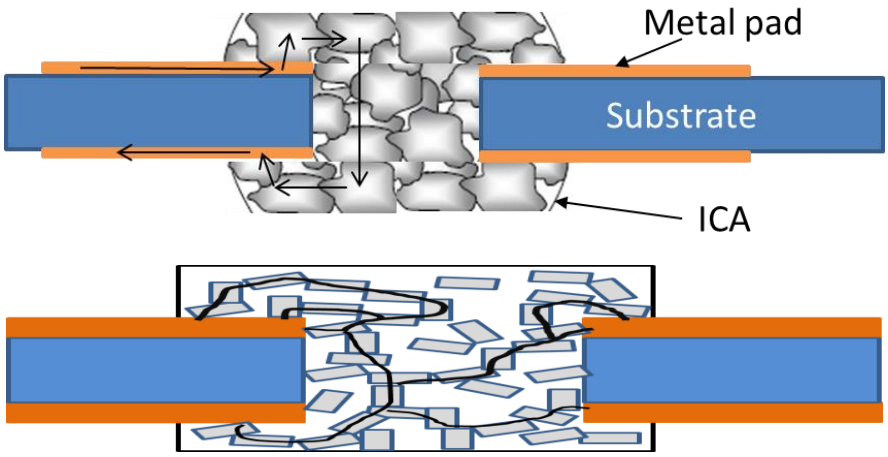

Fig.3. 28 Schematic illustration of ICA vertical interconnection in FPCB

As shown in Fig.3.28, the current transfer from the top circuit to the bottom circuit through an ICA filled via. The total resistance of the via is

$$R = R_{fill} + R_{top} + R_{bottom} \qquad 3.2$$

R_{fill} is the resistance of ICA fill, R_{top} and R_{bottom} are the interface resistances between metal pads and ICA fill. R_{fill} is decided by the resistivity of the ICA and the geometry of ICA fill. The

interface resistances is affected by several factors, such as contact area, properties of contact surface and process conditions [21, 106, 119, 120].

The rivet-shaped via (Fig.3.29.a) was transformed into regular resistors in series (Fig.3.29.b).

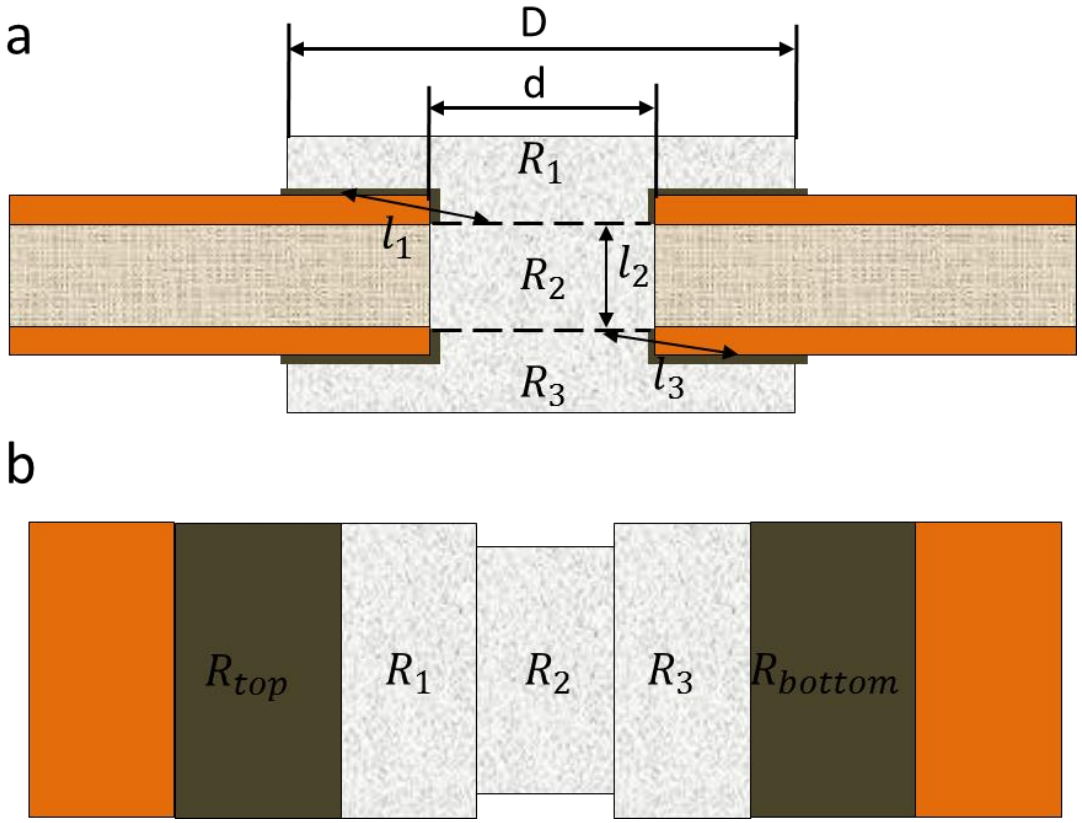

Fig.3. 29 Schematic illustration of via's equivalent model

In order to focus on how the via geometry affects via resistance, the interface resistance was set as a constant value (no cap: 50 mΩ, single cap: 37 mΩ, double caps: 24 mΩ) according to simulation results. Therefore the total resistance of the via is

$$R = R_{fill} + R_{interface} \tag{3.3}$$

The resistance of ICA fill could be calculated by Eq.3.4:

$$R_{fill} = R_1 + R_2 + R_3 = \rho \times \frac{l_1}{A_1} + \rho \times \frac{l_2}{A_2} + \rho \times \frac{l_3}{A_3} \tag{3.4}$$

Where ρ is the resistivity of ICA, A is cross-sectional area of the resistor, l is the length of the resistor. The cross-section area of R_1 and R_3 is defined as the contact area between ICA and

copper track. The length of these resistors is defined as the centre distance between two ends. The resistor R_2 is a cylinder in the middle of the via hole, thus:

$$A_1 = A_3 = \frac{\pi D^2}{4} - \frac{\pi d^2}{4} + \pi dt \tag{3.5}$$

$$l_1 = l_3 = \sqrt{\left(\frac{D/_2 - d/_2}{2} + \frac{d}{4}\right)^2 + \left(\frac{t}{2}\right)^2} = \sqrt{\left(\frac{D}{4}\right)^2 + \left(\frac{t}{2}\right)^2} \tag{3.6}$$

$$A_2 = \frac{\pi d^2}{4} \tag{3.7}$$

$$l_2 = \mathrm{H} - 2\mathrm{t} \tag{3.8}$$

Where D is the outer diameter of the ICA cap, d is the diameter of the via hole, t is thickness of the copper track, and H is the thickness of the FPCB. By combining Eq.3.4, Eq.3.5, Eq.3.6, Eq.3.7 and Eq.3.8, Eq.3.3 can be presented as:

$$R = \rho \times \left(\frac{\sqrt{\left(\frac{D}{4}\right)^2 + \left(\frac{t}{2}\right)^2}}{\frac{\pi D^2}{4} - \frac{\pi d^2}{4} + \pi dt} + \frac{\mathrm{H}-2\mathrm{t}}{\frac{\pi d^2}{4}} + \frac{\sqrt{\left(\frac{D}{4}\right)^2 + \left(\frac{t}{2}\right)^2}}{\frac{\pi D^2}{4} - \frac{\pi d^2}{4} + \pi dt} \right) + R_{interface} \tag{3.9}$$

In this research, all the FPCBs were the same thus the only variable in the model was the cap size of the via. PCB thickness H=0.13mm, copper track thickness t=0.035mm, via hole diameter d=0.2mm, ICA resistivity $\rho = 0.0069\Omega \cdot \mathrm{mm}$. Therefore:

$$A_2 = 0.031mm^2$$

$$l_2 = 0.06\mathrm{mm}$$

Then the resistance of via was calculated using Eq.3.9. (Table. 3.6)

Table.3. 6 The calculated resistance of via with different geometries

Geometry	A_1 (mm²)	A_3 (mm²)	l_1 (mm)	R_{fill} (Ω)	R (Ω)
No cap	0.022	0.022	0.053	0.047	0.097
Φ0.4 mm S*	0.116	0.022	0.102	0.036	0.073
Φ0.6 mm S	0.273	0.022	0.151	0.034	0.071
Φ0.4 mm D*	0.116	0.116	0.102	0.025	0.049
Φ0.6 mm D	0.273	0.273	0.151	0.021	0.045
Φ0.8 mm D	0.493	0.493	0.201	0.019	0.043

*S represents Single cap; D represents Double caps.

3.3.3 Resistances of ICA vias with different geometry

Vias with 0.4mm, 0.6mm and 0.8mm diameter caps and without caps were fabricated for the resistance test.

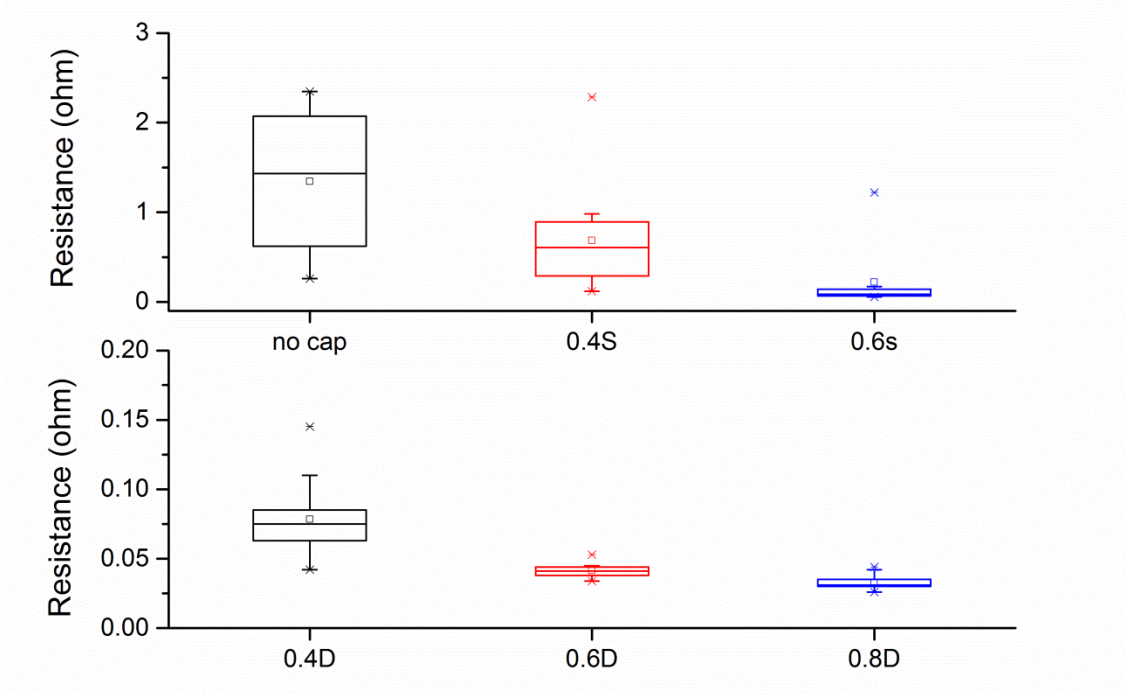

Fig.3. 30 The box charts of experimental vias resistances

Finer vias require better manufacturing process control that the lab can't achieve. Therefore the resistances of no cap and 0.4mm-caps vias are more dispersive (Fig.3.30). Both the calculated and experimental results agree the same pattern: the vias resistances decrease while the cap

diameter increases, and the decline in resistance is significant at the beginning then slows down (Fig.3.31).

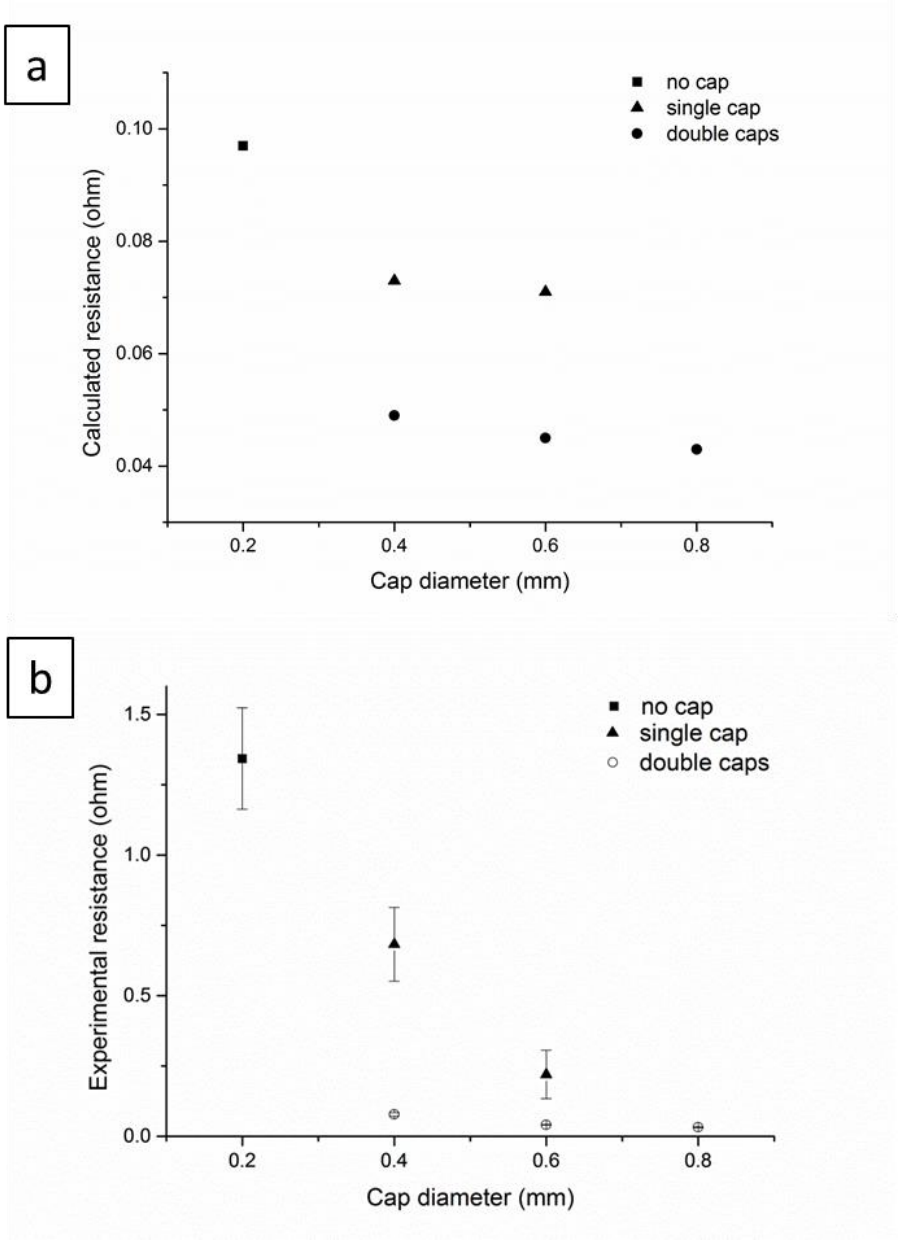

Fig.3. 31 a) Theoretical via resistances verse cap diameter, b) Average via resistances of test vehicles verse cap diameter

The above calculation and experiments prove that the ICA caps can significantly increase the conductivity of the via, especially double caps structure. Larger cap area introduces more parallel current paths, but the resistances in long paths are high. As a result, the increase of cap area increases the conductivity, while the gain is diminishing. These findings could help achieve a balance between PCB design, performance and cost.

3.3.4 Thermal cycling and damp heat ageing

The change of test vehicles resistance for different geometry vias as a result of the temperature cycling test is shown in Figure 3.32.

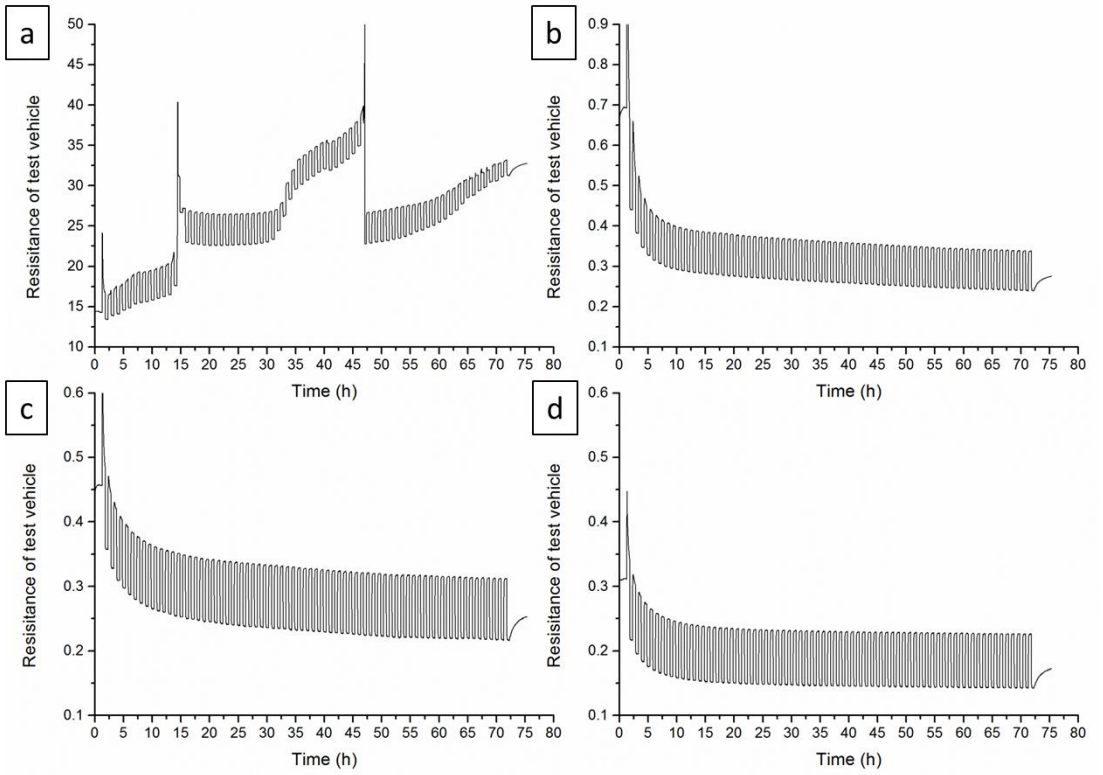

Fig.3. 32 Evolution of via resistance as a function of time exposed to temperatures cycles alternating between -40°C and 125°C. a) no cap, b) Φ0.4 mm double caps, C) Φ0.6 mm single cap, d) Φ0.6 mm double caps

Since the change of copper track resistance is the same in temperature cycles, the changes of test vehicle resistance represent the changes of via resistance. The vias with double caps were steadiest, and the vias with no cap were increased and fluctuated. This can be explained by the CTE mismatch of the FPCB and ICA, the crack and detachment tend to grow along the interface between the copper and ICA, while the caps can stabilise the deterioration. The decrease in resistance can be explained by a beneficial post-curing effect on ICA, induced by the prolonged exposure to high temperature.

As shown in Fig. 3.33, a similar pattern can also be observed in 85°C /85RH damp heat test. Vias with no cap or single cap are more vulnerable to thermal stress.

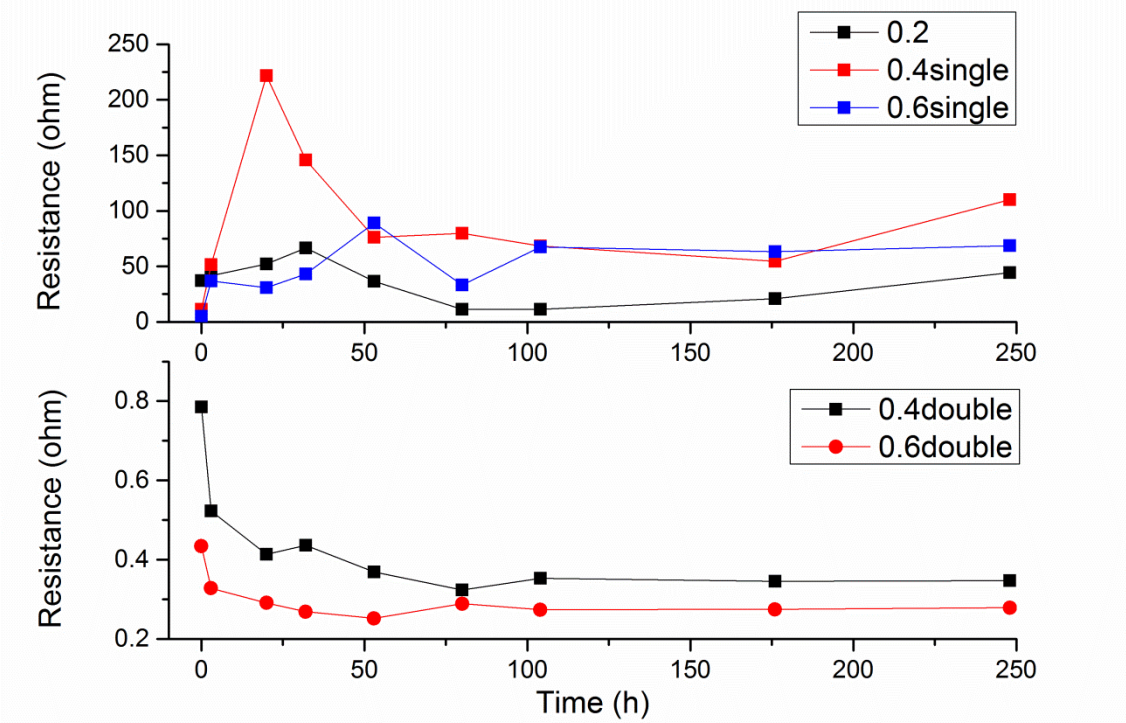

Fig.3. 33 Resistance evolution as a function of time at 85°C/85% RH

3.3.5 Mechanical bending

The resistances of test vehicles changed slightly after bending around Φ100mm cylinder for 3000 times (Fig.3.34). The ICA vias exhibited reasonable lifetime in this test. To accelerate the bending test and observe obvious changes in resistance, the other series of test vehicles were flexed around Φ5mm cylinder in order to induce more mechanical stress. Firstly, a 30 mm long copper track on the FPCB was tested to set a baseline. As shown in Fig.3.35, such small radius bending of FPCB didn't affect the resistance of the copper circuit.

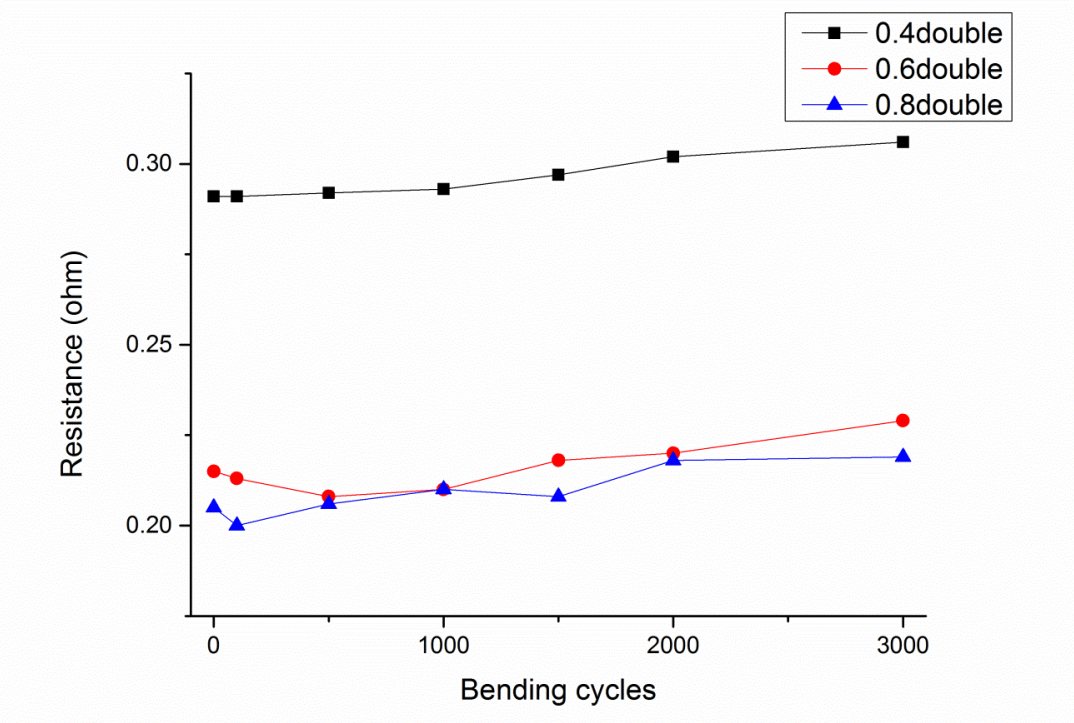

Fig.3. 34 Test vehicles resistance versus bending cycles (Φ100mm cylinder)

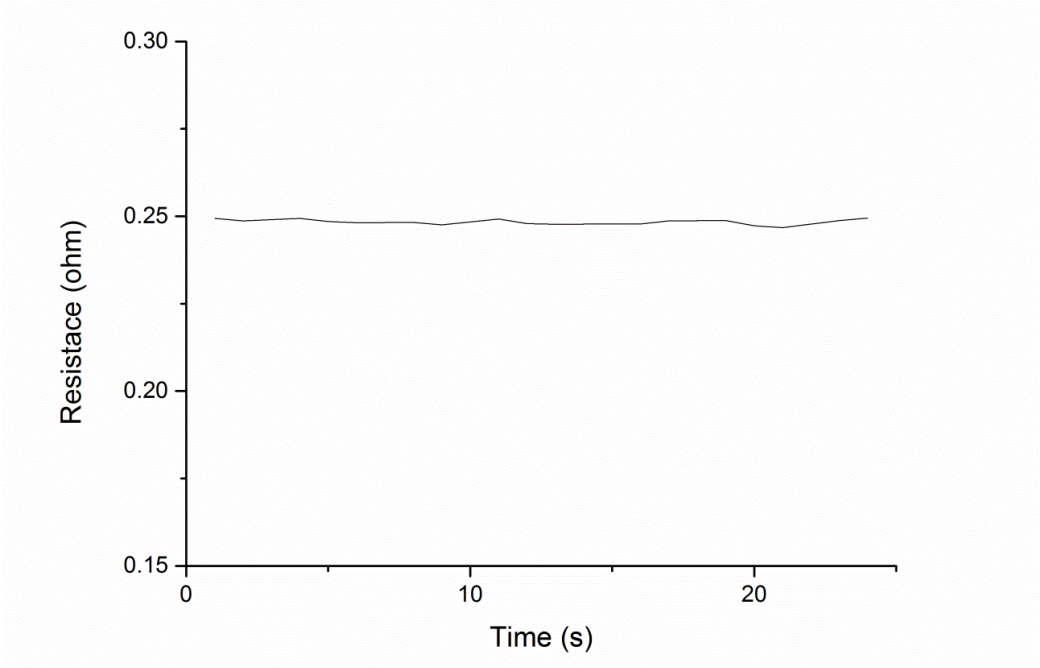

Fig.3. 35 Real-time resistance recording of copper track bending test

As shown in Fig.3.36, the resistance of vias increased immediately when occur to bending, represented by the peaks in real-time recordings. The resistance dropped sharply right after the bending and then decreased slowly to a certain value which is higher than the value before bending. The immediate increase in resistance was caused by the crack formation in the ICA or

the delamination between the ICA and the copper track which broke the conductive network and reduced the conductive paths. The recovery behaviour can be explained by the self-heal ability of ICA vias, and the accumulation of unhealable damages resulted in the eventual increase of resistance. Similar patterns were also observed when bending other test vehicles (Fig.3.37-3.40).

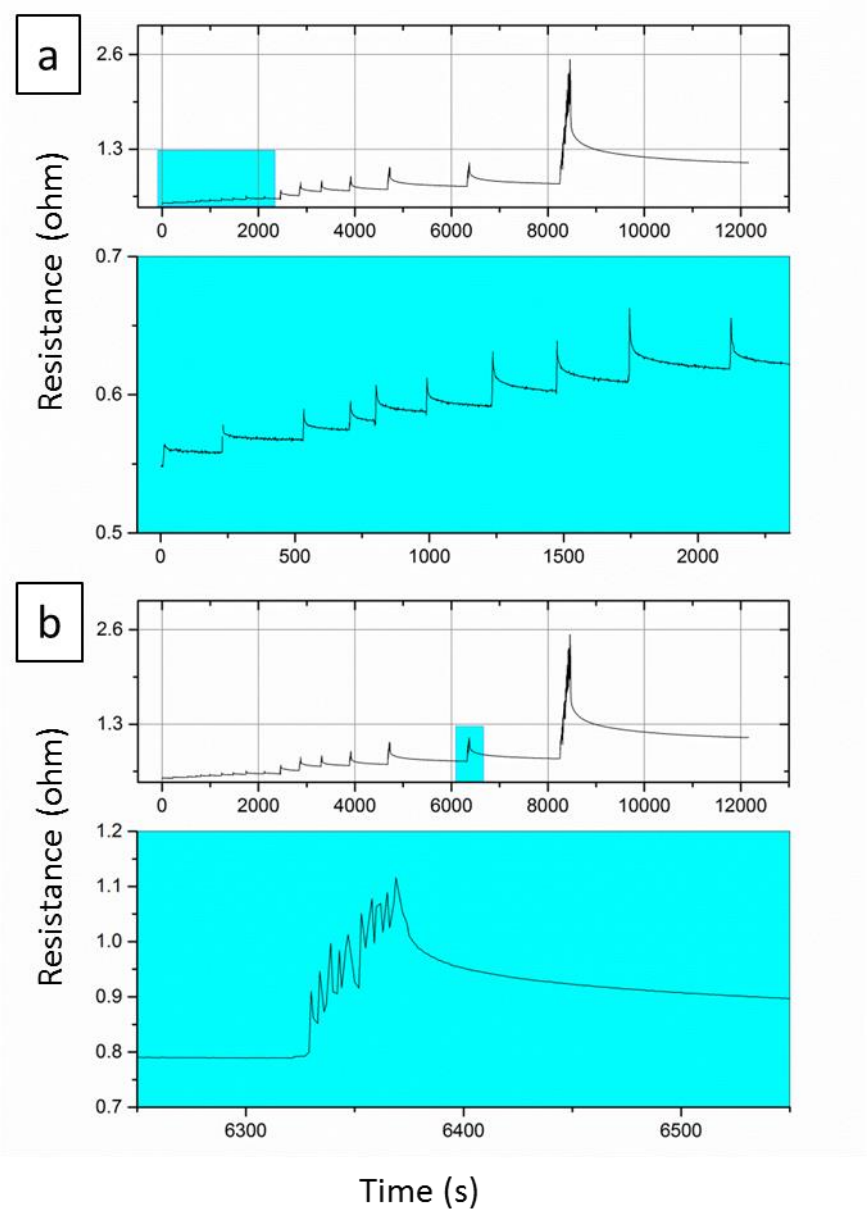

Fig.3. 36 The resistance of test vehicle with double 0.6mm-caps vias. The test vehicle was bent once and left for recovery, then repeated 9 times. Then it was bent 5 times and left for recovery, then repeated 3 times. The following are 10 times and 50 times bending. Blue box: a) bend once, b) ten times in a row

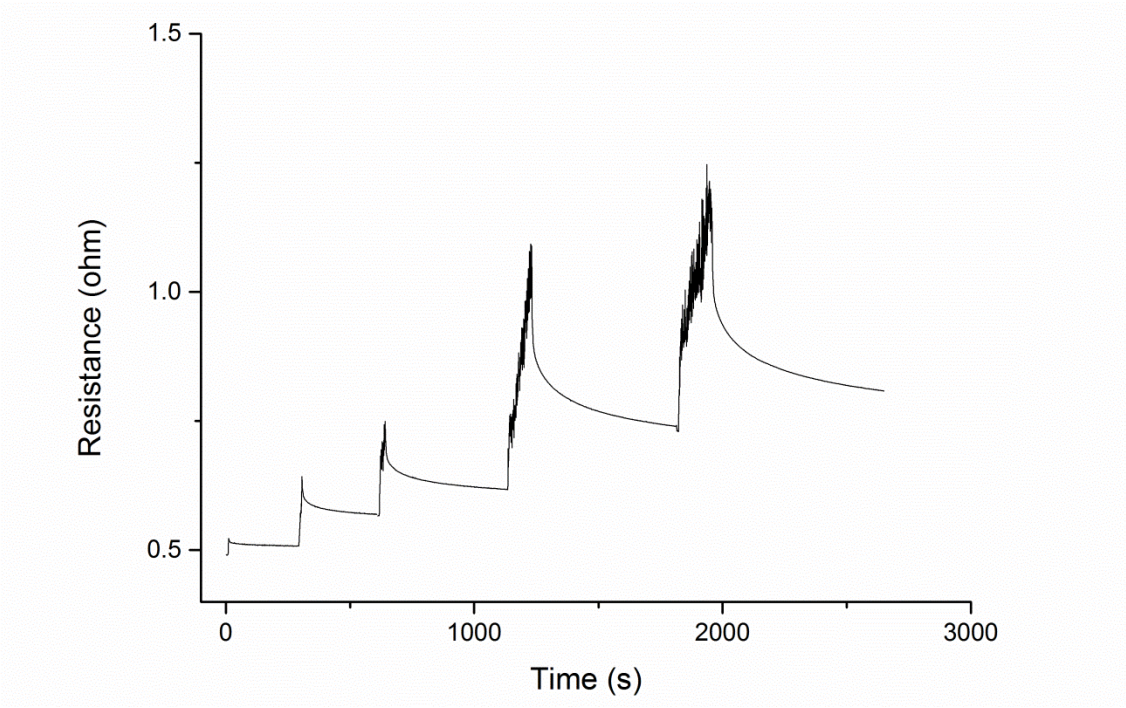

Fig.3. 37 The resistance of test vehicle with double 0.8mm-caps vias. The test vehicle was bent once and left for recovery, then bent 5 times and left for recovery, then bent 10 times and left for recovery. The following are 40 times and 50 times bending

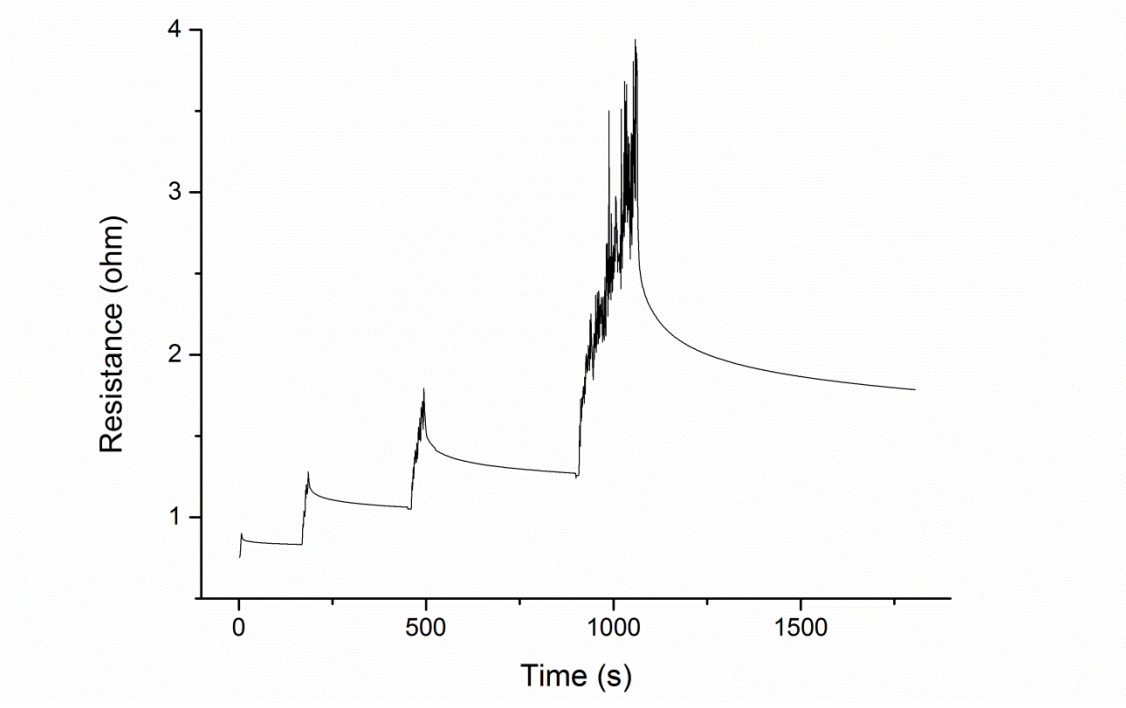

Fig.3. 38 The resistance of test vehicle with single 0.6mm-cap vias. The test vehicle was bent once and left for recovery, then bent 5 times and left for recovery, then bent 10 times and left for recovery. The final operation is 40 times bending.

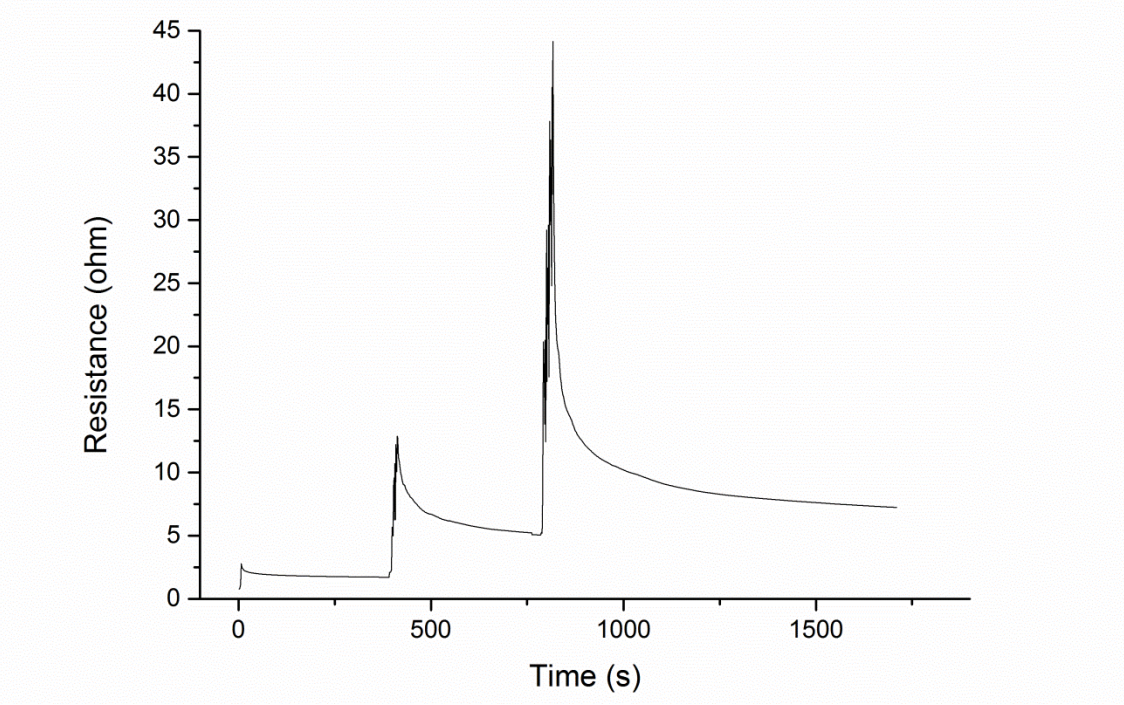

Fig.3. 39 The resistance of test vehicle with double 0.4mm-caps vias. The test vehicle was bent once and left for recovery, then bent 5 times and left for recovery, then bent 10 times and left for recovery.

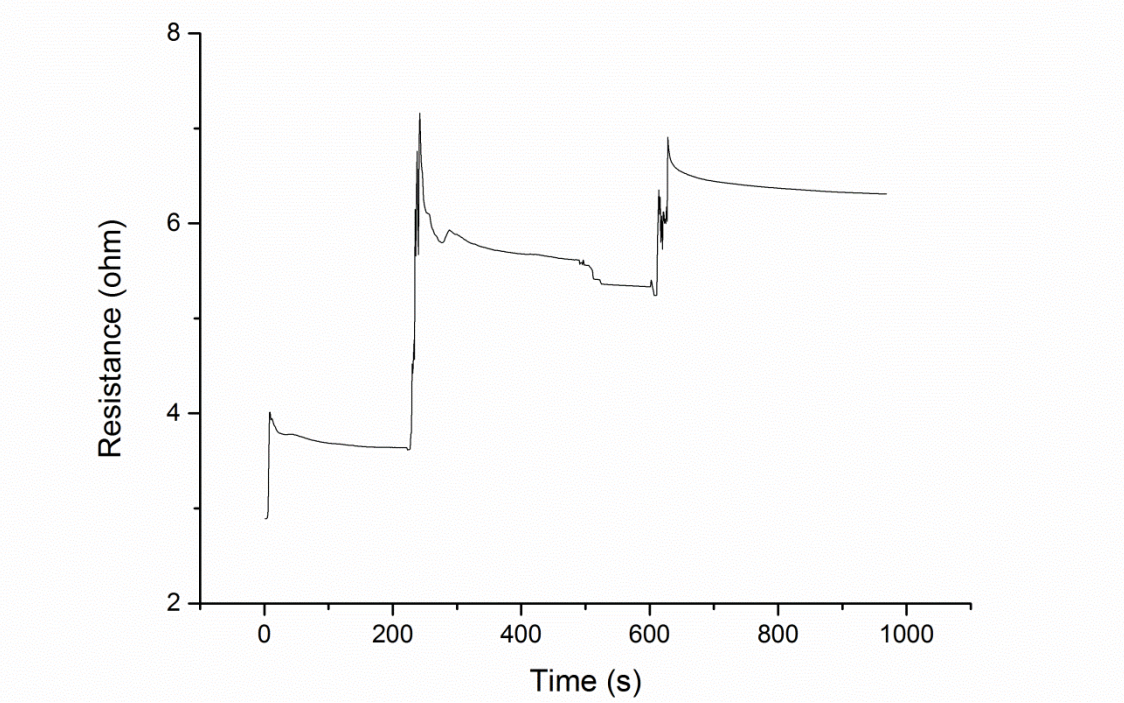

Fig.3. 40 The resistance of test vehicle with single 0.4mm-cap vias. The test vehicle was bent once and left for recovery, then bent 5 times in a row and left for recovery, finally bent 10 times in a row and left for recovery.

The resistance increments of test vehicles were differed after same bending cycles because of different initial resistance. Therefore, the percentages of resistance increase are compared in Table.3.7. It can be concluded that vias with large cap area and double caps structure performed better in bending.

Table.3. 7 The percentage of resistance increase of test vehicles after bending

	Number of times				
	1	6	16	56	106
Φ0.8mm Double caps	3.8%	16%	26.3%	51%	63%
Φ0.6mm Double caps	1.8%	7.8%	20%	50.5%	100.3%
Φ0.6mm Single cap	11.3%	40%	69.3%	137.3%	—
Φ0.4mm Double caps*	122%	562.3%	840.2%	—	—
Φ0.4mm Single cap	25.5%	83.8%	117.2%	—	—

* Loose contacts of one via joint in the test vehicle dramatically increased the total resistance after bending.

3.4 conclusions

The manufacture processes of test vehicles are developed and optimised to ensure the uniformity of ICA vias. A simplified model was built to represent rivet-shaped vias in the FPCBs. An equation was proposed to calculate the via fill resistance using geometry parameters. The relationship between the via resistance and cap size of the via was discussed. Vias with different cap sizes were fabricated and tested to validate the equation. The vias resistances decreased while the cap diameter increases, and the decline rate in resistance slowed down after the cap diameter overpass a certain value, like 0.5mm for researched test vehicles. For same cap size, the resistance of via with caps on both sides was lower than that with only one cap. Further work on contact resistance is needed to minimise the difference between theoretical and experimental result. Furthermore, those samples were divided into three groups

for thermal cycling test, damp heat ageing test and bending test. The results show that the via with large cap and double caps structure performed better under thermal or mechanical load.

Chapter 4 Curing effect on electrical performance of ICA vias

4.1 Introduction

In this chapter, the relationship between curing condition and vias performance was researched. Firstly, the ICA material itself was tested. The curing behaviour of the ICA was examined using differential scanning calorimetry (DSC) and thermogravimetry (TG)-differential thermal analysis (DTA). The degree of conversion of the ICA was estimated based on the DSC measurements. The glass transition temperature (Tg) and modulus of the ICA were measured by the dynamic mechanical analyser (DMA). Then the vias under different curing conditions were made and subjected to thermal shock test, heat and humidity ageing test and bending test.

4.2 Equipment and experimental details

4.2.1 Materials

The ICA used in this research is CircuitWorks Conductive Epoxy (CW2400). It is a two-part silver epoxy: Part A contains silver and epoxy resin, bisphenol-A-epichlorohydrin (number average molecular weight $\leqslant$ 700, CAS No. 25068-38-6), Part B contains silver and hardener, 2-piperazin-1-ylethylamine (CAS No.140-31-8).

4.2.2 Characterization of ICAs

4.2.2.1 Thermogravimetry-differential thermal analysis (TG-DTA)

Since the suggested pot life is 8-10 Minutes at 25^{o}C after mixing, equal amounts (1:1) by weight of Part A and Part B were mixed thoroughly for 2 minutes and immediately tipped into the Al_2O_3 ceramic crucible to run the test. The mass of the ICA in the crucible was 17.84mg. TG-DTA machine is NETZSCH STA449 F3. The sample was heated in a nitrogen atmosphere from 40 ^{o}C to 200 ^{o}C at a linear rate of 10 ^{o}C/min.

Fig.4. 1 TG-DTA machine NETZSCH STA449 F3

4.2.2.2 Differential scanning calorimetry (DSC)

DSC measures the energy absorption of a sample as it is subjected to a specified thermal profile [121]. The amount of heat contained in a material at any given time is known as its enthalpy. As additional thermal energy is supplied to the material, its enthalpy will increase. The rapid change in sample's enthalpy at a transition (i.e. melting, decomposition, curing, etc.) will cause a change in the amount of energy needed to be delivered which would appear in a DSC scan [117, 121]. Therefore, DSC measurements were utilised to monitor the cure of ICAs. The calorimetric measurements were performed with a Pyris Diamond DSC (PerkinElmer Instruments) supported by a PerkineElmer computer for data acquisition. The samples were prepared in the same way as TG-DTA test but tipped in aluminium pans. Experiments were conducted from 40 ^{o}C to 200 ^{o}C with different heating rates (5, 15 and 30 ^{o}C/min) in a nitrogen flow of 40 mL/min. The sample and reference are separated from each other and have their individual heaters and temperature sensors. The temperature difference between the sample and reference is eliminated by supplying differential thermal power [118]. This unique power compensation approach yields true heat flow measurements.

In the application of DSC technique, the conversion percentage is determined as

$$\alpha = \left(\frac{\Delta H_t}{\Delta H_{total}}\right) \times 100 \qquad 4.1$$

The reaction rate, $d\alpha/dt$, is proportional to heat flow:

$$\frac{d\alpha}{dt} = \frac{(dH/dt)}{\Delta H_{total}} \quad 4.2$$

Where, dH/dt is the heat flow rate at time t. ΔH_t represents the partial heat of the cure at time t and ΔH_{total} is the total heat of the cure.

The reaction rate in kinetic analysis can also be described as:

$$\frac{d\alpha}{dt} = K(T)f(\alpha) = A\,exp\left(-\frac{E}{RT}\right)f(\alpha) \quad 4.3$$

Where $K(T)$ is a temperature-dependent reaction rate constant, $f(\alpha)$ is dependent kinetic model function, A is the pre-exponential factor, E is activation energy, R is the universal gas constant, and T is the temperature in Kelvin.

Fig.4. 2 Pyris Diamond DSC

4.2.2.3 Dynamic mechanical analyser (DMA)

Test samples were cured under three different conditions: 100 °C for 6 minutes, 100 °C for 10 minutes, and 150 °C for 6 minutes. The dimensions of the cylindrical samples are 0.95mm high and 6mm in diameter. Diamond DMA （PerkinElmer Instruments）was used to obtain the storage modulus and loss factor (tan δ) of the specimens. Compression mode was applied with heating rate 2 °C /min from 25 to 200 °C at a single oscillation frequency 1 Hz.

Fig.4. 3 Diamond DMA

4.2.2.4 Field Emission Gun Scanning Electron Microscopy (FEGSEM)

Scanning electron microscope (SEM) was employed to reveal the structure and status of ICAs which were cured under different conditions.

4.2.3 Experiments on ICA filled vias

All the test vehicles with same via geometry, double Φ0.6 mm caps, were made by stencil printing. They were cured under different temperatures and time periods: 50°C for 6 minutes, 50°C for 10 minutes, 100°C for 6 minutes, 100°C for 10 minutes and 150°C for 6minutes. Resistance measurement, thermal cycling test, damp heat test and bending test were also conducted following the methods described in Chapter 3.

4.3 Results and discussion

4.3.1 Weight fractions of Ag in ICAs

Since the volume percentages of the studied ICA are not given in the datasheet, they have to be calculated.

$$\rho_{\mathrm{ICA}} = \mathrm{SG} \times \rho_{H2O} = 2.85\ \mathrm{g}/cm^3$$

Where SG is the specific gravity of the ICA, SG=2.85 (Appendices 3), ρ_{H2O} was the density of water at 4°C, $\rho_{H2O} = 1\ g/cm^3$

The volume percentage can be calculated with the rule of mixture for densities of composite materials:

$$\rho_{\mathrm{ICA}} = \rho_{\mathrm{Ag}} \times V_{Ag} + \rho_{\mathrm{poly}} \times V_{poly} \qquad 4.4$$

$$\rho_{\mathrm{poly}} = \frac{\rho_A + \rho_B}{2} = 1.08\ \mathrm{g}/cm^3$$

$$\rho_{\mathrm{Ag}} = 10.49\ \mathrm{g}/cm^3\ [122]$$

Where ρ_A is the density of polymer in Part A [123], ρ_B is the density of polymer in Part B [124]. Therefore, V_{Ag} = 18.8% and V_{poly} = 81.2%, corresponding weight fractions (wt%) are 69.2% and 30.8% respectively.

4.3.2 Curing kinetics of ICAs

Figure 4.4 shows the results of TG-DTA scans of the uncured ICA. The right ordinate scale indicates mass loss in percent of original mass. An exothermic peak (peak max: ~110 °C) due to the curing reaction of the ICA can be observed in the temperature range between 85 °C and 150 °C in the DTA curve.

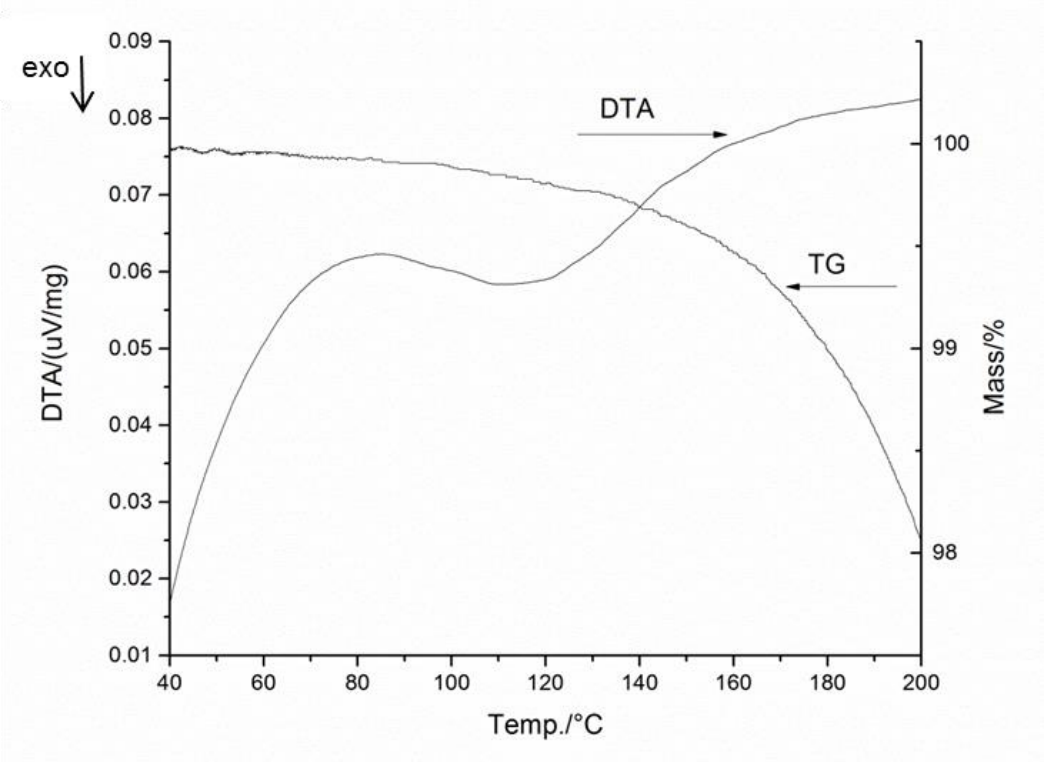

Fig.4. 4 TG-DTA curves of ICA sample under a heating rate of 10 °C/min

Table.4. 1 Impact of vaporisation in TG-DTA scan

Temperature range (°C)	Mass reduction	Heat of vaporisation (kJ/kg)	Heat absorption of Ag-epoxy (kJ/kg)	Impact on thermal profile
40-150	0.40%	1.80	51.81	3.47%
150-180	0.60%	2.70	14.13	19.11%
180-200	0.95%	4.28	9.42	45.44%

Note：Specific heat capacity of Ag: 0.235 kJ/kg [125], specific heat capacity of epoxy: 0.100 kJ/kg [125]. The specific heat of vaporisation: 450 kJ/kg [126]. Specific heat capacity of Ag-epoxy was calculated according to weight fractions: 0.471 kJ/kg.

A decrease in weight of the ICA was observed in the TG curve. This decrement in weight (<2 %) was caused by the vaporisation of water and additives that are contained in the ICA. As shown in Table 4.1, the vaporisation had a neglectable impact [127] on the thermal profile when the temperature was rising from 40 °C to 150 °C. Though the impact became significant after 180 °C, the DSC analysis wouldn't be affected as the cure reaction was already finished after 150 °C.

According to DSC curves obtained at different heating rates, the initial curing temperature (T_i), the peak temperature (T_p), the finishing temperature (T_f), the curing reaction range, duration and the change in enthalpy (ΔH) are summarised in Table 4.1. The analysis is based on the theory that the heat generated during the reaction is equal to the total area under the heat flow versus time curve.

Table.4. 2 Curing characteristics evaluated from DSC curves

Heating rate ∅	T_i (°C)	T_p(°C)	T_f(°C)	Curing range (°C)	Curing duration (min)	ΔH (J/g)
5 °C/min	32.91	73.61	121.02	88.11	17.6	26.66
15 °C/min	36.15	90.76	141.27	105.12	7	26.01
30 °C/min	54.52	104	174.43	119.91	4	27.42

To eliminate the influence of heating rate, the data were linear fitted (Fig.4.5), then T_i, T_p, and T_f of the ICA can be determined by extrapolating to $\emptyset = 0$. The extrapolated T_i, T_p, and T_f were 26.3 °C, 69.6 °C and 109.9 °C respectively. T_i is near room temperature, which proves that the studied ICA could be a room-temperature curing adhesive. The curing reaction can be carried out at low temperature over long periods of time, or performed at high temperature within a short period of time. The conversion of ICA in DSC scanning was calculated as a function of time and plotted in Fig.4.6.

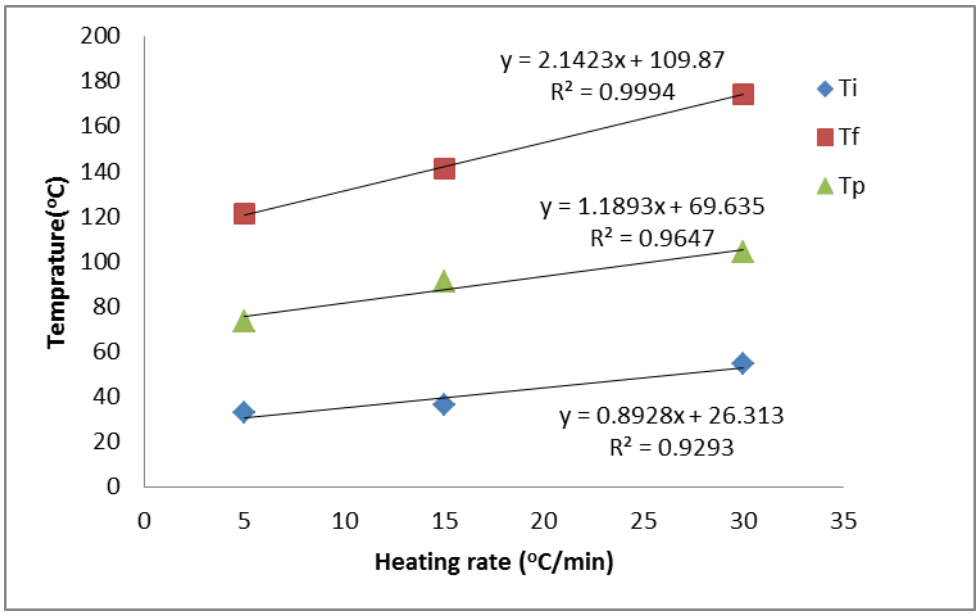

Fig.4. 5 Plots of characteristic cure temperatures for ICA at different heating rates.

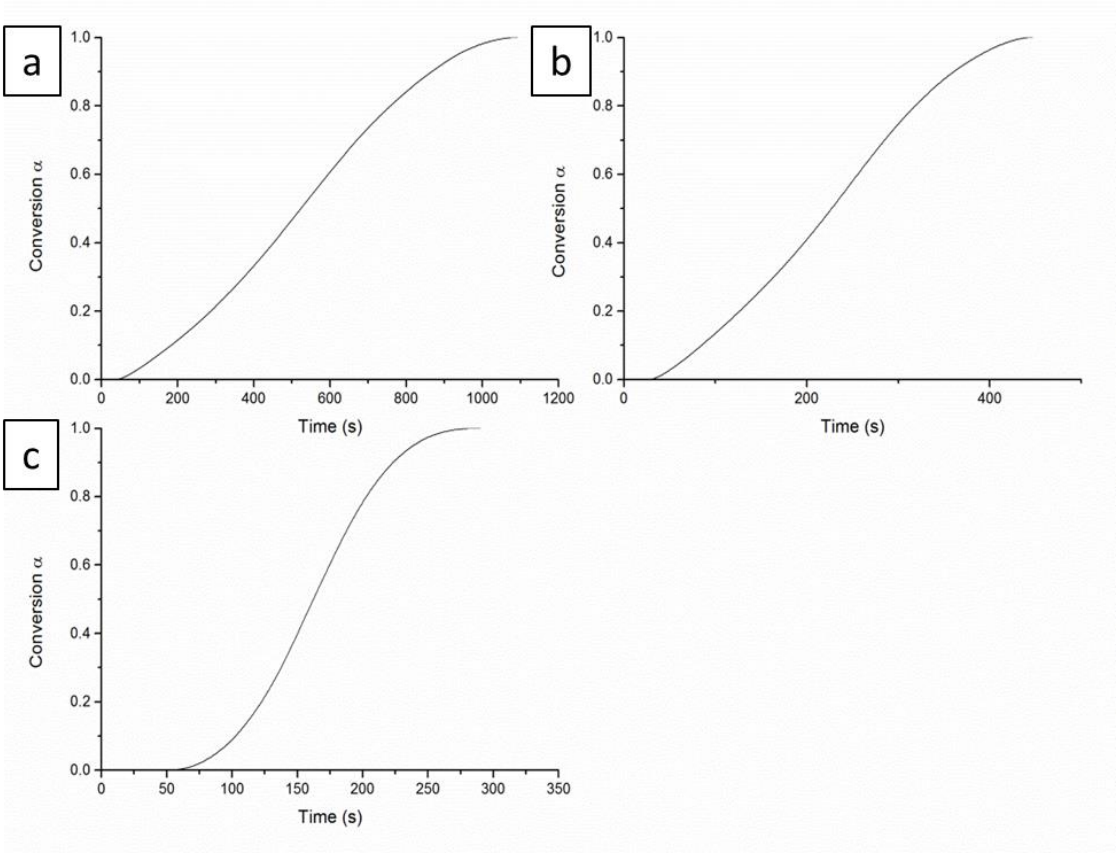

Fig.4. 6 Fractional conversion as a function of time, heating rate: a) 5 °C/min, b) 15 °C/min and c) 30 °C/min

Firstly, the ICA curing is assumed as a nth-order reaction [117, 128].

Nth-order kinetic: $$f(\alpha) = (1-\alpha)^n \quad 4.5$$

Where n is the reaction order, $(1-\alpha)$ represents the uncured epoxy, thus, the reaction rate depends the concentration of epoxy functional groups in ICAs.

The combination of Kissinger method and Crane method is a way to rapidly determine the reaction order n and the kinetic equation. The apparent activation energy E_a can be estimated by Kissinger method:

$$\ln\frac{\emptyset}{T_p^2} = \ln\frac{AR}{E_a} - \frac{E_a}{RT_p} \quad 4.6$$

$$\frac{d\left(\ln\frac{\emptyset}{T_p^2}\right)}{d\left(\frac{1}{T_p}\right)} = -\frac{E_a}{R} \quad 4.7$$

Where ∅ is the heating rate, T_p is the peak temperature and R is the gas constant, 8.314 J mol^{-1} K^{-1}. The peak temperatures at different heating rates are identified from DSC curves.

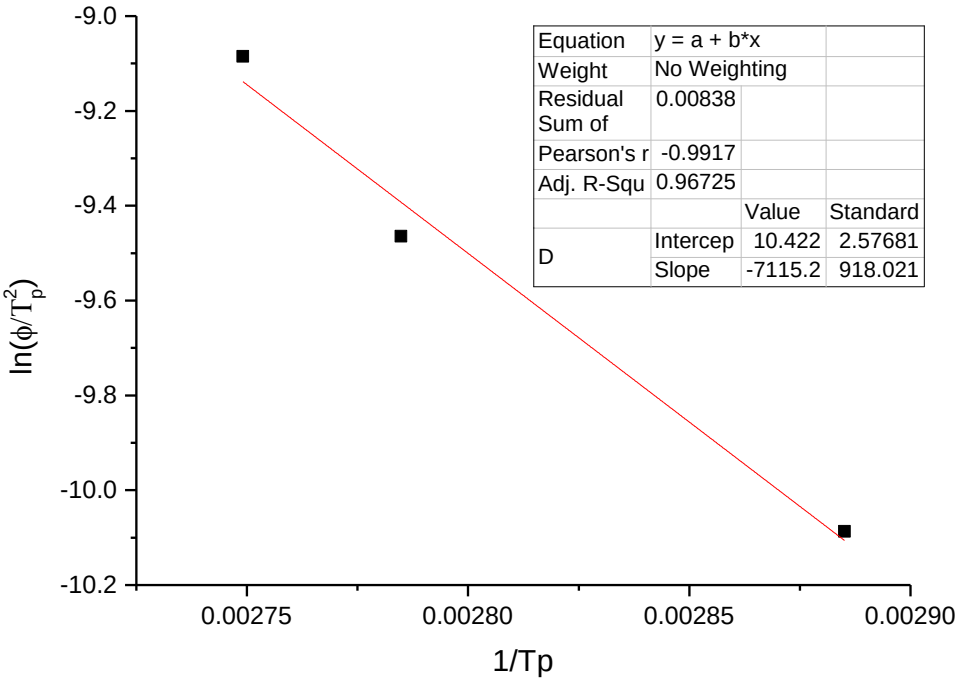

Fig.4. 7 The linear fit of $\ln\frac{\emptyset}{T_p^2}$ versus $\frac{1}{T_p}$

The slope of $\ln\frac{\emptyset}{T_p^2}$ versus $\frac{1}{T_p}$ in the Fig.4.7 equals $-\frac{E_a}{R}$ and the intercept equals $\ln\frac{AR}{E_a}$. Therefore,

$$E_a = -R \times -7115.2 = 59.2 \text{ kJ mol}^{-1}$$

$$\text{A} = \text{e}^{10.442} \times \frac{E_a}{R} = 2.4 \times 10^8$$

Then the reaction order n is calculated by substituting the apparent activation energy E_a into Crane equation:

$$\frac{d(\ln \emptyset)}{d\left(\frac{1}{T_p}\right)} = -\frac{E_a}{nR} \qquad 4.8$$

The slope of $\ln \emptyset$ versus $\frac{1}{T_p}$ is -7824.36 (Fig.4.8), thus

$$\text{n} = \frac{59200}{8.314 \times 7824.36} = 0.91$$

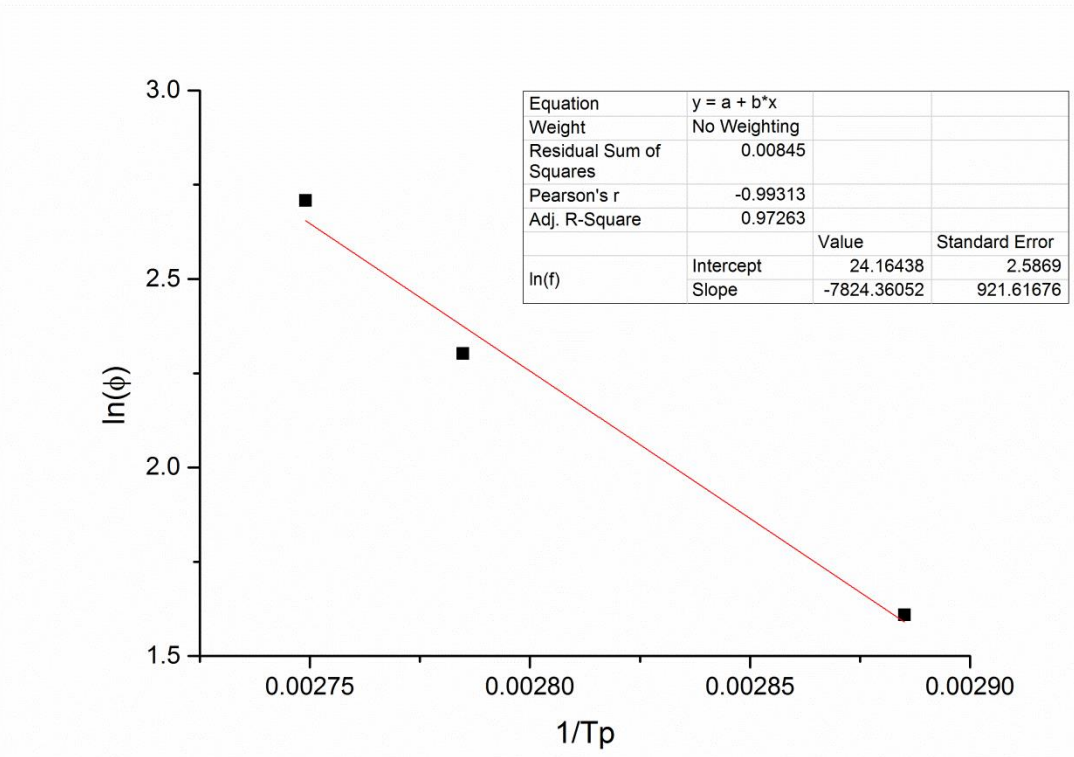

Fig.4. 8 The linear fit of ln ϕ versus $\frac{1}{T_p}$

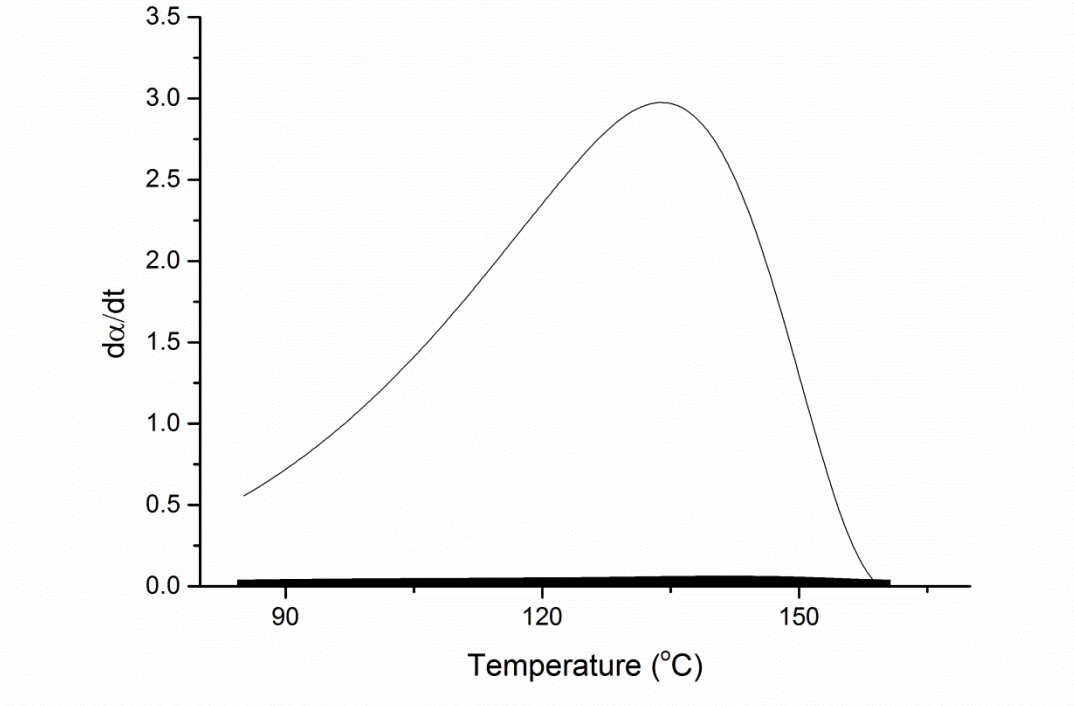

Fig.4. 9 Comparison of experimental (thick line) and calculated (thin line) DSC curve

According to the parameters calculated above, the nth-order cure kinetic equation is presented as:

$$\frac{d\alpha}{dt} = 2.4 \times 10^8 \, exp\left(-\frac{59200}{RT}\right)(1-\alpha)^{0.91} \qquad 4.9$$

The DSC curve calculated by nth-order cure kinetic equation is quite different from the experimental DSC curve (Fig.4.9). The nth-order kinetic model can't describe this ICA curing process properly. Therefore Malek method [117, 129, 130] is used to determine the kinetic model.

In Malek method, the apparent activation energy E_a is determined by iso-conversional method. Using the logarithmic form of the kinetic equation (Eq.4.3)

$$\ln\frac{d\alpha}{dt} = \ln[Af(\alpha)] - \frac{E_a}{RT} \qquad 4.10$$

For each given α, the slope of $\ln\frac{d\alpha}{dt}$ versus 1/T determines the value of E_a.

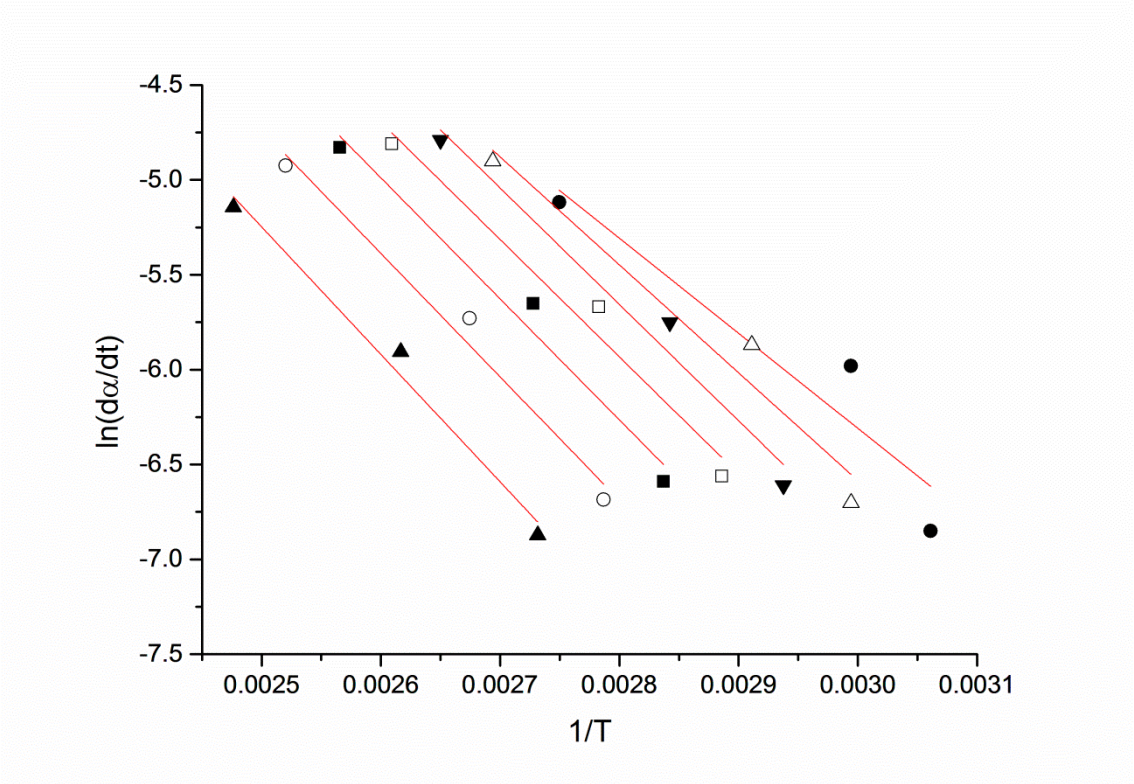

Fig.4. 10 The plot of $\ln\frac{d\alpha}{dt}$ versus 1/T , (▲) α=0.8, (○) α=0.7, (■) α=0.6, (□) α=0.5, (▼) α=0.4, (Δ) α=0.3, (●) α=0.2

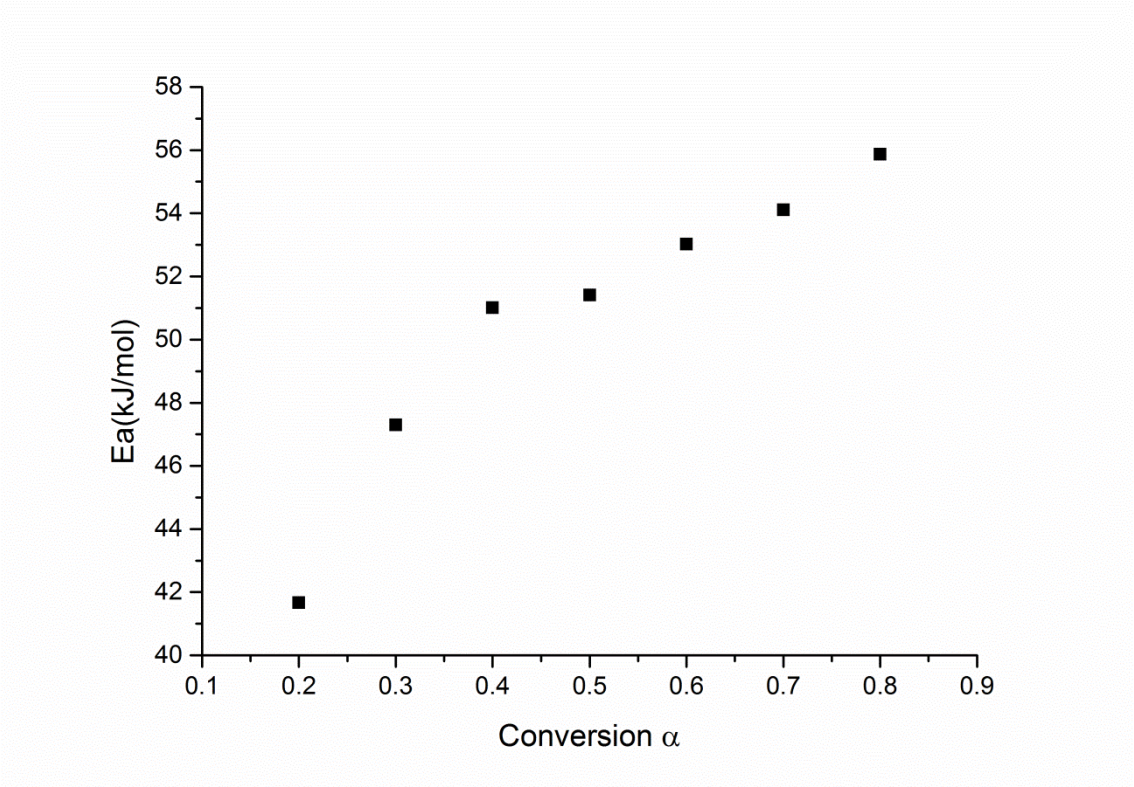

Fig.4. 11Dependencies of the activation energy E_α on conversion α

The activation energy $\boldsymbol{E_a}$ depends not only on temperature but also on the reaction mechanism and the diffusion rate of reactive groups [131]. As shown in Fig.4.11, $\boldsymbol{E_a}$ varies with the extent of conversion α. The initial activation energy $\boldsymbol{E_a}$ was very low because the initial viscosity of the mixture was very low. Low viscosity leads to better mixing and hence better reaction. An increase in $\boldsymbol{E_a}$ was observed with the elevation of conversion. Then, $\boldsymbol{E_a}$ kept steady with increasing in conversion, as the autocatalytic effect grew important. The OH groups generated by the epoxy-amine reaction lead to the autocatalysis which lower the activation energy [127, 131]. In high conversion region, $\boldsymbol{E_a}$ gradually increased due to the high diffusion resistance, as the aggregating silver particles start to decrease the mobility of polymer and the molecular weights increased continually. The average value of $\boldsymbol{E_a}$ was calculated to be 50.69 kJ/mol.

Two special functions, $y(\alpha)$ and $z(\alpha)$, are introduced in the determination of the kinetic model function $f(\alpha)$.

$$y(\alpha) = \left(\frac{d\alpha}{dt}\right) e^{x} \tag{4.11}$$

$$z(\alpha) = \pi(x) \left(\frac{d\alpha}{dt}\right) \frac{T}{\emptyset} \tag{4.12}$$

Where $x = E_a/RT$ is the reduced activation energy, and $\pi(x)$ is an approximation of the temperature integral. The rational expression is

$$\pi(x) = \frac{x^3+18x^2+88x+96}{x^4+20x^3+120x^2+240x+120} \quad 4.13$$

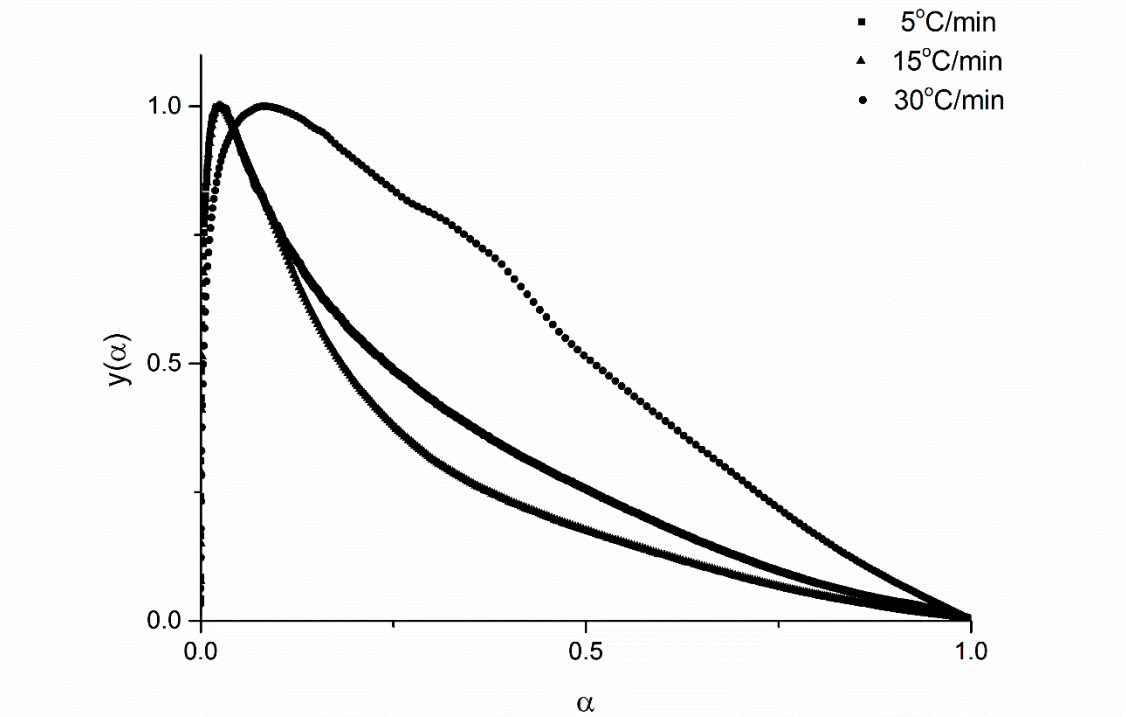

Fig.4. 12 Variation of y(α) function versus conversion

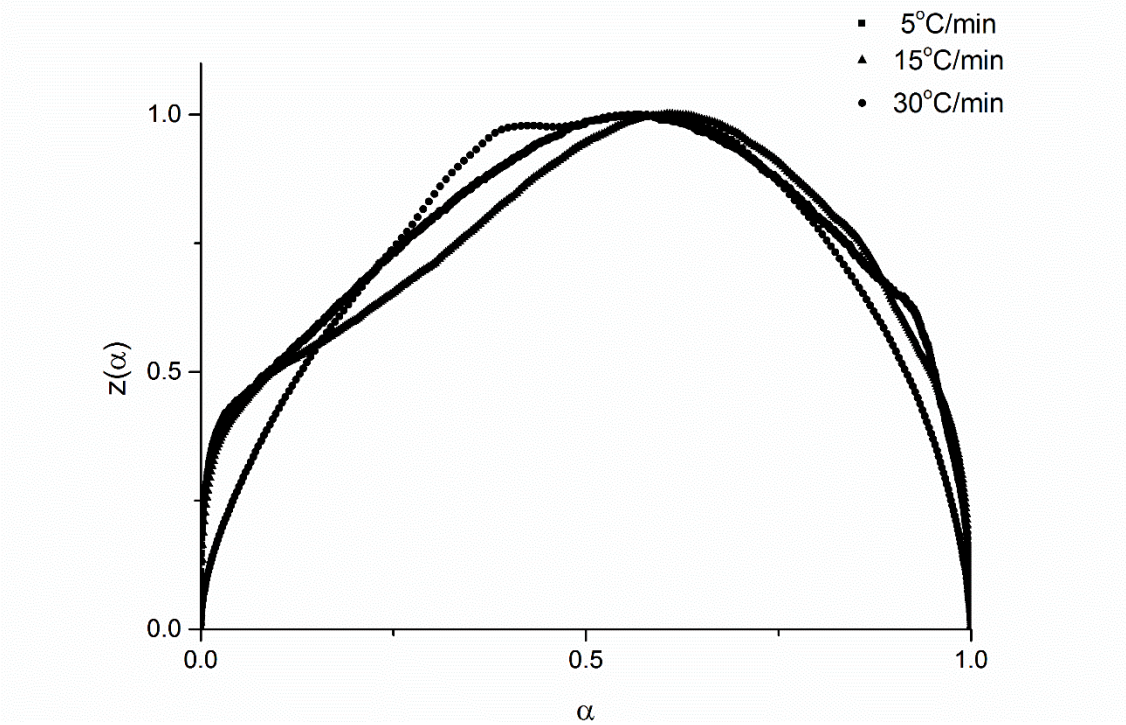

Fig.4. 13 Variation of z(α) function versus conversion

The functions $y(\alpha)$ and $z(\alpha)$ reach the maxima at α_M and α_P^{∞}, respectively. α_P is the fractional conversion at the peak of DSC curves. As shown in Table 4.2, the values of α_M are lower than the values of α_P, and the values of α_P^{∞} are lower than 0.632. These criteria indicate that the kinetic data can be described by the Sestak-Berggren model.

Table.4. 3 Characteristic values obtained from $y(\alpha)$, $z(\alpha)$ and DSC curves

Heating rate ∅ (ºC/min)	α_M	α_P^{∞}	α_P
5	0.025	0.567	0.502
15	0.024	0.609	0.559
30	0.082	0.563	0.399

Sestak-Berggren model is a two-parameter autocatalytic kinetic model:

$$f(\alpha) = \alpha^m(1-\alpha)^n \qquad 4.14$$

where m and n are the kinetic exponents.

The kinetic exponent ratio, p=m/n, is calculated by using Eq.4.15:

$$p = \frac{\alpha_M}{1-\alpha_M} \qquad 4.15$$

Kinetic exponent n can be obtained using Eq.4.16. and then $m = pn$.

$$\ln[(d\alpha/dt)e^x] = \ln A + n\ln[\alpha^p(1-\alpha)] \qquad 4.16$$

As shown in Fig.4.14, the slope is n and the intercept is lnA.

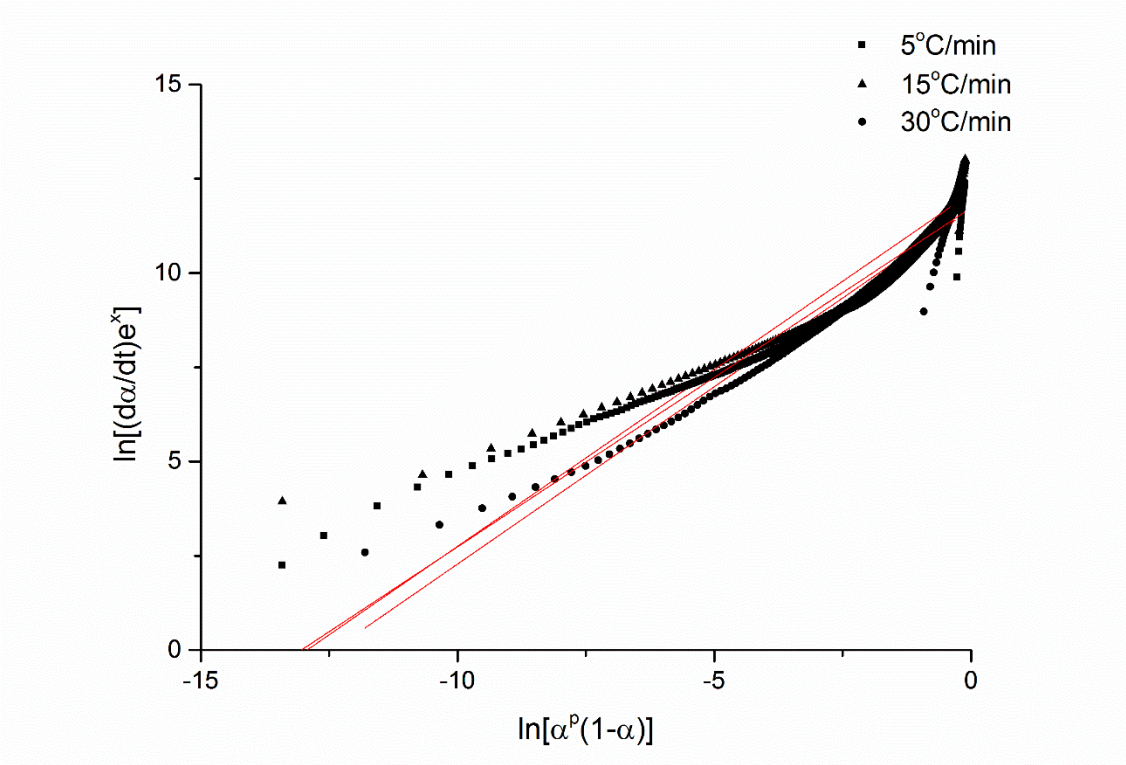

Fig.4. 14 Variation of $\ln[(d\alpha/dt)e^{x}]$ versus $\ln[\alpha^{p}(1-\alpha)]$

Table.4. 4 The kinetic parameters evaluated for the curing of ICA

Heating rate ∅ (ºC/min)	E_a (kJ/mol)	lnA	m	n
5	50.69	11.72	0.023	0.899
15		11.92	0.022	0.897
30		11.69	0.048	0.941
Mean		11.78	0.031	0.912

Based on the parameters obtained above, the kinetic equation is delivered:

$$\frac{d\alpha}{dt} = 1.306 \times 10^{5}\, exp\left(-\frac{50690}{RT}\right)\alpha^{0.031}(1-\alpha)^{0.912} \qquad 4.17$$

This equation expresses the rate of conversion $(\frac{d\alpha}{dt})$ as a function of conversion α and temperature T. $(1-\alpha)^{0.912}$ represents the reaction catalysed by the groups initially present and

consumed by the reaction. $\alpha^{0.031}$ indicates reaction products act as catalysts for the continuing reaction associated with the autocatalysis by the -OH groups generated by the epoxy amine reaction [127, 131].

The correctness of the kinetic model is verified by comparing experimental curves and calculated curves in the plot of dα/dt versus temperature. It is observed in Fig.4.15 that the two-parameter Sestak-Berggren model well describes the studied curing process.

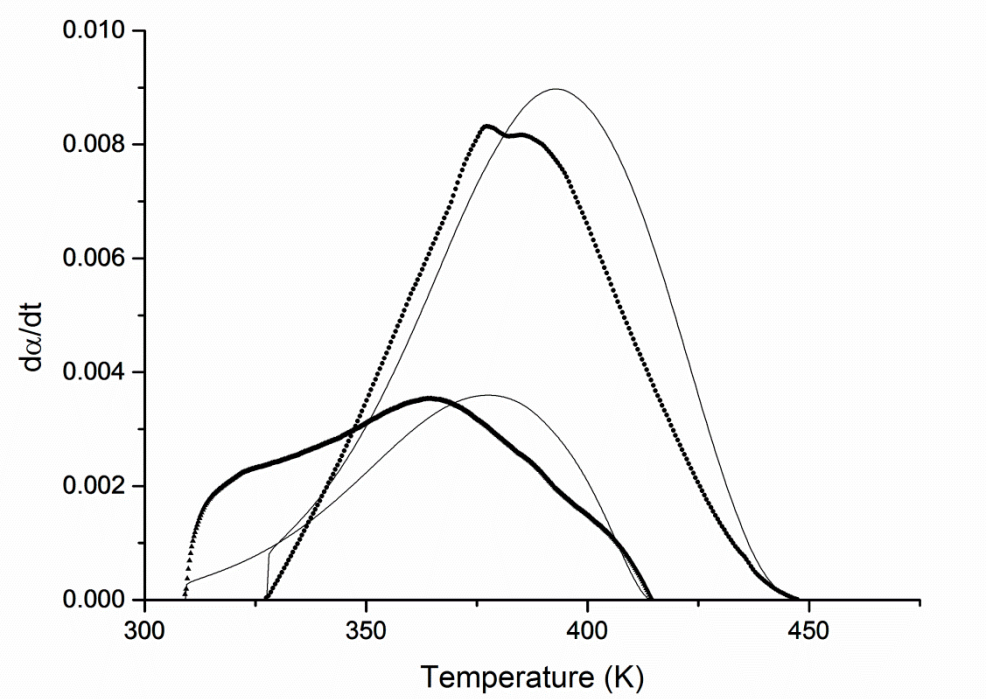

Fig.4. 15 Comparison of experimental (dot lines) and calculated (solid lines) DSC curves (▲15°C/min and ● 30°C/min)

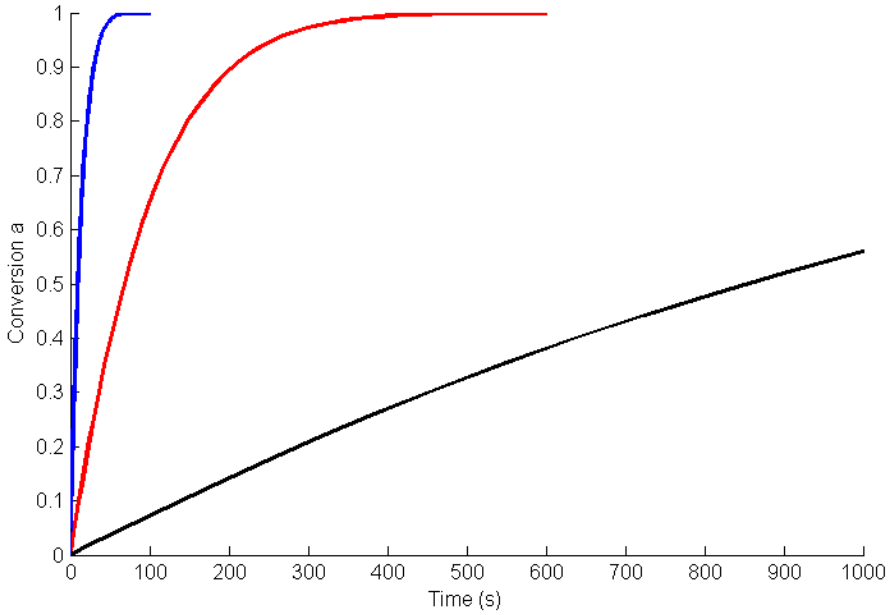

Fig.4. 16 Conversion vs. curing time at different temperatures (Blue line: 150 °C, Red line: 100 °C, Black line: 50 °C)

The kinetic equation can be used in roughly predicting the cure time at a given temperature (isothermal curing). Three cure temperatures (50, 100, and 150 °C) were chose for this study. As shown in Fig.4.16, it would take much more time to reach a certain conversion level when lower the curing temperature since the curing reaction is also a thermally activated process.

4.3.3 Mechanical properties of ICAs

The storage and loss modulus of ICAs shown in Table.4.4 are gained from DMA curves (Fig.4.17. A and B). The glass transition temperature (T_g) is determined by the peak position of tanδ curves (Fig.4.17.C).

Table.4. 5 Storage, loss modulus and T_g, according to DMA test, T_g values at 1 Hz.

Curing condition	Storage modulus (MPa)	Loss modulus (MPa)	T_g (°C)
6 min @ 100 °C	40.9	15.8	57.0
10 min @ 100 °C	71.4	17.9	61.8
6 min @ 150 °C	46.7	9.5	58.2

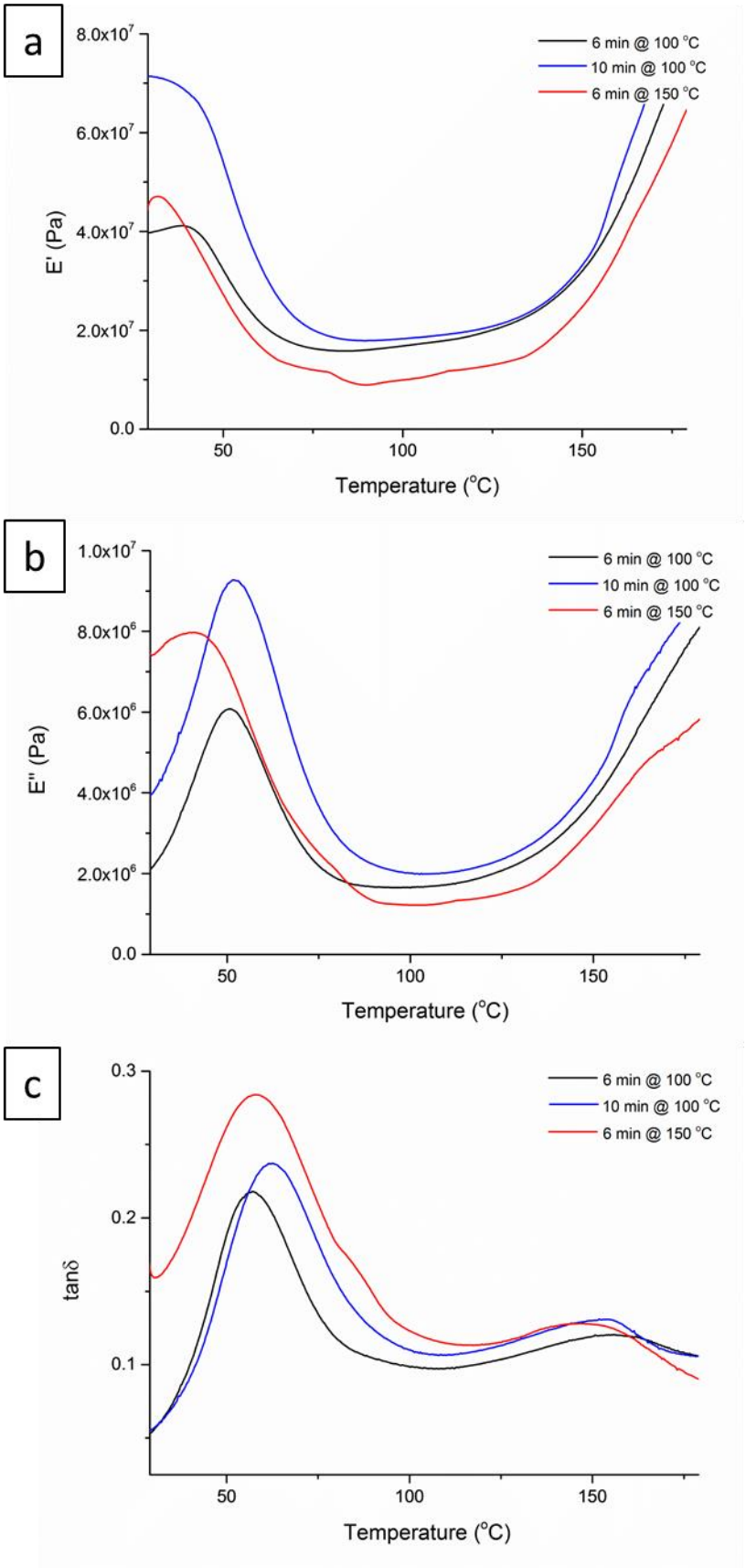

Fig.4. 17 DMA curves: a) Storage modulus E', b) Loss modulus E'', c) Loss factor tanδ

Since the mechanical strength is mainly provided by epoxy binders, the SEM photos of cured epoxy in ICA were taken for analysis. It can be seen from the SEM images, the epoxy resin cured at 100 ^{o}C for 6 minutes was in scaly structure (Fig.4.18. a). This kind of ICA is weak because the epoxy network formation is incomplete. After increasing the conversion level by prolonging the curing time, a dense epoxy network was formed (Fig.4.18. b) and the storage modulus increased. Some tiny holes in epoxy resin can be seen in the ICA sample cured at 150 ^{o}C for 6minutes (Fig.4.18.c). This is because the internal stress of epoxy resin was too high as it was over-shrinkage under high temperature and long curing time. These defects decrease the mechanical strength.

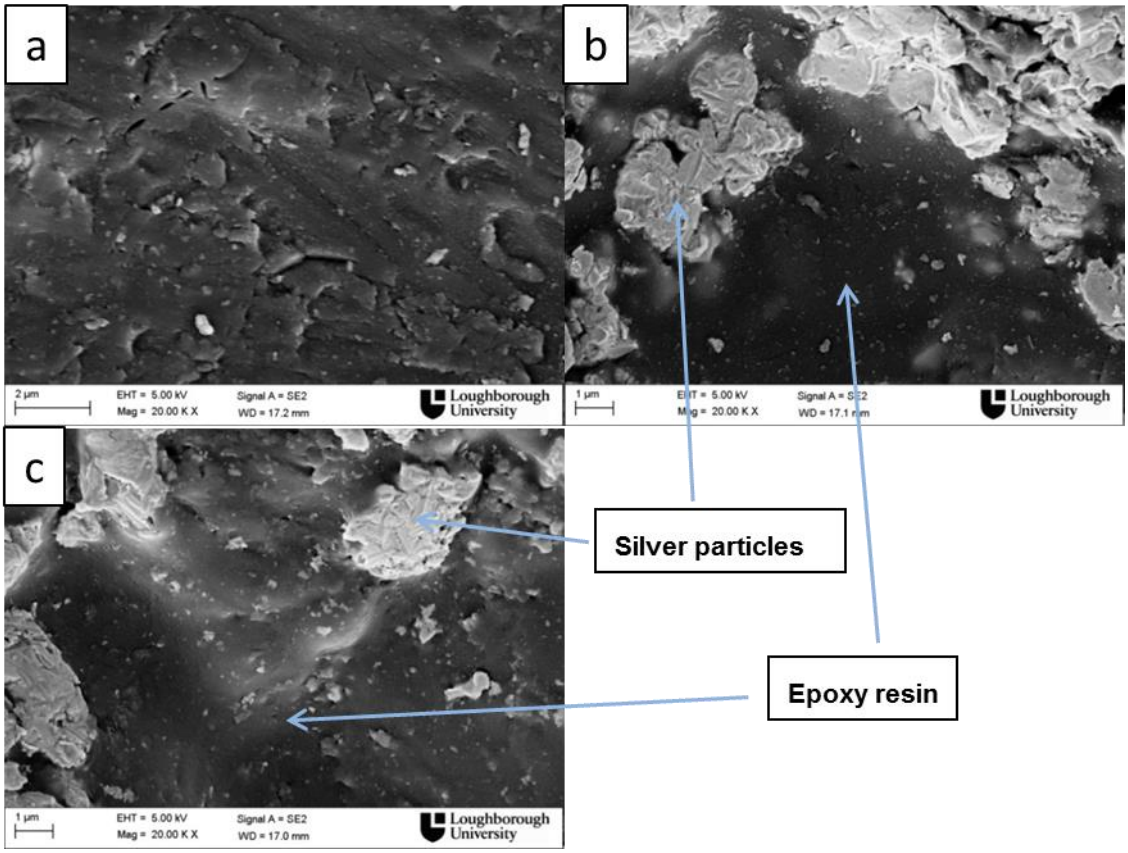

Fig.4. 18 SEM photos of ICA samples cured under different conditions. a) 6 min @ 100 ^{o}C, b) 10 min @ 100 ^{o}C, c) 6 min @ 150 ^{o}C

4.3.4 Resistances of ICA vias under different curing conditions

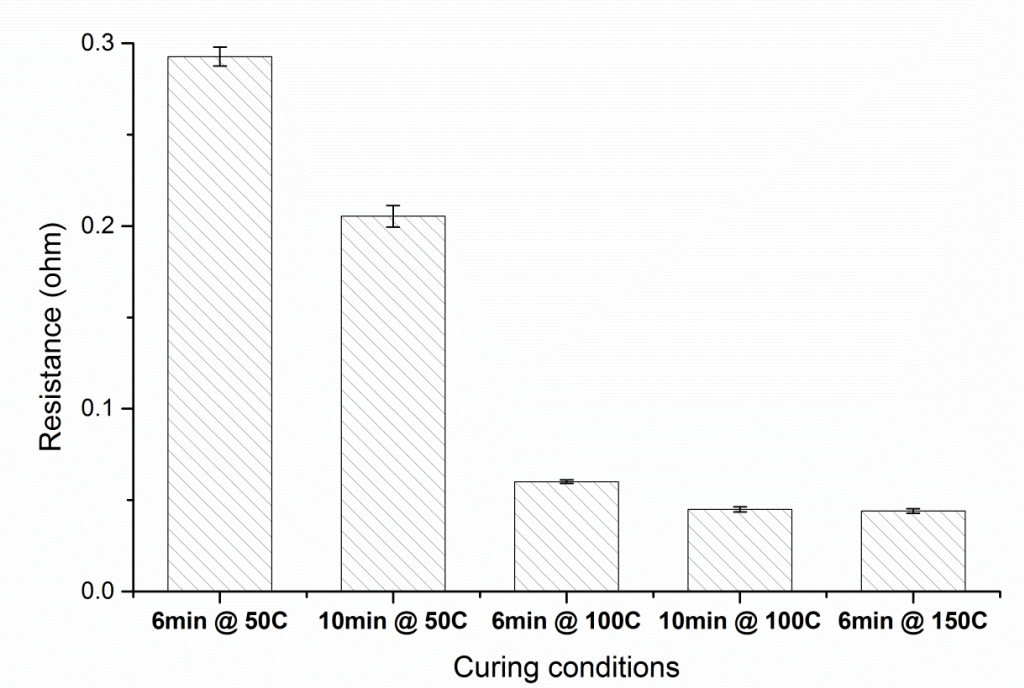

Fig.4. 19 Average via resistances of test vehicles

As shown in Fig.4.19, 100 ^{o}C and 6 minutes are the most economic curing parameters, saving both time and energy. The SEM photos (Fig.4.20) prove that the conductive particles were aggregated and formed more electrical contacts by the shrinkage of epoxy when increasing cure temperature and time. The closer contacts decreased the ICA resistivity thus lowered the via resistance.

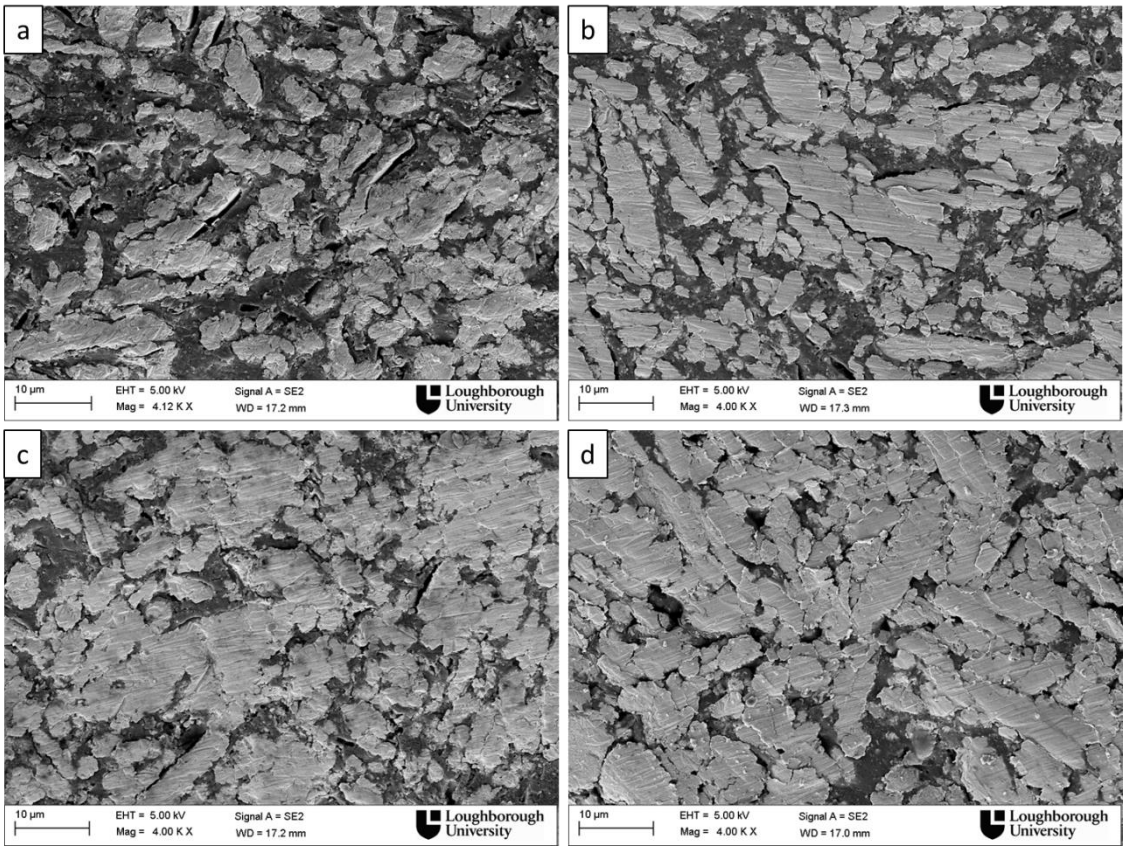

Fig.4. 20 Scanning Electron Microscope (SEM) photos of ICA samples cured under different conditions: a) 10 min @ 50°C, b) 6 min @ 100°C, c) 10 min @ 100°C, d) 6 min @ 150°C

4.3.5 Thermal cycling and damp heat ageing

The samples were post-cured at the hot stage of thermal cycles. Thus a decrease in resistance was observed at the early stage of the thermal shock test. For samples cured below 125 °C, higher the conversion level, lower the post-cure effect (Fig.4.21. a, b and c). The samples cured above 125 °C were affected slightly (Fig.4.21. d).

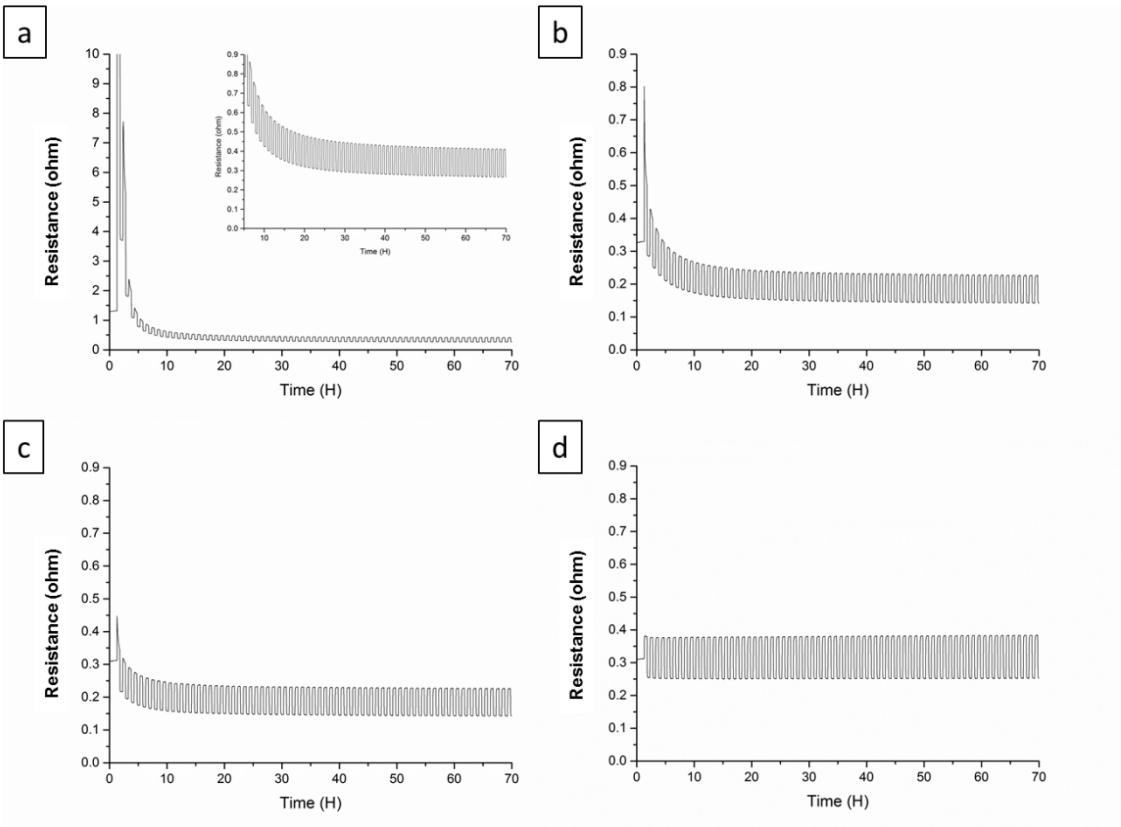

Fig.4. 21 Evolution of via resistance as a function of time exposed to temperatures cycles alternating between -40°C and 125°C. a) curing at 50°C for 10 minutes, b) curing at 100°C for 6 minutes, c) curing at 100°C for 10 minutes, d) curing at 150°C for 6 minutes

A similar pattern could also be observed in 85°C /85RH damp heat test. There was a significant post-cure effect on vias cured at 50°C. Despite the different start resistance, vias cured at 50°C for 6 or 10 minutes reached the similar resistance after 20 hours ageing.

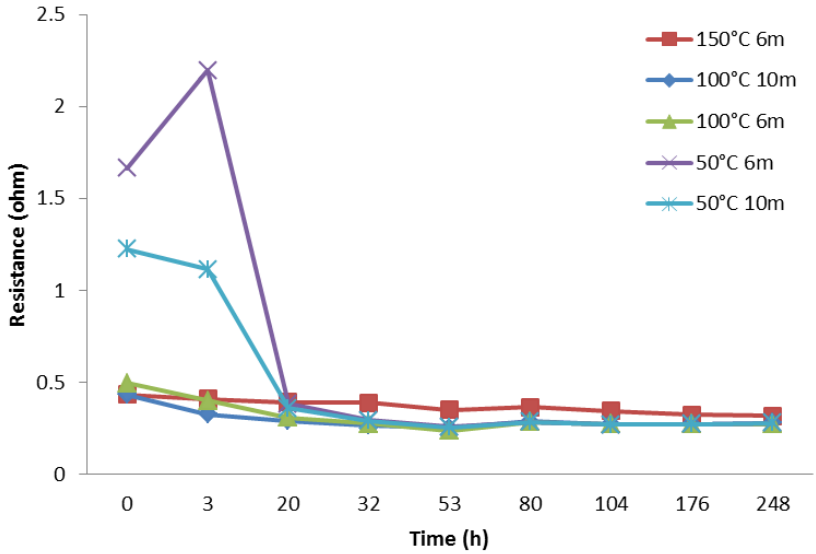

Fig.4. 22 Resistance evolution as a function of time at 85°C/85% RH

4.3.6 Mechanical bending

The resistance increments of test vehicle cured at 50 °C were much bigger than the test vehicles cured at 100 °C and 150 °C. It agrees with the material research above that the incomplete cured epoxy is weak and sparse particles network is vulnerable. Although the mechanical property of ICA cued at 100 °C was better, the resistance increments of vias cured at 100 °C in bending tests were larger than the vias cured at 150 °C. It because the Ag particles were more closely contacted in the vias cured at 150 °C, which weaken the impact of tiny cracks in epoxy.

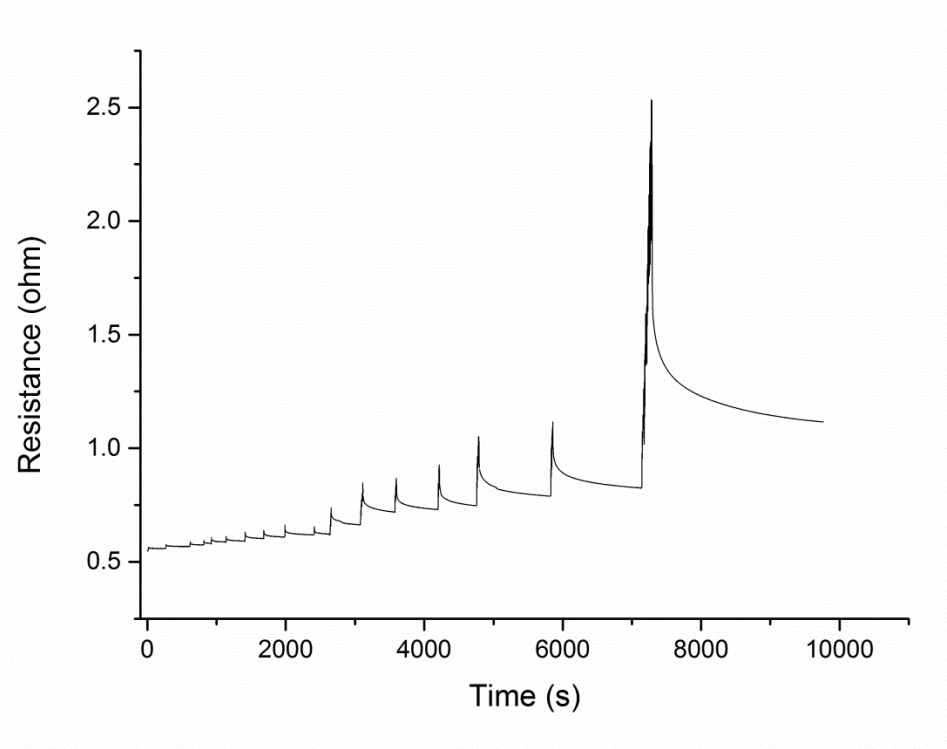

Fig.4. 23 Bending test of test vehicle cured at 100°C for 10min. (1,5,10,50 times in a row)

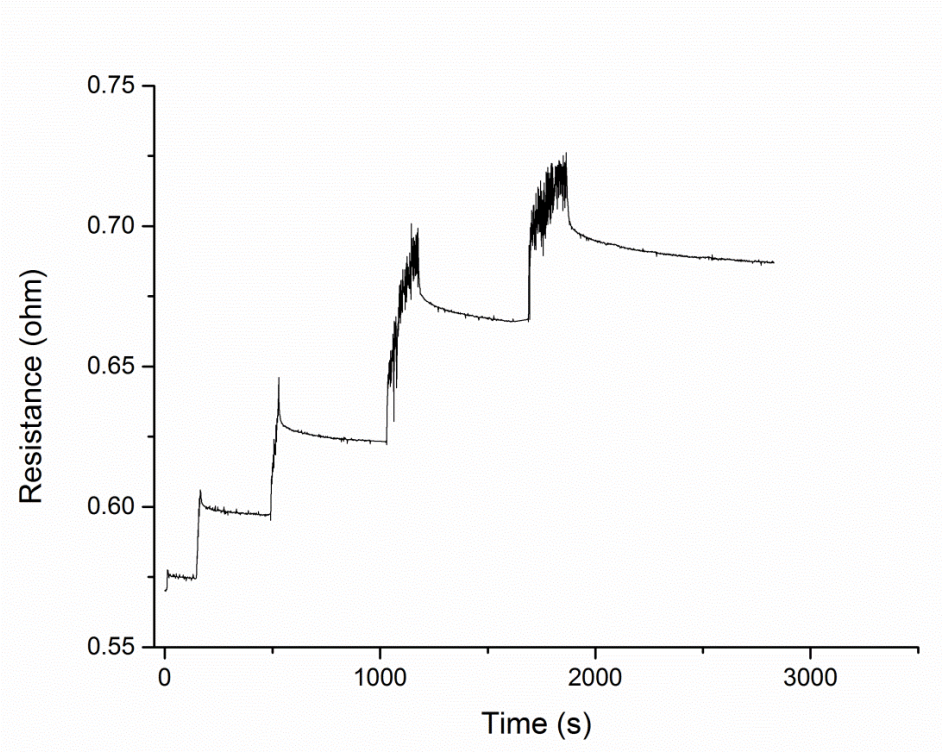

Fig.4. 24 Bending test of test vehicle cured at 150°C for 6min. (1,5,10,40,50 times in a row)

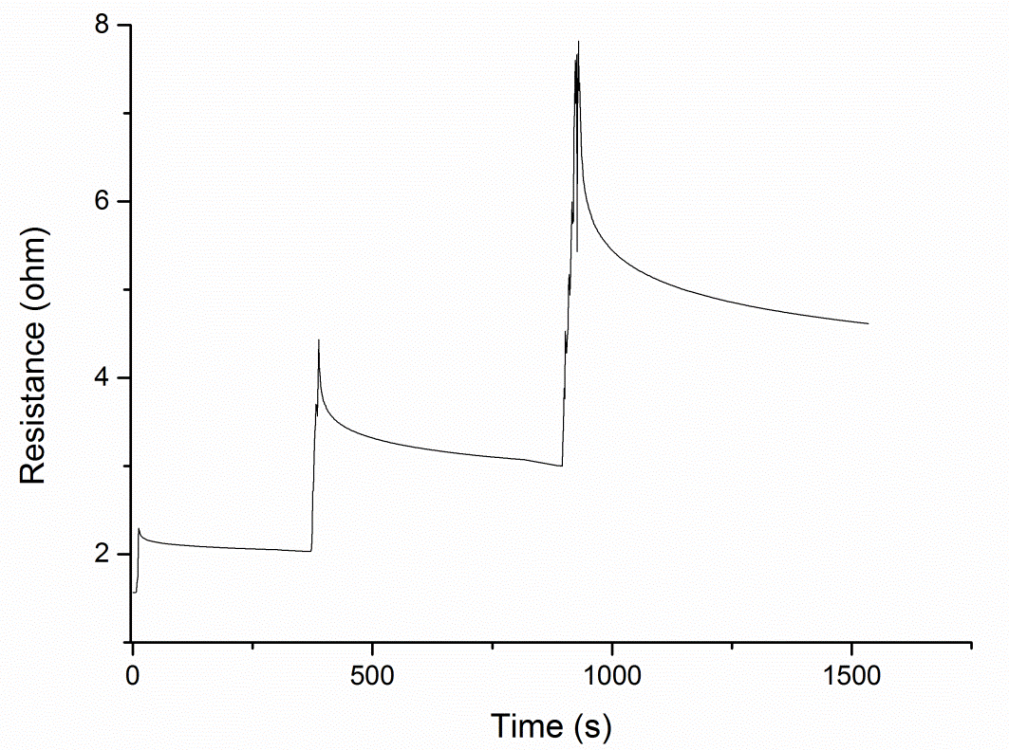

Fig.4. 25 Bending test of test vehicle cured at 50°C for 10min. (1,5,10 times in a row)

4.4 Conclusions

Firstly, DSC analysis was used to build the cure kinetic model capable of predicting the cure schedule at a given temperature for this typical ICA composed of epoxy-based binders and Ag filler particles. Two-parameter autocatalytic model (Sestak-Berggren model) was established as the most suitable description of the studied curing process. Based on the theoretical analysis and the practical curing process, the varying curing processes were set as: 10 minutes @ 50^{o}C, 6 minutes @ 100 ^{o}C, 10 minutes @ 100 ^{o}C, 6 minutes @ 150 ^{o}C.

Then, a series of test vehicles with ICA vias were cured follow the above curing processes. The electrical resistance of via decreases significantly when ICA conversion level is rising. In consideration of conductivity, process time and temperature, 100 ^{o}C and 6 minutes are the optimised curing temperature and time for the studied ICA.

Furthermore, DMA was used to investigate the effect of curing conditions on the mechanical properties of ICAs. Combining with the SEM images of the epoxy structure, it was identified that samples cured at 100 ^{o}C for 10 minutes possessed best mechanical properties.

Finally, the reliability of ICA vias was studied using thermal cycling test, damp heat test and bending test. Resistances of the vias were measured before testing and in real time during testing. During thermal tests, the vias cured at higher temperature had superior reliability compared to the vias cured at a lower temperature. Reliability of vias cured at 50 ^{o}C was extremely poor in bending test due to the low conversion. Besides the polymer binders' properties, the nature of Ag particles' distribution and connection were found to affect the vias resistance during bending.

Chapter 5 Multifunctional vias in flexible PCBs

5.1 Introduction

The investigation of multifunctional vertical interconnects in flexible substrates was presented in this chapter. Firstly, finite element (FE) model of ICA via was used to help better understanding of the electrical conduction mechanisms. Then a fistula-shape ICA via was developed. Its hollow nature provides the space for integrations of the optical or fluidic circuit. Two techniques were investigated and proved feasible to fabricate optoelectrical vias in flexible PCB.

5.2 Design and verify of fistula-shape via in FPCBs

5.2.1 Methods

5.2.1.1 FE model of fistula-shape ICA via

Based on the theory established above, fistula-shape vias was proposed to enable multifunction without compromising electrical conductivity. Firstly, models of fistula-shape ICA vias were built in COMSOL Multiphysics (COMSOL Inc.). Only conductive parts were built and meshed in order to save the computing time. Model geometry and mesh settings are listed in Table 5.1 and Table 5.2.

Table.5. 1 Dimensions of model

Parts	Dimensions（mm）			
	Length（L）	Width（W）	Height (H)	Diameter(D)
Copper track	1.00	1.00	0.035	—
Via	—	—	0.13	0.6
ICA cap	—	—	0.1	0.8

Table.5. 2 Mesh settings

Setting Name	Maximum element size	Minimum element size	Curvature factor	Maximum element growth rate	Predefined size
Value	0.02	2.0E-4	0.2	1.3	Extremely fine

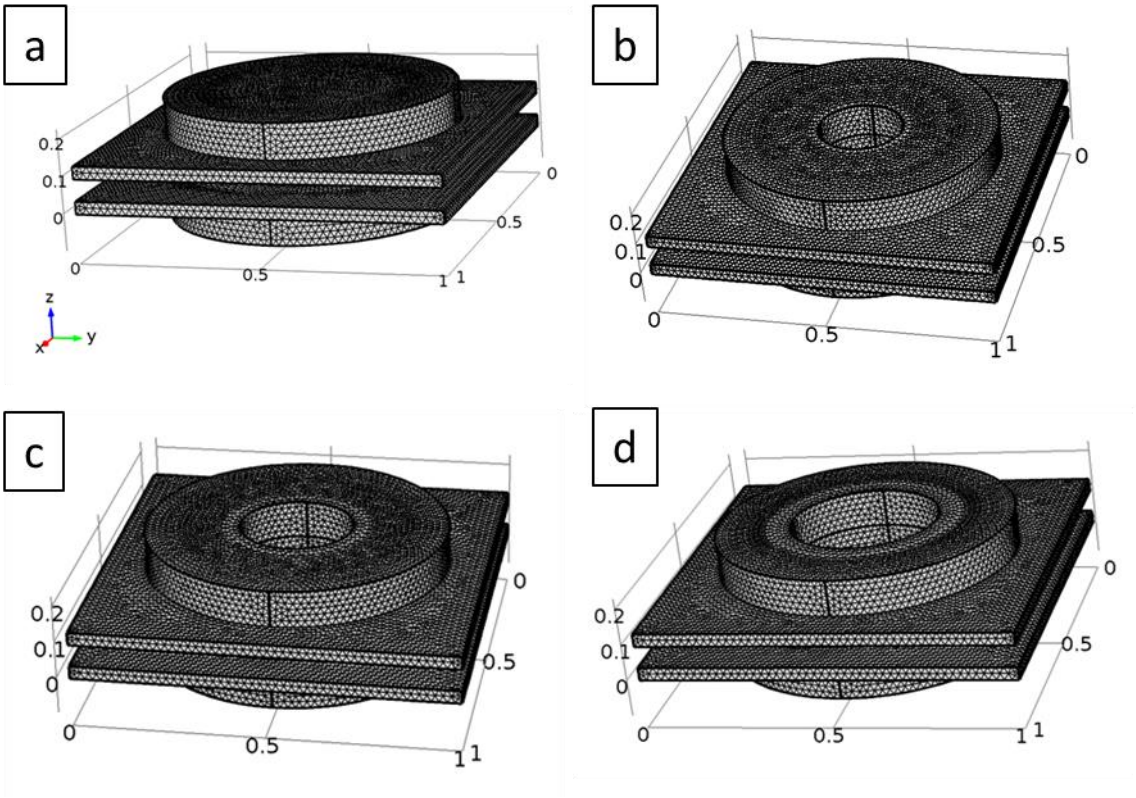

Fig.5. 1 Meshed model of ICA vias: a) solid, b) inner bore Φ0.25mm, c) inner bore Φ0.3mm, d) inner bore Φ0.4mm.

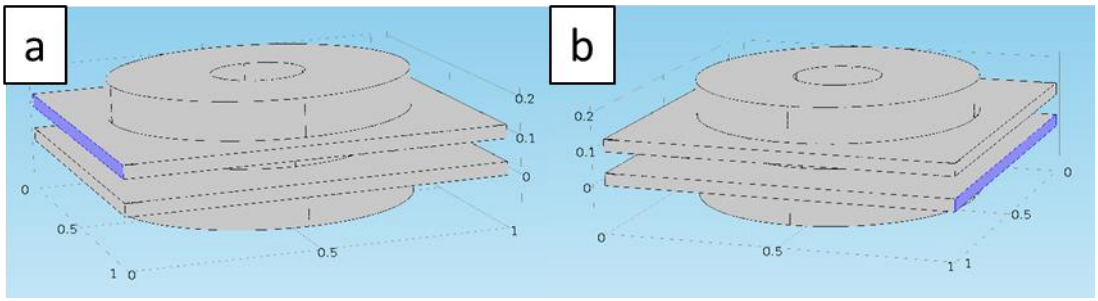

Fig.5. 2 a) Current input cross-section in top copper track, b) current output cross-section in bottom copper track

As shown in Fig.5. 2, 0.5 A current was added on top copper track. The electrical conductivity of ICA was set as 1e5 S/m, and the electrical conductivity of copper was set to be 5.998e7 S/m.

5.2.1.2 Manufacture and tests of fistula-shape via

Fistula-shape vias were made by drilling into the premade rivet-shape ICA vias. The size parameters were the same as the simulation models. All samples were mechanically drilled by Φ0.25 mm drill, and then the bores of some samples were enlarged by Φ0.3 mm and Φ0.4 mm drill. Resistances of vias were recorded before and after drilling. Temperature cycling test, damp heat test and bending test have been conducted to evaluate the reliability.

5.2.2 Results and discussion

5.2.2.1 Finite element analysis of electrical potential distribution and resistance

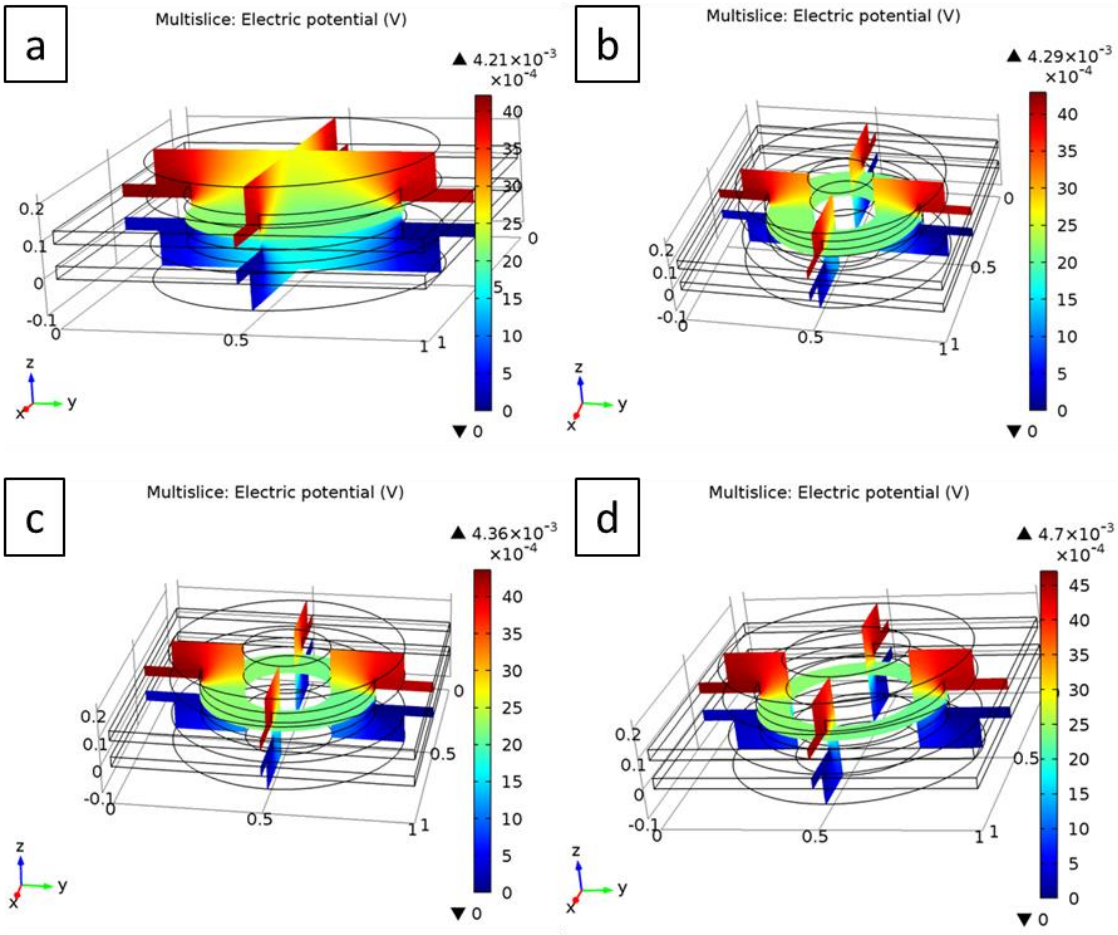

Fig.5. 3 The electric potential of ICA vias: a) solid, b) inner bore Φ0.25mm, c) inner bore Φ0.3mm, d) inner bore Φ0.4mm.

Electric potential is shown in multislice style (Fig.5. 3), it can be seen that the potential distribution didn't change much when small bore formed in the middle of the via.

The resistance of model was calculated by the software built-in equation and the via resistance versus bore size was plotted in Fig.5.4. The increase of slope, from 0.83 mΩ/mm^2 to 3.11 mΩ/mm^2, indicates that the impact on resistance grew larger when the bore size increased.

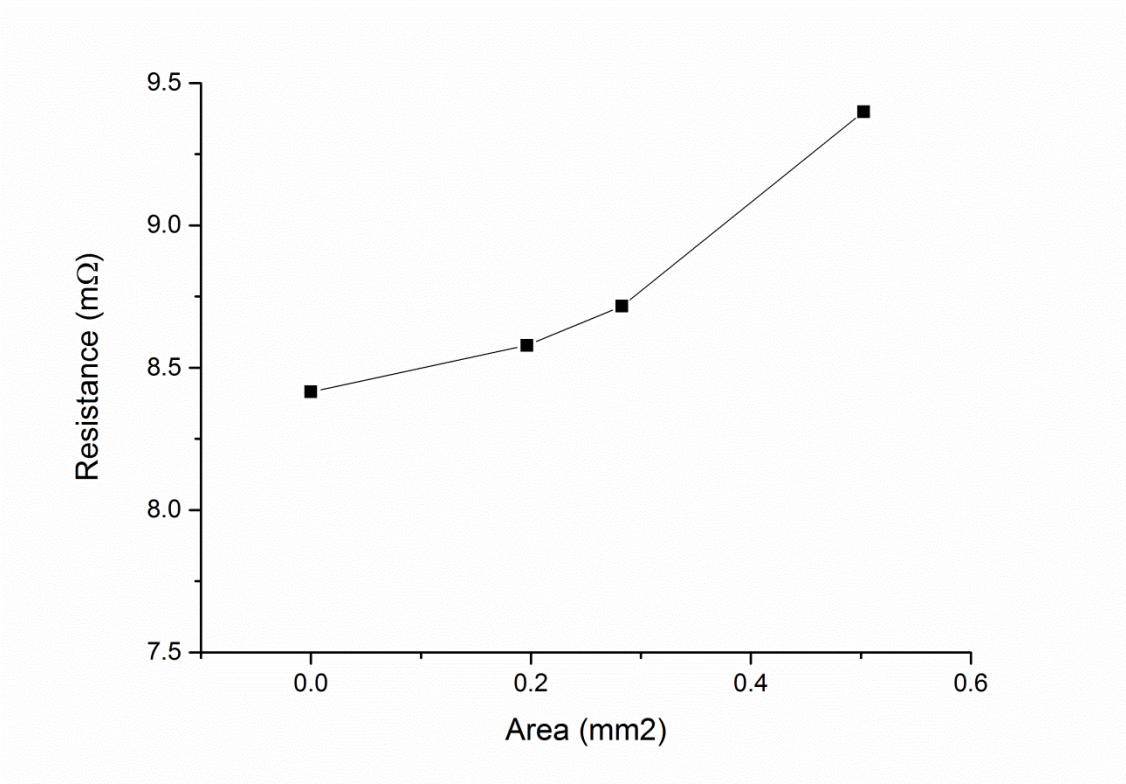

Fig.5. 4 Resistance versus bore opening area

5.2.2.2 Experimental results

Resistances of vias before and after drilling were listed in Table.5. 3. Considering the accuracy of the multimeter in four terminals mode is ± 8 mΩ, the formation of Φ0.25 mm and Φ0.3 mm bores in the centre solid vias had a neglectable influence on resistances. And notable increases appeared when the bore diameter increased to 0.4 mm. These experimental results fit the prediction in simulations. Moreover, finer alignment is required when drilling larger the bore. Like in Sample E (Fig5. 5), off-centre drilling broke one side of the ICA wall and significantly increased the via resistance.

Table.5. 3 Resistances of vias before and after drilling

Vias \ Bore diameter		0	0.25 mm	0.3 mm	0.4 mm
Sample A	Via 1&2	58 mΩ	57 mΩ	—	—
	Via 3&4	45 mΩ	43 mΩ	—	—
	Via 5&6	61 mΩ	60 mΩ	—	—
	Via 7&8	53 mΩ	54 mΩ	—	—
Sample B	Via 1&2	58 mΩ	58 mΩ	—	—
	Via 3&4	43 mΩ	42 mΩ	—	—
	Via 5&6	60 mΩ	61 mΩ	—	—
	Via 7&8	50 mΩ	50 mΩ	—	—
Sample C	Via 1&2	32 mΩ	32 mΩ	—	—
	Via 3&4	30 mΩ	28 mΩ	—	—
	Via 5&6	26 mΩ	24 mΩ	—	—
	Via 7&8	28 mΩ	41 mΩ	—	—
Sample D	Via 1&2	65 mΩ	66 mΩ	66 mΩ	76 mΩ
	Via 3&4	37 mΩ	37 mΩ	40 mΩ	49 mΩ
	Via 5&6	38 mΩ	37 mΩ	46 mΩ	56 mΩ
	Via 7&8	30 mΩ	30 mΩ	30 mΩ	33 mΩ
Sample E	Via 1&2	44 mΩ	45 mΩ	49 mΩ	67 mΩ
	Via 3&4	38 mΩ	38 mΩ	40 mΩ	45 mΩ
	Via 5&6	36 mΩ	39 mΩ	40 mΩ	43 mΩ
	Via 7&8	39 mΩ	39 mΩ	42 mΩ	58 mΩ
Sample F	Via 1&2	18 mΩ	15 mΩ	17 mΩ	22 mΩ
	Via 3&4	26 mΩ	25 mΩ	25 mΩ	32 mΩ
	Via 5&6	26 mΩ	26 mΩ	26 mΩ	33 mΩ
	Via 7&8	41 mΩ	38 mΩ	38 mΩ	49 mΩ

Fig.5. 5 Cross-section of Via 1 in Sample E (bore diameter 0.4mm)

Sample A went through damp heat test together with other solid via samples. As shown in Fig.5. 6, fistula-shape vias exhibited the same behaviour as the solid vias in damp heat test. No deterioration was observed.

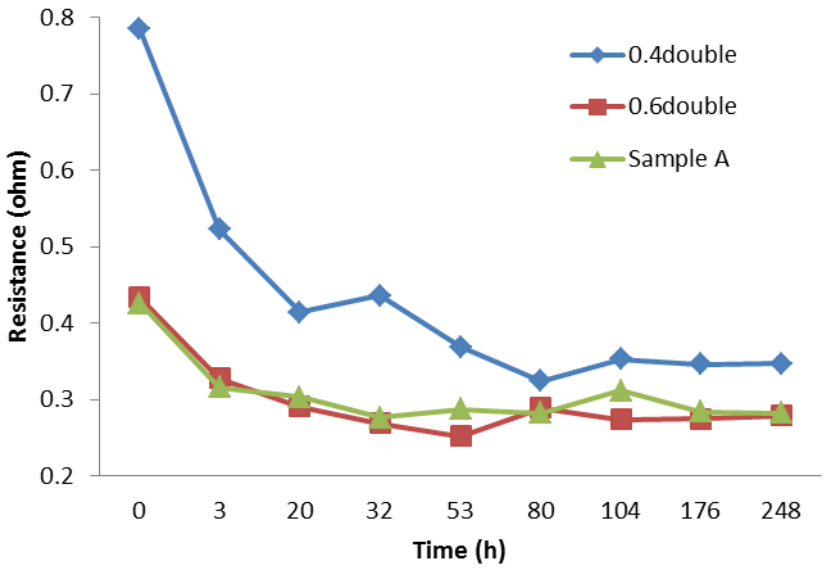

Fig.5. 6 Resistance evolution of test vehicle solid and fistula double-caps vias as a function of time at 85 °C/85% RH

Temperature cycling test was conducted on another two samples with Φ0.25 mm (Sample B) and Φ0.4mm (Sample D) bores. It can be concluded from Fig.5. 7, the performance of fistula-shape vias was the same as solid vias under cyclic thermal load. The vias with Φ0.4mm bores were affected less by post-cure effect due to there was less ICA in the vias.

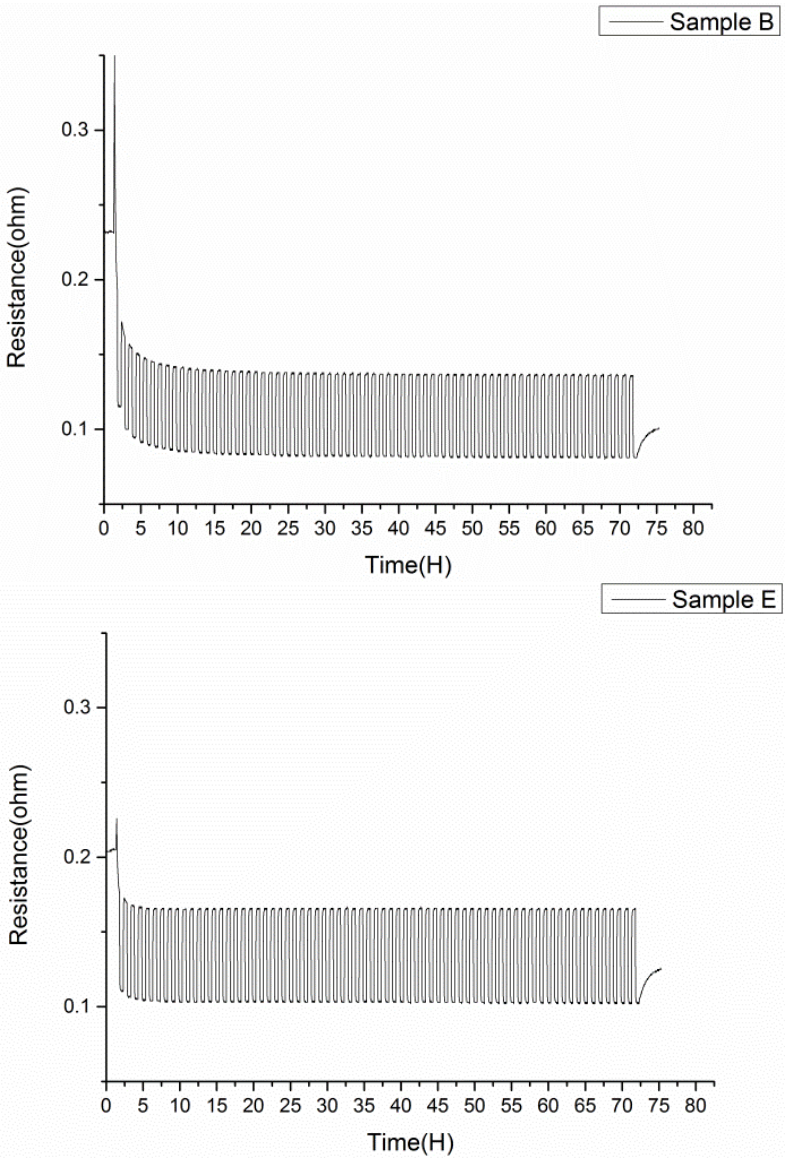

Fig.5. 7 Evolution of test vehicle resistance as a function of time exposed to temperatures cycles alternating between -40 °C and 125 °C.

Bending experiments were performed on the rest two samples, C and F, by flexing the samples around Φ 5 mm cylinder. The total resistance of vias with Φ 0.25mm bores increased 103.45% after 106 times bending, which is similar to solid Φ 0.6mm-caps vias (103.5%). While the total resistance of vias with Φ 0.4mm bores increased more rapidly, it increased 105.85% after 56 times bending.

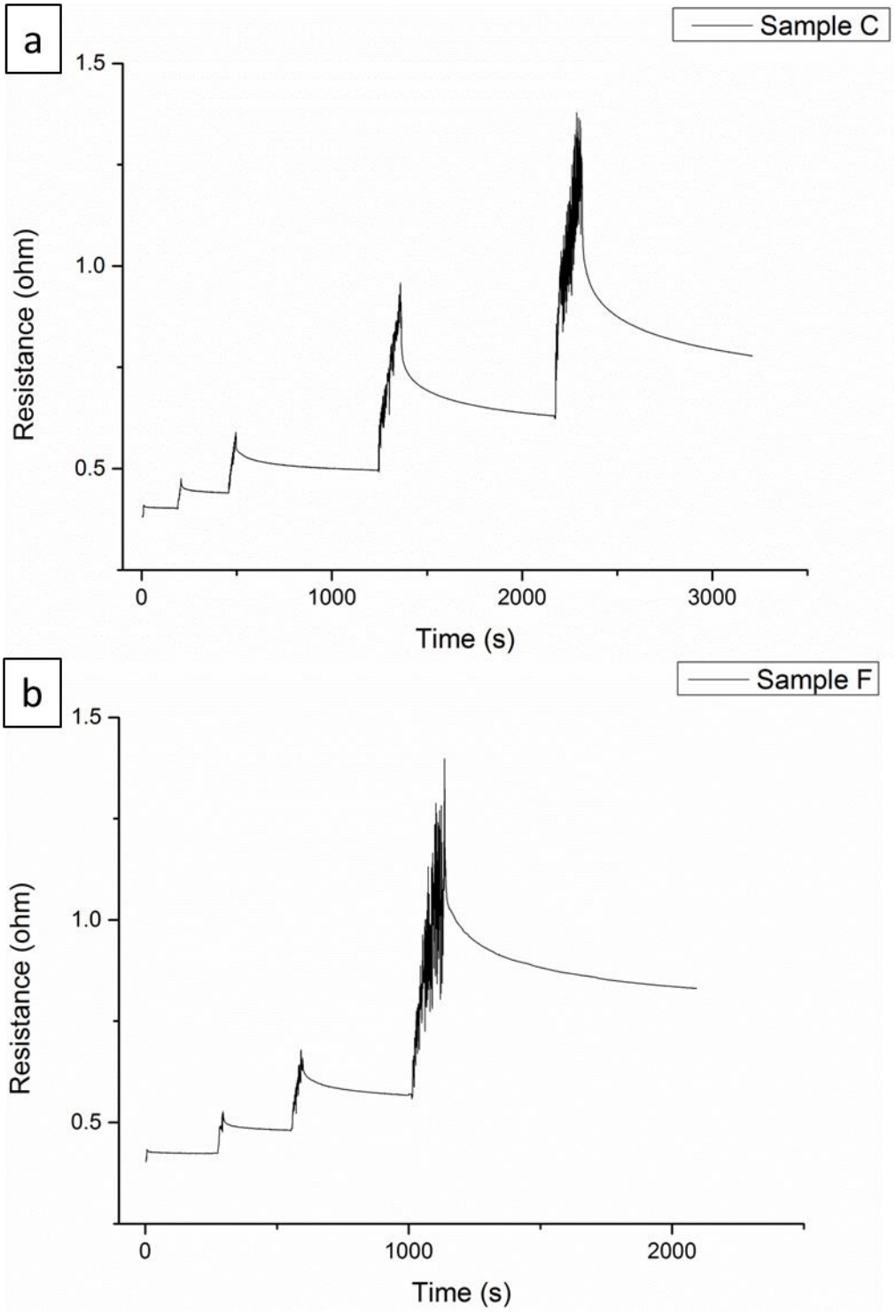

Fig.5. 8 Real-time resistance recording of, a) Sample C: Φ 0.25 mm, b) Sample F: Φ 0.4mm.

5.3 Investigation on optoelectrical vias in FPCBs

5.3.1 Optical interconnection formed by PMMA via fill

Opto-electrical vias can be achieved by forming optical vias within the fistula-shape ICA vias. In this research, optical waveguides and vias were formed in one step by depositing polymethyl methacrylate (PMMA) solution, using a motor assisted micro-syringe extrusion deposition system (MAM-II, Fochif, China).

In order to form a thin and uniform waveguide, PMMA solution should be high concentration and homogeneously dissolved. The greater the viscosity of solution the higher aspect ratio can be achieved [132]. Meanwhile, the viscosity is limited by the aperture of deposition needle. In this experiment, the PMMA solution should be able to pass through Φ0.2mm needle by syringe pushing. PMMA is soluble in strong polar solvents. Therefore Dimethyl Formamide (DMF) and Tetrahydrofuran (THF) were chosen. Due to the low boiling points of DMF (149-156 ^{o}C) and THF (67 ^{o}C), we can firstly prepare a dilute solution of uniformly dissolved PMMA and then adjust the viscosity by volatilizing the THF. Specific preparation steps:

1. Put 20 g dry PMMA grains into 200 ml mixture of THF and DMF (volume ratio 4: 1).
2. Stirred by a magnetic mixer for 120 minutes and ultrasonic dispersion for 30minutes.
3. Allowed to stand for solvent volatilization.

The higher the boiling point of the solvent, the higher the temperature required for volatilization and the slower the evaporation speed. During the heat treatment, a dense PMMA film will appear rapidly on the surface of waveguide under high temperature, which hinders the solvent from evaporating. Small bubbles formed inside the waveguide by remained solvent will cause scattering loss. Therefore, after deposition, the test vehicles were left at room temperature (29 ^{o}C) for 1 hour. Then test vehicles were moved into the oven, and the heating profile was set as 20 ^{o}C/hour to 70 ^{o}C, then 60 ^{o}C/hour to 160 ^{o}C and kept for 10 minutes. The micro bores and bubbles were significantly reduced by slow and low-temperature evaporation.

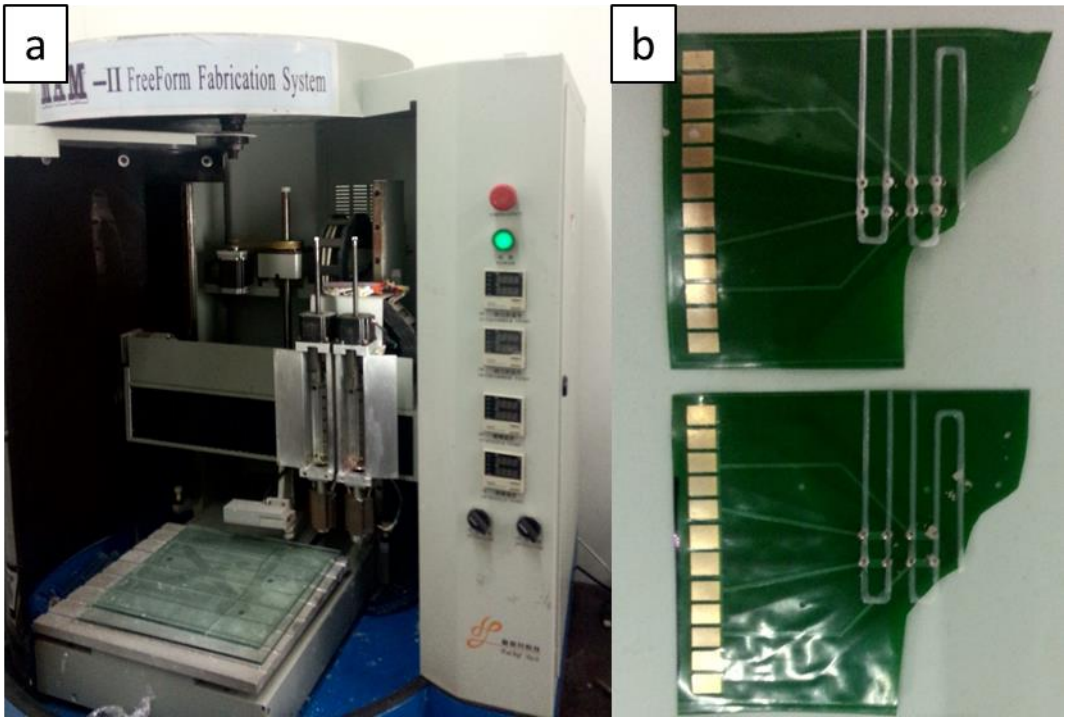

Fig.5. 9 a) MAM-II FreeForm Fabrication System

b) PMMA traces printed on flexible PCB with fistula-shape ICA vias

Fig.5. 10 Optical microscope image of an optoelectrical via

As shown in Fig.5.9b and Fig.5.10, the optical waveguides were successfully deposited on the flexible PCB, and the vias were fully filled. Feasibility of adding optical function by additive manufacturing was proved. However, the PMMA track delaminated from flexible PCB once occurred to bending. Future works on surface treatment are needed to solve adhesion problem.

5.3.2 Optical interconnection formed by PMMA fibre

A cheap and quick method to realise both optical and electrical vertical connection was proposed that the ready-made optical fibre can be used as a waveguide. As shown in Fig.5.11, there are several ways to integrate the optical fibre into a via hole.

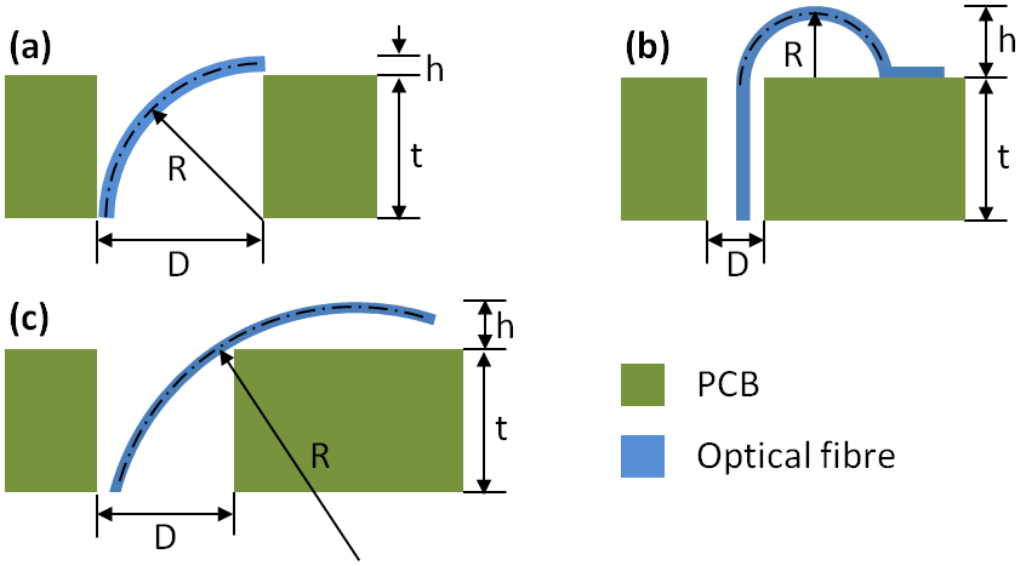

Fig.5. 11 The schematic diagram of three different optical fibre integration arrangements. D: the diameter of via hole, t: the thickness of PCB, R: Bending radius of the optical fibre midline, ϕ: the diameter of the optical fibre, h: the stand-out height

By Inserting a quarter circle of the fibre in the via hole (Fig.5. 11.a), the fibre can be attached to the top surface of the layer right after it jumping out the via hole. The stand-out height h= ϕ, the diameter of via hole D_{min}= 0.5ϕ+R. This design can minimise the stand-out height which is ideal for layer stacking but requires a large via hole. Another design (Fig.5. 11.b) is putting the fibre vertically through the via hole and leaving the bending curve over the top surface of the layer. The stand-out height h= 0.5ϕ+R, the diameter of via hole D_{min}= ϕ. This design can be use on the top layer of the PCB without any other layers or components stacking on.

To miniaturise the device, the designs mentioned above would limit the bending radius of the fibre to a small value. Therefore, the third design (Fig.5. 11.c) is proposed. It is a trade-off between the diameter of via hole and stand-out height. By adjusting the position of the fibre, a reasonable size of D and h can be obtained together with a much larger bending radius.

5.3.2.1 Preliminary experiments of optical fibre bending loss

The entire testing system (Fig.5. 12) consists of three parts: a light emitting diode (LED) with the light source driving part, optical fibre sample and data acquisition part. A high-performance green LED (HLMP-1540, Hewlett Packard Ltd.) was selected, and the drive current was controlled by adjusting a variable resistor. The peak wavelength of the LED is 565nm, and the bulb diameter is 3mm. A Silicon Photodiode (PD) for the Visible Spectral Range (BPW 21, OSRAM Opto Semiconductors Ltd) was employed to detect the output light from the optical fibre. The photovoltages were obtained from the readings of a directly connected voltage meter. The optical fibre was bent into a curvature by two fixtures, one end of the fibre is attached to the LED and the other end is attached to the PD. The LED, PD and optical fibre were fixed on a stage (Fig.3) and put in a black box to reduce the influence of environmental light during the test.

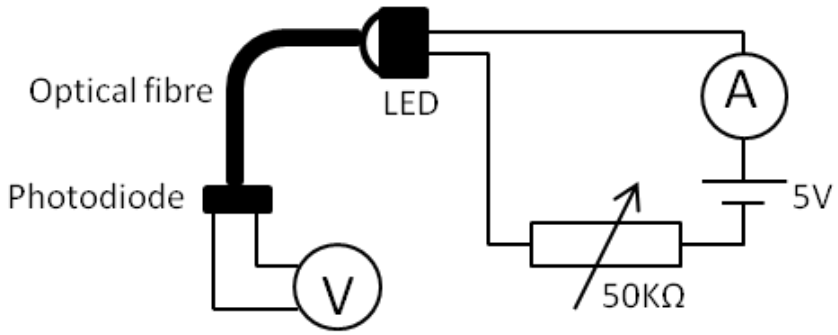

Fig.5. 12 The schematic diagram of optical fibre loss testing

A PMMA fibre was cut 115 mm long. Then its two ends were polished to be flat, and the final length is 114.5 mm. The fibre was manufactured with a curvature; the curve radius is 171 mm without any external force. The diameter of the fibre is 3 mm. The PMMA core was covered with two layers of PVC insulating tape, which served as a cladding layer.

The environment temperature was 20 ^{o}C. The LED drive current started from 0.4 mA, and the current increment is 0.2 mA for each step between 0.4mA and 3mA. From 3 mA to 4.5 mA, the increment is 0.5 mA. Firstly, the LED was placed directly to the photodiode to get a set of references. Then the fibre was placed between the LED and photodiode with different curvature to measure the output changes under the same input variations (Fig.5. 13) :

Model A: The fibre was bent to be straight.

Model B: The fibre was held with its original shape (Fig.5.28. a).

Model C: The fibre was bent to a curve of 58mm radius (Fig. 5.28.b)

Model D: The fibre was bent to a curve of 35mm radius (Fig. 5.28.c)

Model E: The fibre was bent to a curve of 26.6mm radius (Fig. 5.28.d)

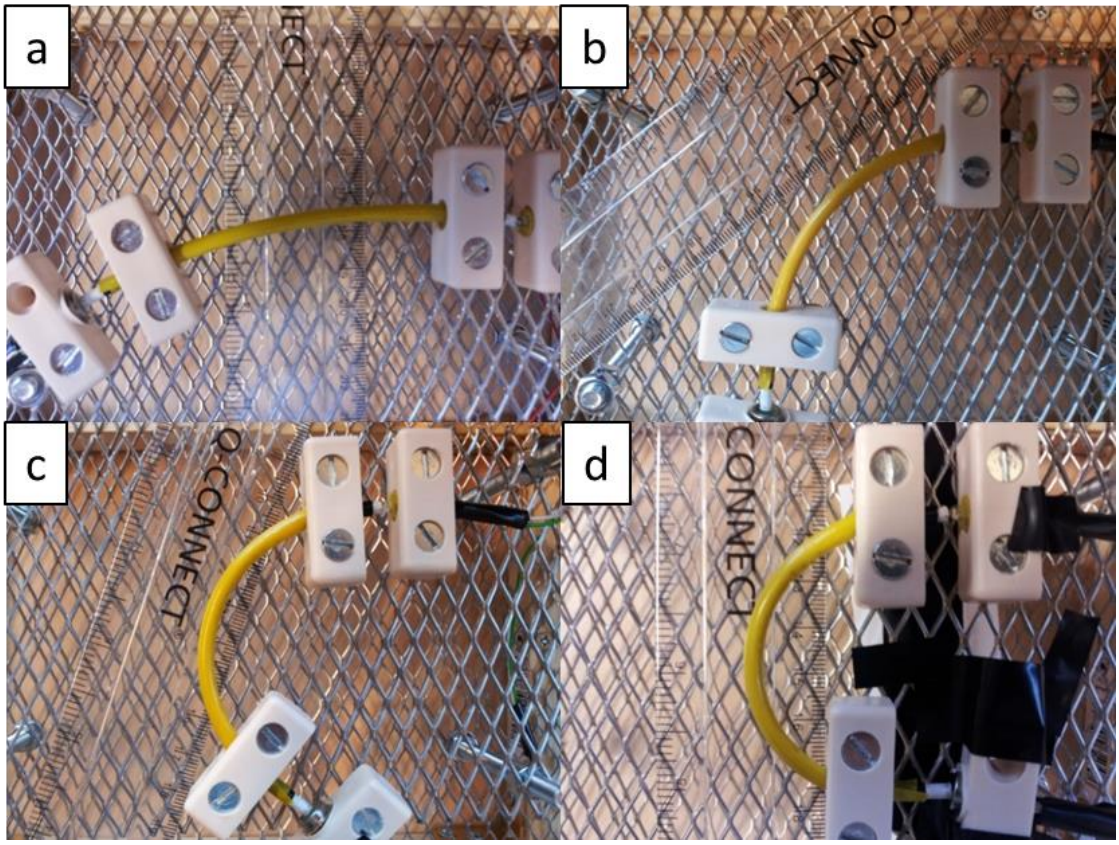

Fig.5. 13 Photos of different bending setups for optical fibre: (a) bending radius: 171mm, bending angle: 39°, (b) bending radius: 58mm, bending angle: 104.5°, (c) bending radius: 35mm, bending angle: 164.5°, (d) bending radius: 26.6mm, bending angle: 185°

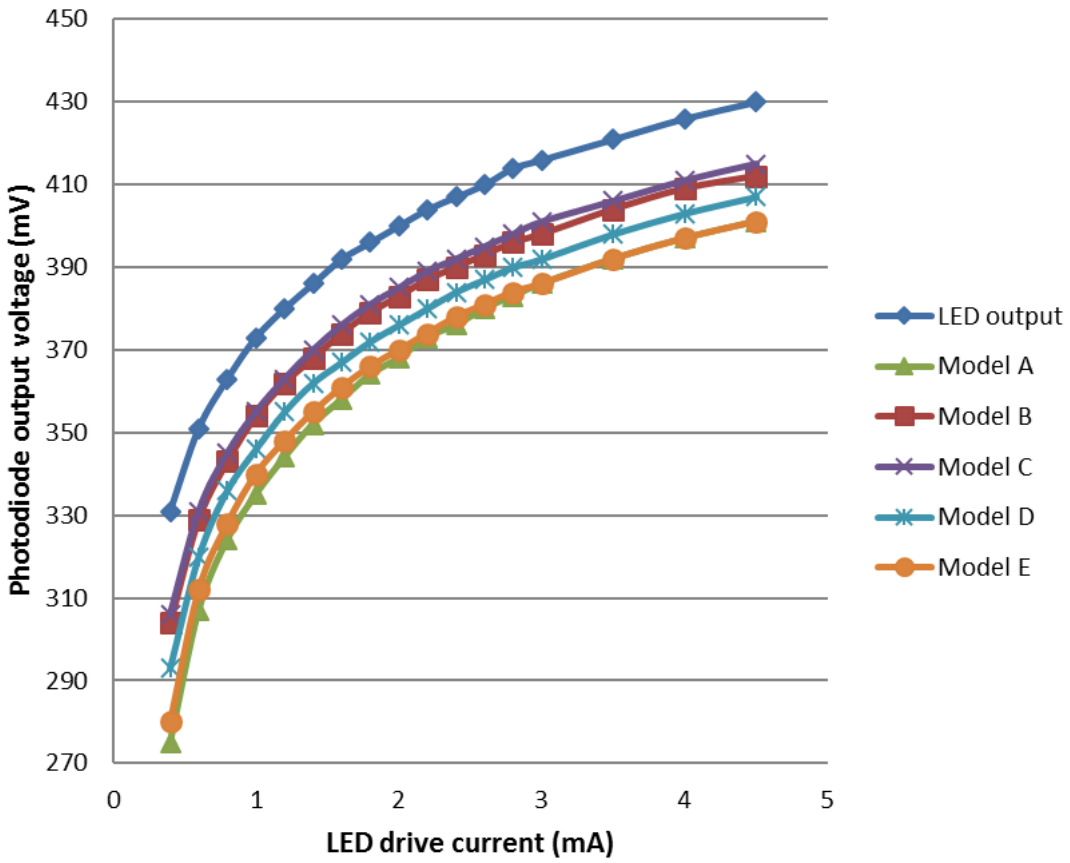

Fig.5. 14 The photovoltages of different models under different LED drive current.

Photodiode output voltage is proportional to the light power that photodiode absorbed, so it can be represented as the output power of the fibre. Similarly, the input power is represented by the photodiode output voltage when LED illuminated the photodiode directly. It can be seen from Fig.5.15.a; the Model C had a higher output. The Model B was similar to the Model C, which suggests the bending loss would be stable in a certain bending radius range, like 171mm-58mm in this case. When the bending radius reduced to 35mm, the output power decreased significantly. And the output power decreased further when the bending radius reduced to 26.6mm. Under the same experiment system and input conditions, the decrease of output power means the increase of bending loss. So it is proven that the smaller the bending radius, the bigger the bending loss. There was an exception that the straight fibre has a very big bending loss, this may because the fibre is made with a curvature. The microbending and inhomogeneities of the fibre increased when straightening the fibre. Thus material quality is important and should be considered in the first place in installation.

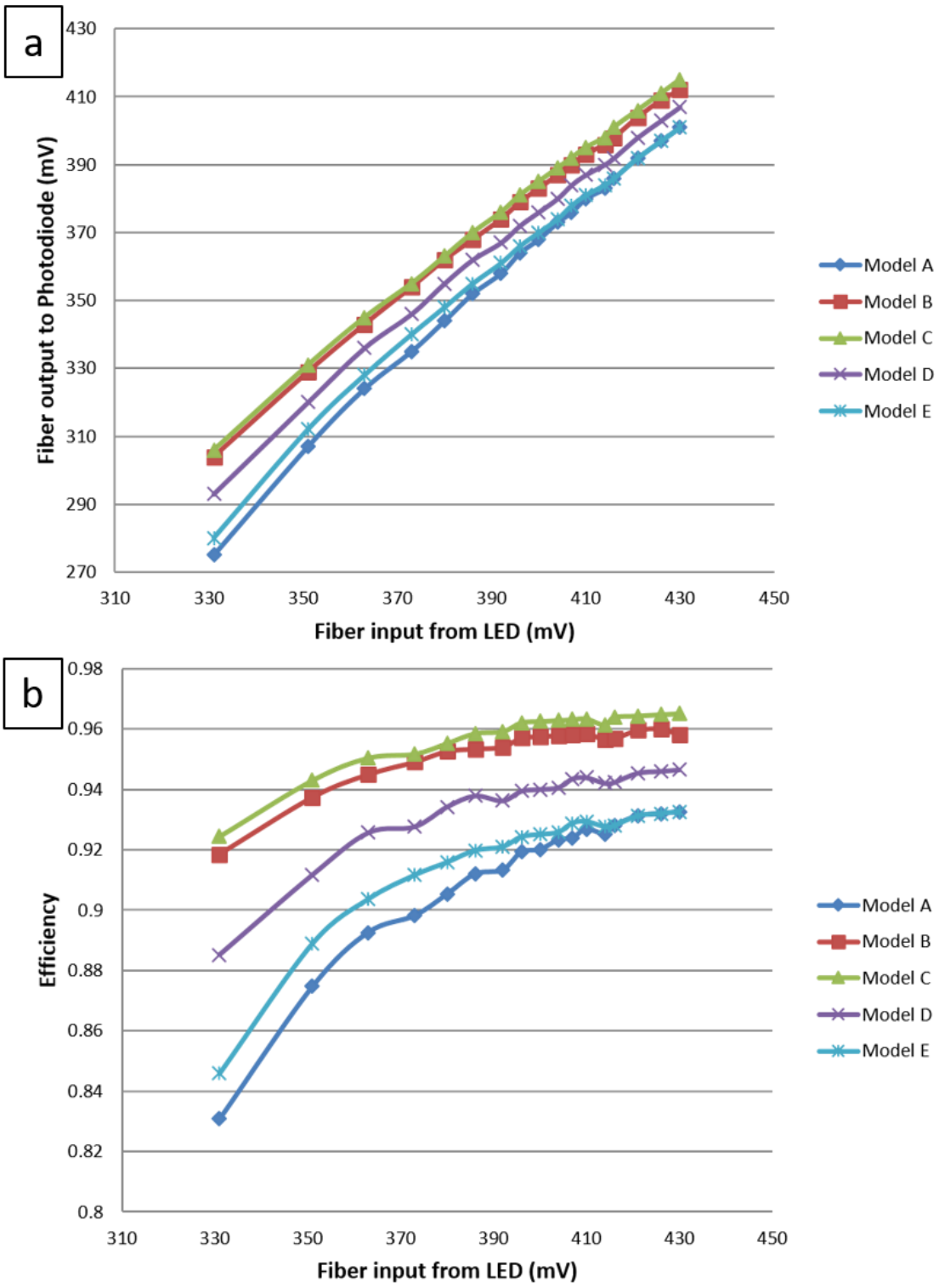

Fig.5. 15 a) Fibre output versus input, b) the transmission efficiency of different models under different input power

The transmission efficiency of tested fibres was defined as the ratio of output power (fibre-output voltage reading) to input power (LED-output voltage reading). As shown in Fig.5.15.b, the efficiency was quite low at the beginning, and then increased with the rise of LED output,

and remained relatively stable after LED output voltage reached 396 mV. This indicates that this optical fibre performs poorly under low light intensity and may not be suitable for working in low-light applications, such as sensing low-light-emitting samples.

These results also agree with the normal fibre installation recommendation [84], which suggest the bending radius should not be less than 15 times of the cable diameter to maintain the performance. In this case, the cable diameter was similar to the core diameter. Table 5.4 shows the ratio of bending radius to core diameter, the bending radii of Model B and C are more than 15 times of the core diameter, while the Model D and E are less.

Table.5. 4 the ratio of bending radius to core diameter

Model	B	C	D	E
Ratio	57	19.3	11.7	8.9

5.3.2.2 Integration with flexible PCB

High-performance plastic optical fibre CK-10 (MITSUBISHI RAYON CO., LTD) was used in this experiment. The diameter of PMMA core is 240 μm, and the cladding layer is 5 μm thick fluorinated polymer.

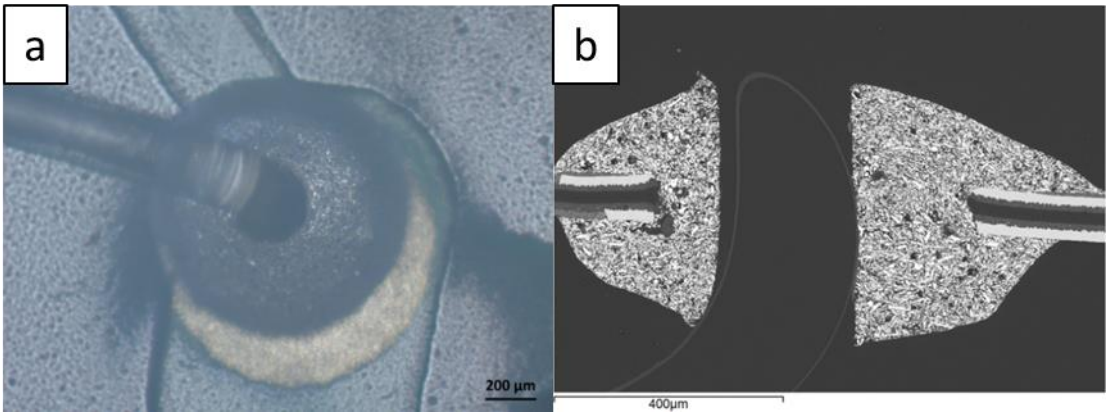

Fig.5. 16 a) Top view of an optoelectrical via, b) cross-section of an optoelectrical via.

Three 280mm long Fibres were cut and inserted through ICA via holes (Fig.5.16), and their ends were polished and mounted in connectors. (Fig.5.17) A visible Laser diode (2008368, LASER COMPONENTS) with a typical wavelength of 655nm was selected as the light source. The power supply to the laser diode was regulated and adapted by an external resistor in Laser

driver (2011660, LASER COMPONENTS). Silicon Photodiode (S5973, HAMAMATSU) is employed to detect the output light from the optical fibre. The input power of fibre was set constant: 325 mV. The operating environment temperature was at 18 ^{o}C. The photovoltages were obtained from the readings of a directly connected multimeter and recorded in Table 5.5.

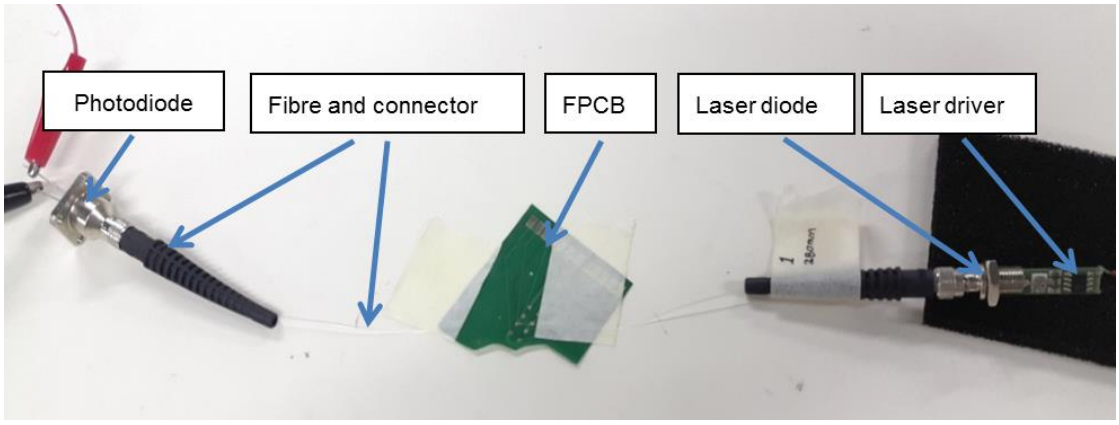

Fig.5. 17 Test system for optoelectrical via integrated in flexible PCB (FPCB)

Table.5. 5 Fibre output in photovoltages (mV)

		Test vehicle A	Test vehicle B	Test vehicle C
Before Bending	Unconstrained	274.4	266.4	267.9
	Integrated	—	254.3	256.7
Bending	5 times	274.3	253.6	230.9
	10 times	274.5	252.4	229.5
	20 times	274.4	251.5	236.0
	50 times	274.0	249.6	230.0
After Bending		274.4	266.5	256.7

The fibre in test vehicle A was unconstrained and bent to Φ40 mm cylinder. The fibres in test vehicle B and C were fixed on FPCB, and its minimum bending radius was 0.7 mm. Test vehicle B was flexed to the same cylinder as test vehicle A. While the test vehicle C was flexed

to Φ5 mm cylinder. It can be concluded that the optical loss increment is around 0.2 dB after integrating PMMA fibre as an optical via. This kind of optical via is sensitive to dynamic bending because the inherent curve of the fibre is more easily deformed. That also explains why test vehicle A remained stable while test vehicle B changed slightly during Φ40 mm cylinder bending test. The changes in fibre output increased when bending radius reduced to Φ5 mm.

5.4 Conclusions

Finite element model of ICA via was used to help better understanding of the electrical conduction mechanisms. The simulations suggested that electrical current in ICA vias would exhibit similar characteristics like in homogeneous conductive material and most current flow through the outer tubular part of the ICA fill.

Based on theoretical equation and simulation model, the fistula-shape ICA via was developed. Its hollow nature provides the space for integrations of the optical or fluidic circuit. Resistance measurement and reliability tests proved that carefully designed and manufactured small bores in vias will not comprise the performance. In this study, the recommendation of bore diameter in Φ0.6 mm rivet-shaped via is 0.3 mm max.

This research has demonstrated the feasibility of multifunctional vertical interconnects in flexible substrates. Test vehicles with optoelectrical vias were made through two different approaches to prove the concept.

Direct writing, an additive manufacture method, was used to fill the via hole and forming the planar waveguide on the substrate in one process. It is a quick and flexible way to form optical vertical interconnects, but the quality of the waveguide highly depends on the capability of manufacturing facilities.

On the other hand, plastic optical fibre integration required no high-end equipment. Ready-made fibres are easy to access. In this study, Φ0.25 mm PMMA fibre (core diameter 0.24 mm) was integrated through fistula-shape ICA vias. After installation, the minimum bending radius of the fibre is 0.7 mm, and the optical loss increment is around 0.2 dB which is acceptable. The downside of this method is that the curved fibre occupied a lot of space, thus increase the height of the whole package. This structure was also sensitive to bending.

Chapter 6 Validation of ICA interconnections through PPG probe manufacturing

6.1 Introduction

As indicated by World Health Organization (WHO), continuous monitoring is one of the effective means to not only assess physiological status that is related to these diseases but also provide indications of disease progression and make it easier to manage daily based medicine and therapy [133, 134]. A simple and cost-effective optical technique, photoplethysmography (PPG), is often employed non-invasively to monitor blood volume changes for physiological assessment. The PPG system mainly consists two parts: light sources for the illumination of the skin tissue, and photosensors for the measurement of light intensity variations [35, 37]. A novel reflection-mode photoplethysmography (rPPG) probe was developed and trial-manufactured in the project. This probe can be integrated into POCT device for in-vivo and non-invasive physiological assessment.

The light-weight flexible polymer film was used to make the PPG patch probe user-comfortable and well fitting. The polymer substrate and key parts of the probe (surface-mount light emitting diodes (LEDs) and photodiodes) were all heat sensitive. Thus an ICA-based low-temperature manufacture process was established to realise the probe design referring to previous research outcome. The interconnections were validated through functional tests and “proof of concept” using. In prototype Type One, the photodiode and LEDs were mounted on a flexible circuit to achieve sensitivity, stability, and user comfort. Based on the success of the first prototype, double-sided flexible circuits and ICA vias were utilised to improve the performance in probe Type Two.

6.2 Methods and experimental setup

6.2.1 Substrate materials selection

Compared to conventional Polyimide (PI) film, Polyethylene Terephthalate (PET) film and Polyethylene Naphthalate (PEN) film are cheaper but less thermal stable. The warpage and shrinkage of the FPCB would cause the dislocation of components that affects the accuracy of the photonic system and induce stress that affects reliability. Therefore, the thermal dimension stability was set as a selection criterion. The dimension shrinkage after manufacture processes should be less than 1% and the smaller, the better. There were two candidates:

a) Polyethylene Terephthalate (PET) film with electrodeposited copper (GTS 5560),

b) Polyethylene Naphthalate (PEN) film with electrodeposited copper (GTS 5670).

The thicknesses of the film and copper are 125 μm and 35 μm, respectively.

Two laminates were made into specimens (Fig.6.1) by selectively removing a photoresist coating and etching the unwanted copper. A heating test was carried on the specimens to investigate the thermal dimensional stability of the materials. Due to the shape of the board and copper pattern, the strains mainly concentrated in one axial direction. Dimension change was measured by the distance change from point A to point B. The original distance between A and B is 43.5 mm.

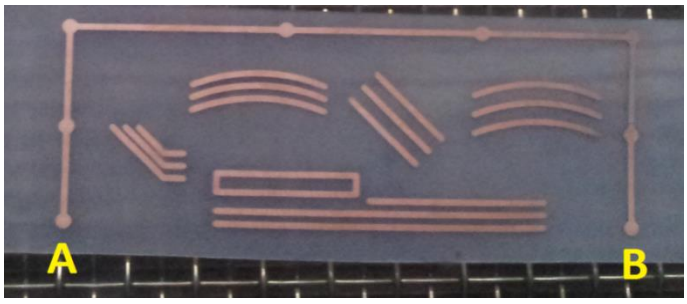

Fig.6. 1 The photo of a test specimen

In the heating test, the specimens were placed unconstrained in an oven. The heating profile was divided into three stages. The first stage was the common ICA curing condition, and the temperature was elevated in the followed two stages to test the capability of alloy soldering (Fig.6.2).

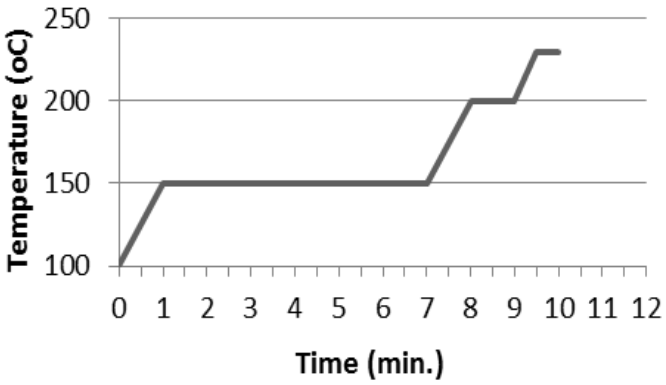

Fig.6. 2 Heating profile for Thermal dimension stability test, stage 1: 0~7 mins, stage 2: 7~9 mins, stage 3: 9 mins~

The heating test repeated three times. In the first test, the specimens were taken out for dimension measurement right after stage 1 and then put back. Same operations were done right after stage 2 in the second test, and right after stage 3 in the third test.

6.2.2 Architecture design

Probe Type One was a basic version to explore the feasibility of the design and manufacture. The copper track was made 2 mm wide to secure the conductivity and components alignment. The photodiode (PD) is OSRAM, BPW 34 S and light-emitting diodes (LEDs) are in SMD0603 type package. The probe Type Two is based on Type One, a larger PD (HAMAMATSU, S10357-01) is used to increase sensitivity. The number of LEDs is also doubled and located symmetrically to improve the performance. In order to accommodate more components in a smaller patch, the copper track width was reduced to 0.5 mm and a double-side circuit design was adopted. Electrical vias were used to connect the two circuit layers.

PCB design software: DesignSpark PCB 5.0 was used to design the PCB architecture and output the Gerber file for FPCB fabrication. First of all, the centre to centre distance between LED and PD is fixed to ensure the probe's function. When locating the components, the actual size of the component and its contact pad size are also taken into consideration, thus leaving enough space for copper traces. After components placement, all the components are connected in right order, followed by wires adjustment to achieve optimised electrical performance. There are several tips for wiring arrangement [135, 136]:

1. The signal traces should be as short and direct as possible.

2. Avoiding sharp angle turns. Using round turns or two 45-degree bends instead.
3. Position polarised parts (i.e. diodes, and electrolytic caps) with the positive leads all having the same orientation.
4. Avoiding parallel traces to reduce parasitic current. It's better to have vertical traces on one side and horizontal traces on the other for double side circuit.

6.2.3 Manufacture process

6.2.3.1 Probe Type One

a. The FPCB was fixed on a rigid FR-4 board by the tape

c. Isotropic conductive adhesive (ICA) paste was deposited on connection pads.

b. A flip-chip bonding machine was employed in components mounting (Fig.6.3). The components are picked and placed pneumatically with the optical microscope (Leica WILD M3Z) aided component positioning.

Fig.6. 3 Flip-chip bonding machine.

d. The FPCB was placed into the oven for adhesive curing. A thermal couple was put on the PCB to monitor the actual temperature at bonding area. The curing oven is the JEM-310 Batch Reflow System (Fig.6.4) which is programmable and auto temperature control. The heating profile was optimised with the condition of maintaining the ICA at 100 ^{o}C for 10 minutes.

Fig.6. 4 JEM-310 Batch Reflow System

e. After the bonding of photodiode, LEDs and I/O wires, a foam ring was mounted around the photodiode to isolate the direct light from LEDs; then the LEDs were covered by diffusion film. Finally, the whole probe was covered by a thick layer of foam.

6.2.3.2 Probe Type Two

In addition to via hole formation and filling, the manufacturing procedure of probe Type Two was the same as the Type one. After forming the circuit pattern, Φ 0.7 mm vias were mechanically drilled through the board and filled with ICA. After curing, the top circuit and bottom circuit were vertically connected by these ICA filled vias (Path B in Fig.6.5).

The stencil was made from 0.35 mm plastic board by mechanically drilling. When filling the vias from one side, some ECA paste would leave on the holder board and form voids at the other side. To solve this problem, two identical stencils were attached on both sides of the PCB (Fig.6.6), so the vias could be fully filled by squeezing the adhesive with a blade manually from only one side.

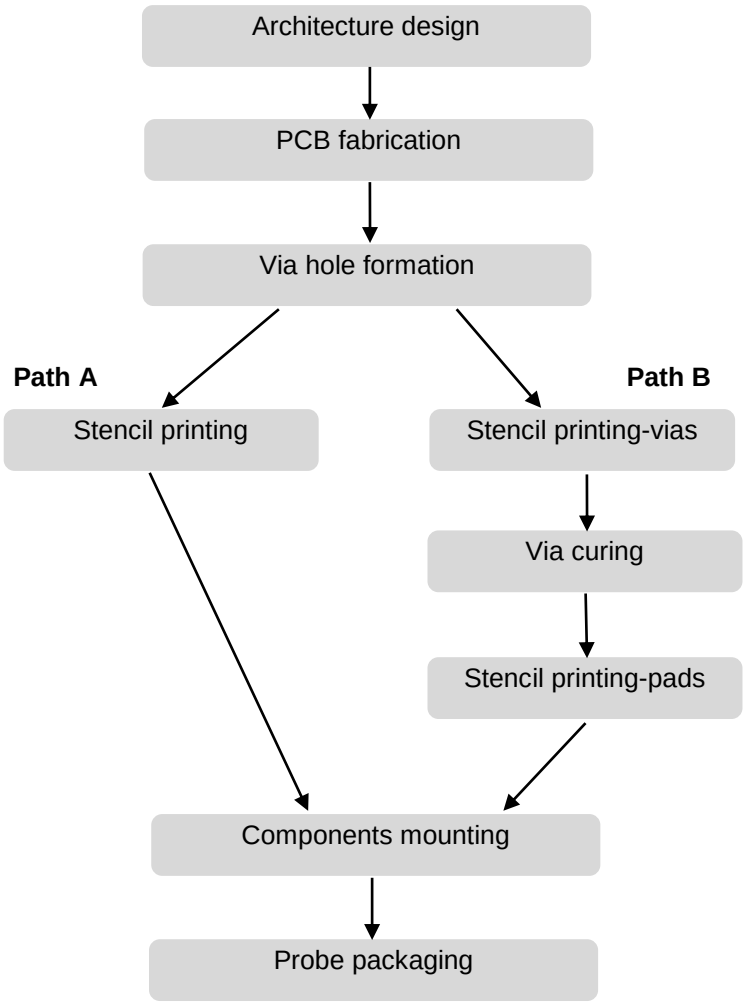

Fig.6. 5 Manufacturing procedures of rPPG patch probe Type Two

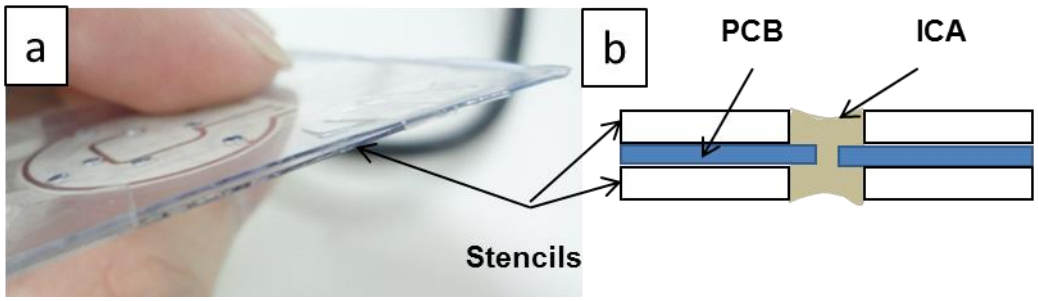

Fig.6. 6 a) Stencils arrangement: the two stencils were fixed by adhesive tape after alignment, b) a sketch of cross-sectional stencil printing setup

A simplified manufacturing process (Path A in Fig.6.5) was developed based on double stencils. The schematic process flow is presented in Fig.6.7. The principle was relatively simple: the stencils and FPCB are aligned by alignment pins (1). The ICA is deposited on the pads and in the vias by blade squeezing from the top (2). Removing the top stencil (3) and mounting components (4). Removing bottom stencil and curing (5).

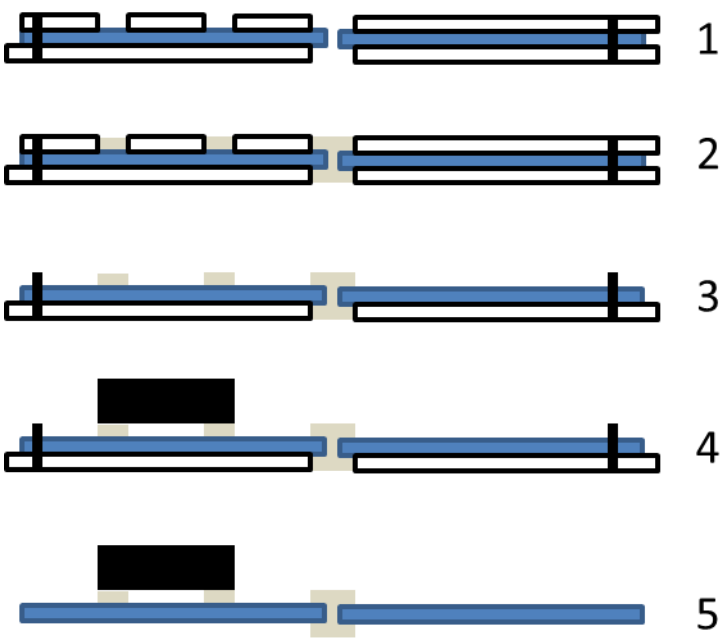

Fig.6. 7 Schematic illustration of Path A

6.2.4 Functional test setup

6.2.4.1 Cylindrical Bending Test

A simple bending test was carried out after the rPPG patch probe was fully manufactured and packaged. The probe was bent over a 25 mm radius cylinder and recovered in the frequency of 20 cycles per minute in a room environment (Fig.6.8). The forward voltage drop was measured by the diode function on a multimeter (10XL, WAVETEK Ltd.).

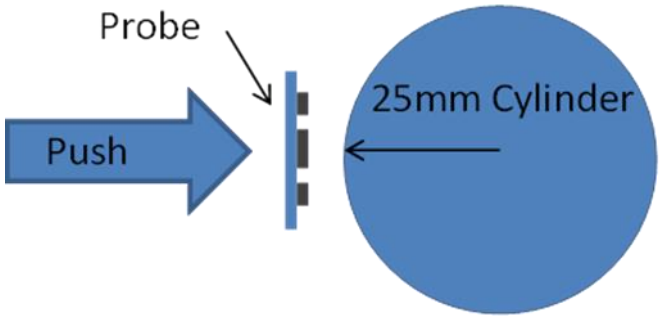

Fig.6. 8 A sketch of bending test setup: the probe is pushed manually to fit the curve of a cylinder

6.2.4.2 Validation through physiological test

As shown in Fig.6.9, the probe's signals were captured by a 4-channel PPG board (DISCO4, Dialog Devices Ltd., UK). The analog-to-digital conversion for these captured PPG signals was

implemented by a data acquisition board (USB-6009, National Instruments Co., USA), and the control software of the PPG board was performed by LabView 7.1 (National Instruments Co., USA).

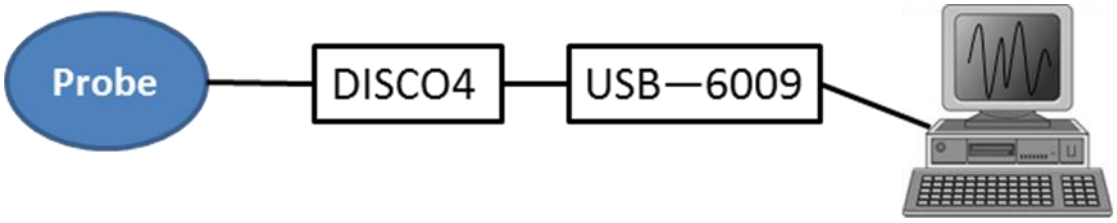

Fig.6. 9 Experimental setups of assessment system (rPPG probe Type One)

Type Two is compared with a commercial probe to validate its performance. Both the prototype probe patch and a commercial forehead contact pulse oximetry sensor (Nellcor™ Max-Fast™, COVIDIEN) were placed on the participant's forehead (Fig.6.10). So the signals from two probes were captured simultaneously. During the signal recording, the participant sat still for 5 minutes.

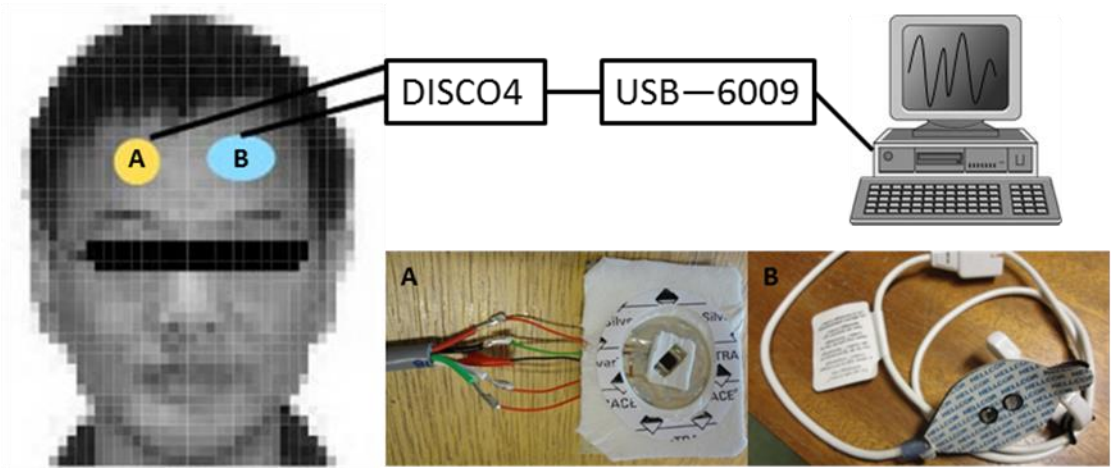

Fig.6. 10 Physiological assessment setup, A) the commercial forehead contact pulse oximetry sensor, Nellcor™ Max-Fast™, COVIDIEN, B) the rPPG probe Type Two

6.3 Results and discussion

6.3.1 Probe manufacture

The dimension shrinkage of each specimen was listed in Table.6.1, and Fig.6.11 shows the photos taken before heating and after each heating stage. The deformation and shrinkage of the substrate will cause the dislocation of components and induce thermal stress thus affect the

probe's accuracy and reliability. The PEN laminate was more stable than the PET laminate during the heating stages. Therefore, PEN copper laminate was chosen because of better accuracy and reliability of FPCB.

Table.6. 1 Transverse dimension shrinkage of test specimens

	After stage 1	After stage 2	After stage 3
PEN	0.5%	1.1%	5.7%
PET	5.1%	17.2%	81.6%

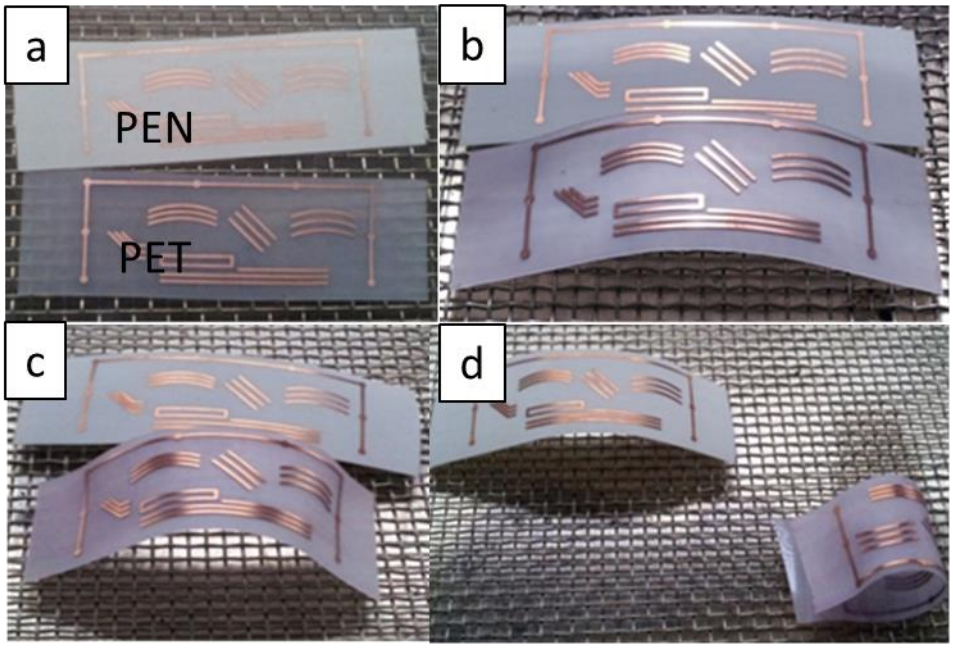

Fig.6. 11 Photos of specimen deformation after each heating stage. A: Before heating, B: After stage 1, C: After stage 2, D: After stage 3.

Most currently commercial lead-free solders, such as tin/silver (Sn/Ag), tin/silver/copper (Sn/Ag/Cu), have higher melting temperatures (T_m of Sn/Ag and Sn/Ag/Cu are 217 and 221 ^oC, respectively) than of the conventional tin–lead eutectic solder (183 ^oC) [137]. According to the temperature limits identified above, the lead-free solder technology is not suitable for manufacturing the rPPG probe based on PEN substrates. Moreover, the processing window for LED/PD soldering is very narrow, which increase the requirements and cost of components mounting. Compared to the soldering technology, ICAs offer numerous advantages, such as

environmental friendliness, fewer processing steps, and most important advantage in our application, lower processing temperature. Based on previous research (Chapter 4), the curing temperature can be as low as 100^{o}C.

The layout of Type One and Type Two are shown below (Fig.6.12 and 6.13). The tolerance of the centre-to-centre distance between the photodiode and LED is the radius of photodiode's sensitive area. In probe Type One, the photodiode has a relatively small sensing area. Thus the LEDs are placed very close to the photodiode outer package, causing inconvenience in component-mounting and photodiode-isolating. In the upgrade version - Type Two, bigger sensitive area photodiode was used to gain more PCB design freedom and reduce the impact from PCB fabrication inaccuracy and mounting misalignment.

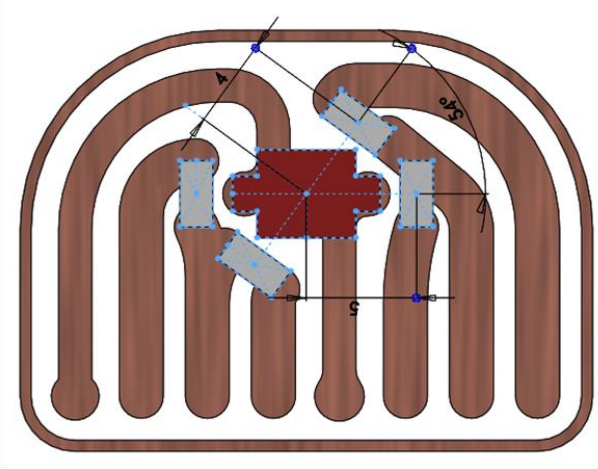

Fig.6. 12 The sketch of Type One probe's circuit. The big block in the middle represents the photodiode, and the four blocks around it are LEDs.

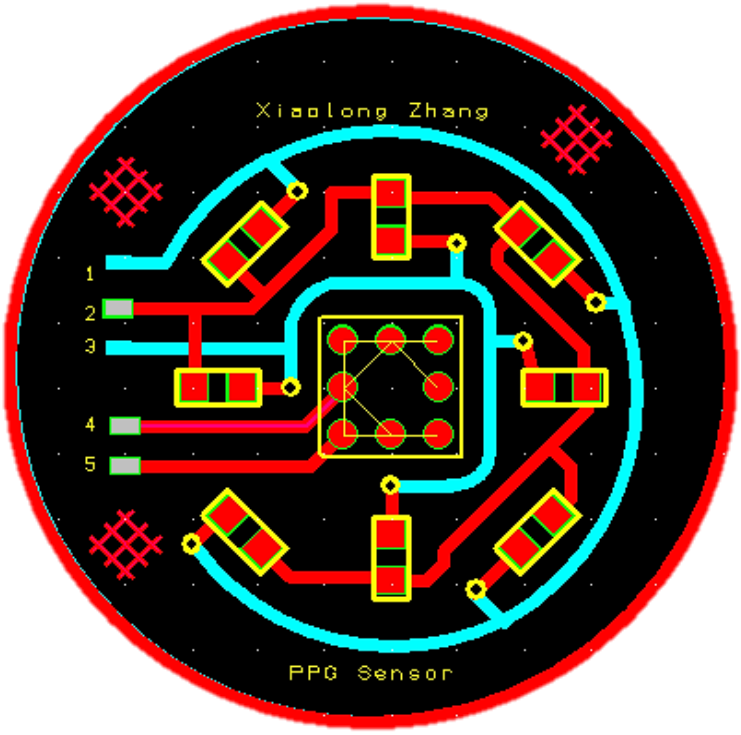

Fig.6. 13 The layout of the double-side PCB for probe Type Two. The dark (red) tracks are on the top side, and the light (white) tracks are on the bottom side

Different sizes of apertures were tested. (Fig.6.14) The ECA needs to be spread around the vias on both sides to gain mechanical strength and electrical conductivity, so the apertures will be bigger than the vias to form solid connections. However, the big hole will consume more adhesive, otherwise, form a hollow. The gap between stencil and PCB caused spreading which would form a short between adjacent lines. The optimal size in this study is 1.2mm in diameter. There is a shift when drilling the holes manually which caused an alignment problem. The ECA would be blocked when the aperture was placed away from the vias (Fig.6.15).

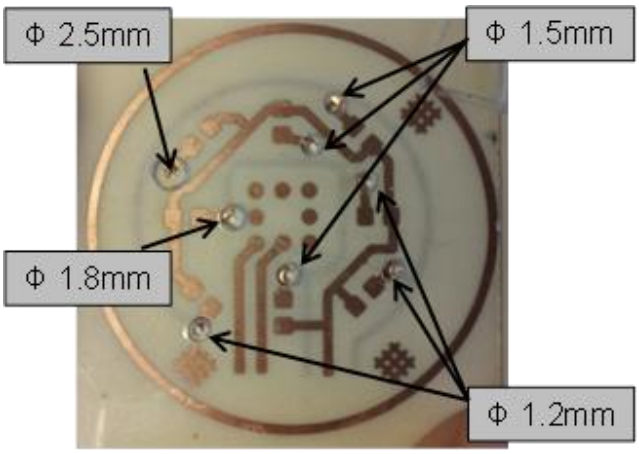

Fig.6. 14 Different sizes of the stencil apertures

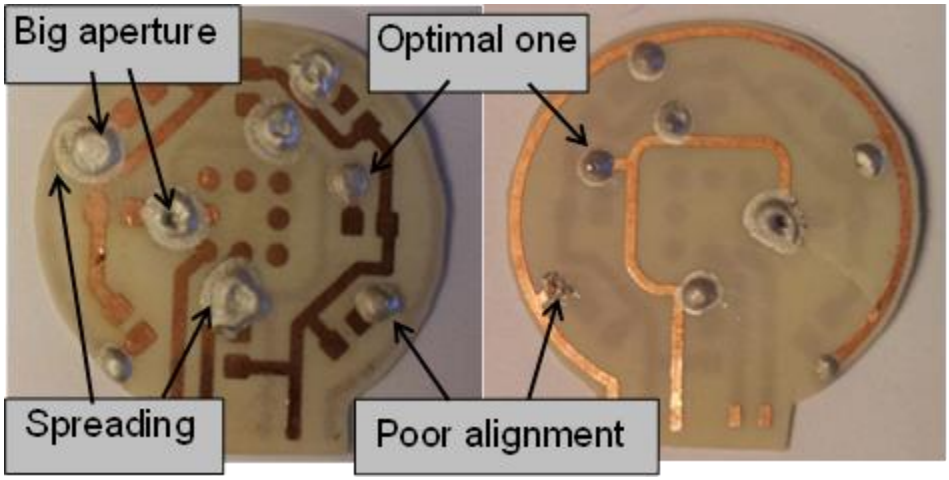

Fig.6. 15 Stencil printing results

A new set of stencils were made by drilling ϕ1 mm holes in 150 μm thick PET copper laminates. Fig.6.16 shows that reducing the thickness of the stencil would enable finer printing feature. The bottom diameter of this via cap is 0.88 mm.

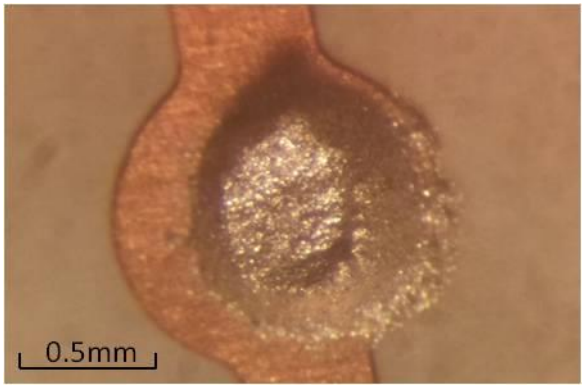

Fig.6. 16 Top view image of a via plug made by 150μm thick stencil

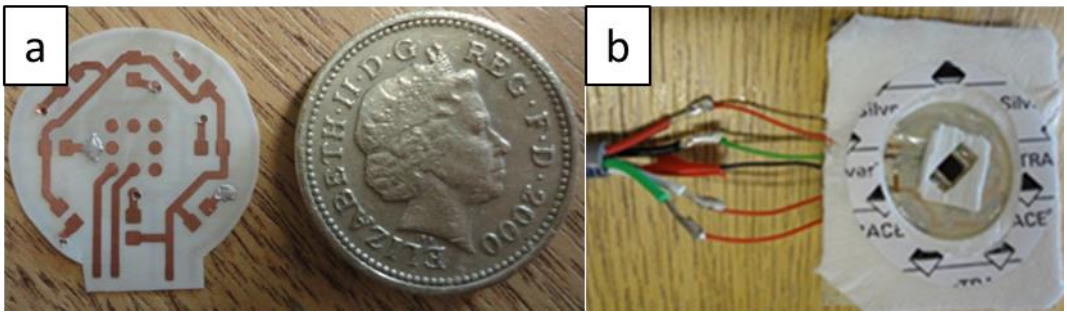

Fig.6. 17 a) Flexible printed circuit board (top side) and a one-pound coin, b) packaged rPPG sensor

6.3.2 Functional test

The bending test preliminarily proved that the ICA bonding could provide reasonable lifetime for biomedical monitoring applications. As shown in Table 6.2, the electrical property of each loop in Type Two probe remained the same after 100 cycles. After connecting this probe to assessment system, all LEDs worked properly, and the photodiode received meaningful signals. (Fig.6.18)

Table.6. 2 Forward voltage drop of each component's channel

Channel / Cycles	Red LED	Infrared LED	Photodiode
Before bending	1.661 V	1.480 V	0.551 V
After 20 cycles	1.661 V	1.480 V	0.551 V
After 100 cycles	1.661 V	1.479 V	0.549 V

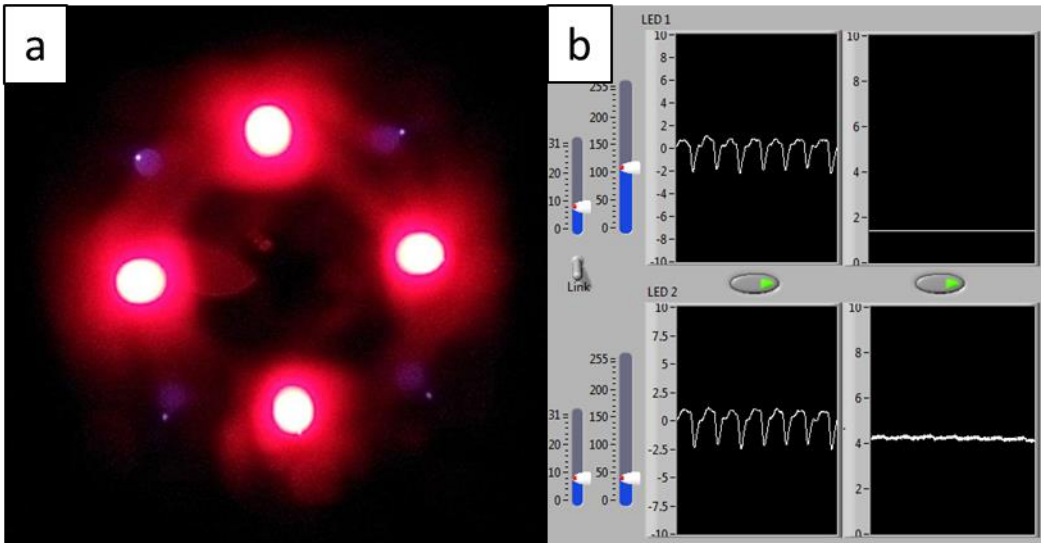

Fig.6. 18 Work status test after 100 bending cycles, a) a photo of Type Two probe in dark room, b) probe's signals and driven currents in control software

The probe Type One was attached to a thumb of the participant. Its signals (Fig.6.19) are clear, but the waveform is not ideal, so we can only get the heart rate of the participant. Some signal segments of probe Type Two are shown in the Fig.6.20, the solid lines are prototype's signals, and the dot lines are signals from the commercial one. The overall shape of the curves is the

same which indicate the prototype has the same accuracy level as the commercial one. And thanks to the special selective components and reasonable manufacturing, the current consumption of the probe Type Two (21.76 mA) is only 39.8% of the commercial one (54.7 mA). Besides, the symmetrical ring-like LEDs arrangement would give the prototype probe a better motion cancellation [138, 139]. Physiological assessment result shows that the mild assembly processes based on the ICAs can protect the delicate components and substrates, thus fully achieve the probe's design.

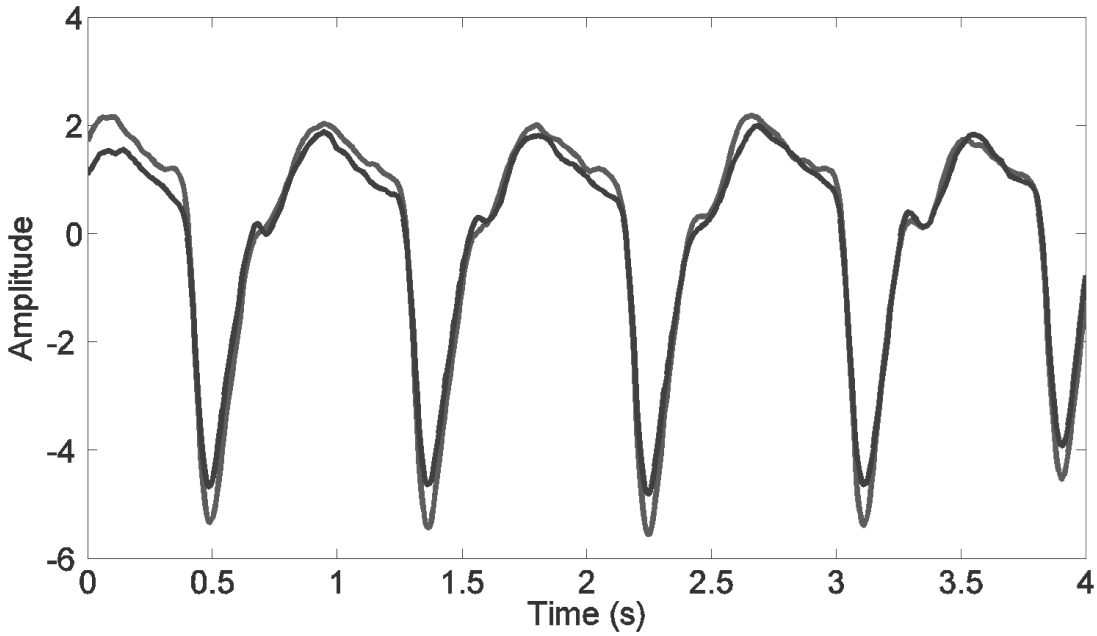

Fig.6. 19 A segment of signals generated from the probe Type One

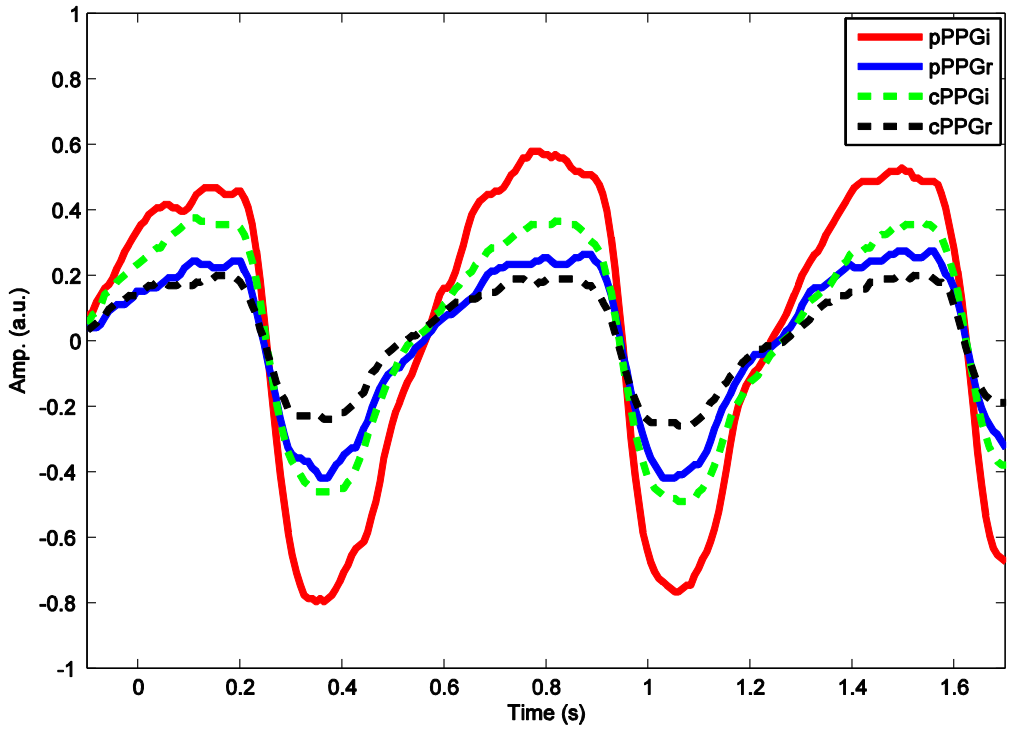

Fig.6. 20 The waveform of signals when staying still. The Y-axis is the amplitude of the signal, and the X-axis is the time. pPPGi= infrared LED channel of the prototype, pPPGr= red LED channel of the prototype, cPPGi= infrared LED channel of the commercial probe, cPPGr= red LED channel of the commercial probe.

6.4 Conclusions

PEN film is a light-weight flexible and cheap substrate that helps to make rPPG patch probe user-comfortable and well fitting. High efficient and sensitive photodiode and LED ensure the probe high performance. But conventional soldering may degrade the substrate and components. The assembled probes in this research are all functional and show the outstanding performance, which demonstrated the feasibility of bonding optoelectronics and flexible substrates together by electrically conductive adhesive under low temperature. ICA-based low-temperature manufacture processes also enable the integration of other flexible but delicate components in the future, such as polymer optical fibres, polymer microlens and printed organic electronics. In the manufacturing routes, a modified stencil printing setup, which merges two printing-curing steps into one, was developed to save both time and energy.

Based on the works done in this chapter, thinner substrate can be tried for more flexibility and user-comfort. Smaller aperture size and thinner stencil will be utilised to form fine and neat via interconnection for further miniaturisation. The double stencil setup can also be transferred to

an industrial-scale stencil print machine which can provide better control of all the parameters, e.g. print pressure, print speed and squeeze angle to enhance the printing quality.

Chapter 7 Conclusions and Future work

7.1 Main conclusions

Based on the presented experimental and modelling results in previous chapters, the main findings in this research are summarised in this chapter.

7.1.1 Curing effect on vias

The research of curing effect on via performance was first carried out by studying the relationship between curing conditions and material properties. Based on DSC analysis results, two-parameter autocatalytic model (Sestak-Berggren model) was established as the most suitable curing process description of our typical ICA composed of epoxy-based binders and Ag filler particles. The conversion level of studied ICA in an isothermal cure schedule was predicted by the kinetic equation: $\frac{d\alpha}{dt} = 1.306 \times 10^5 \, exp\left(-\frac{50690}{RT}\right) \alpha^{0.031}(1-\alpha)^{0.912}$. Based on the theoretical analysis, the varying curing conditions were selected. Samples cured at 100 ^{o}C or 150 ^{o}C was near full conversion which ensured electrical conductivity. While samples cured at 50 ^{o}C for 10 minutes exhibited poor conductivity due to the low conversion level. Therefore, ultra-low temperature cure process for the ICA required long processing time to achieve satisfied conversion level. Further, a link between curing conditions and the mechanical properties of ICAs was found by DMA experiments. At low conversion level, the elastic modulus of ICA increases while the conversion level rises. When the conversion is approaching 100%, the elastic modulus of ICA may decrease. Combining with the SEM images of epoxy structure, it was identified that samples cured at 100 ^{o}C for 10 minutes owned best mechanical properties.

A series of test vehicles with ICA vias were cured follow the above curing processes. The electrical resistance of via decreases significantly when ICA conversion level is rising. In consideration of conductivity, process time and temperature, 100 ^{o}C and 6 minutes were the optimised curing temperature and time for the studied ICA. Resistances of the vias were measured before testing and in real time during thermal cycling tests, damp heat tests and bending tests. During thermal tests, the vias cured at higher temperature had superior reliability compared to the vias cured at a lower temperature. Reliability of vias cured at 50 ^{o}C was

extremely poor in bending test due to the low conversion. Although the mechanical properties of ICA cued at 100 ^{o}C was better, the resistance increments of vias cured at 100 ^{o}C in bending tests were larger than the vias cured at 150 ^{o}C. It because the Ag particles were more closely contacted in the vias cured at 150 ^{o}C, which weaken the impact on resistance caused by tiny cracks in epoxy.

7.1.2 Geometry effect and fistula-shape via

Finite element model of ICA via was used to aid better understanding of the electrical conduction mechanisms. The simulations suggested that current in ICA vias would exhibit similar characteristics like in homogeneous conductive material and most current flew through the outer tubular part of the ICA fill.

A simplified model was built to represent rivet-shaped vias in the FPCBs based on the assumption of homogenous ICA. An equation was proposed to calculate the resistance of the model. In this research, all the FPCBs are the same thus the only variable in the model was the cap size of the via. Vias with different cap sizes were tested and validated the equation. The vias resistances dropped sharply from no cap to double caps structure. The vias resistances kept decreasing while the cap diameter increases, and the decline rate in resistance slowed down after the cap diameter overpass a certain value, 0.5 mm for the test vehicles in this research. Furthermore, those samples were divided into three groups for thermal cycling test, damp heat ageing test and bending test. The results show that the large cap and double caps structure can improve the reliability.

Based on theoretical equation and simulation model, the fistula-shape ICA via was developed. Its hollow nature provides the space for integrations of the optical or fluidic circuit. Resistance measurement and reliability tests proved that carefully designed and manufactured small bores in vias will not comprise the performance. In this study, the recommendation of bore diameter in Φ0.6 mm rivet-shaped via is 0.3 mm max.

7.1.3 Multifunctional vertical interconnects

This research has successfully demonstrated the feasibility of multifunctional vertical interconnects in flexible substrates. Test vehicles with optoelectrical vias were made through two different approaches to prove the concept.

Direct writing, an additive manufacture method, was used to fill the via hole and forming the planar waveguide on the substrate in one process. It was a quick and flexible way to form optical vertical interconnects, but the quality of the waveguide highly depends on the capability of manufacturing facilities.

On the other hand, plastic optical fibre integration required no high-end equipment. Ready-made fibres are easy to access. In this study, Φ0.25 mm PMMA fibre (core diameter 0.24 mm) was integrated through fistula-shape ICA vias. After installation, the minimum bending radius of the fibre is 0.7 mm, and the optical loss increment is around 0.2 dB which is acceptable. The downside of this method is that the curved fibre occupied a lot of space, thus increase the height of the whole package.

7.1.4 Case study: reflection PPG probe manufacture

In this research, reflection Photoplethysmography (rPPG) sensors using specially designed photodiode-LEDs system were assembled on flexible PCBs by ICAs. The PCB substrate, PEN film, is a light-weight flexible and cheap substrate that helps to make rPPG patch probe user-comfortable and well fitting. High efficient and sensitive photodiode and LED ensured high performance of the probe. ICA-based low-temperature manufacture processes were developed to enable the integration of these flexible but delicate substrate and components. In the manufacturing routes, a modified stencil printing setup, which merges two printing-curing steps (vias forming and components bonding) into one step, was developed to save both time and energy. The assembled probes showed the outstanding performance in functional and physiological tests. Based on the works done in this case study, the thinner substrate can be tried for more flexibility and user-comfort. Smaller aperture size and thinner stencil will be utilised to form fine and neat via interconnection for further miniaturisation. The double stencil setup can also be transferred to an industrial-scale stencil print machine which can provide

better control of all the parameters, e.g. print pressure, print speed and squeeze angle to enhance the printing quality.

7.2 Future works

Due to the limited time and constraints of research facilities, a number of areas have not been fully investigated. Some new areas worthy of future work have been identified during this research. Therefore, the recommendations for future work are presented as follows.

7.2.1 Further research on geometry and curing effect

Referring the outcome of the research, the different shape and distribution of fillers may vary the geometry effect on ICA vias, and the curing effect is linked to binder's properties. Therefore, ICAs made from different binders (silicone or other elastic polymers) and fillers (silver-polymer spheres or nanomaterials) can be studied to gain a comprehensive understanding of geometry and curing effect on the conductivity and reliability of vias. And long-term reliability tests are also needed for lifetime analysis.

7.2.2 Additive manufacture for optoelectrical vias

There was only a trial on additive manufacture in this research. Based on the manufacturing machine, e.g. inkjet printing machine, a lot of technique problems need to be solved. In order to print a fine optical via, deeper research on solution preparation, substrate surface treatment, deposition speed and temperature is needed. The optical performance and reliability of printed vias can be tested and compared with the vias formed from the optical fibre in this research.

7.2.3 Interactions in multifunctional vias

Different materials were integrated into one via to achieve multifunction. The interactions between each functional vias when working together and the mechanical behaviours during bending are worth of further research. For example, the effect of electromagnetic field or temperature elevation becomes an issue when optoelectrical vias are working under high current or high-frequency conditions. Finite element analysis would be a powerful tool to assist such experimental investigation.

7.2.4 Multifunctional vias in POCT device

Based on the research in this thesis, more complicated POCT device can be enabled by multifunctional vias in the future. As shown in Fig.7.1, electrical circuits and optical circuits are built on multi-layered flexible substrates and vertically connected. And the optical waveguide can also be adopted in sensing systems as the illuminator or receiver which gives more freedom to the arrangement of photonics.

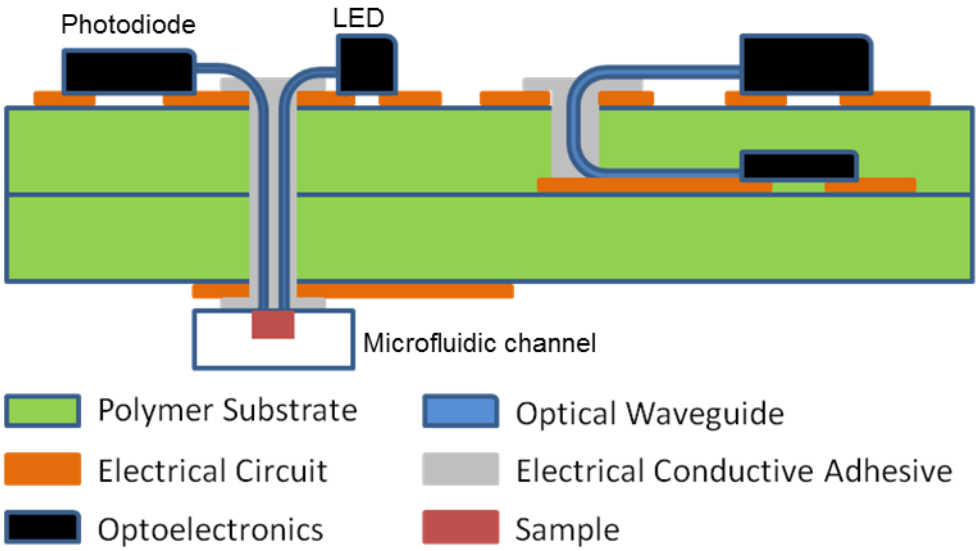

Fig.7. 1 A schematic diagram of a POCT device using fibres in sensing and interconnects

References

[1] C. Willmott and J. E. Arrowsmith, ‘Point-of-care testing’, *Surgery (Oxford)*, vol. 28, no. 4, pp. 159–160, 2010.

[2] E. Lee-Lewandrowski and K. Lewandrowski, ‘Point-of-care testing. An overview and a look to the future.’, *Clinics in laboratory medicine*, vol. 21, no. 2, p. 217–239, vii, 2001.

[3] P. B. Luppa, C. Mueller, A. Schlichtiger, and H. Schlebusch, ‘Point-of-care testing (POCT): Current techniques and future perspectives’, *TrAC Trends in Analytical Chemistry*, vol. 30, no. 6, pp. 887–898, 2011.

[4] Y. Xia, J. Si, and Z. Li, ‘Fabrication techniques for microfluidic paper-based analytical devices and their applications for biological testing: A review’, *Biosensors and Bioelectronics*, vol. 77, pp. 774–789, 2016.

[5] T. Jaakola, M. Lahti, J. Petaja, and K. Kautio, ‘Low Cost Printed Flexible Multilayer Substrates’, in *Electronics Packaging Technology Conference*, 2008, pp. 344–349.

[6] W. Christiaens, T. Torfs, W. Huwel, C. Van Hoof, and J. Vanfleteren, ‘3D integration of ultra-thin functional devices inside standard multilayer flex laminates’, *European Journal of Operational Research*, vol. 123, pp. 125–144, 2009.

[7] K. Y. Chen, R. L. D. Zenner, M. Arneson, and D. Mountain, ‘Ultra-thin electronic device package’, *IEEE Transactions on Advanced Packaging*, vol. 23, no. 1, pp. 22–26, 2000.

[8] M. M. Tentzeris, R. Vyas, V. Lakafosis, A. Traille, A. Rida, and G. Shaker, ‘Inkjet-printed system-on-paper/polymer “green” RFID and wireless sensors’, in *Proceedings - Electronic Components and Technology Conference*, 2010, pp. 1552–1555.

[9] P. St-Louis, ‘Status of point-of-care testing: Promise, realities, and possibilities’, *Clinical Biochemistry*, vol. 33, no. 6, pp. 427–440, 2000.

[10] Z. Chen, C. Fang, G. Qiu, J. He, and Z. Deng, ‘Non-enzymatic disposable test strip for detecting uric acid in whole blood’, *Journal of Electroanalytical Chemistry*, vol. 633, no. 2, pp. 314–318, 2009.

[11] T. Monteiro, P. R. Rodrigues, A. L. Gonçalves, J. J. G. Moura, E. Jubete, L. Añorga, B. Piknova, A. N. Schechter, C. M. Silveira, and M. G. Almeida, ‘Construction of effective disposable biosensors for point of care testing of nitrite’, *Talanta*, vol. 142, pp. 246–251, 2015.

[12] C. Gao, X. Zhu, J. W. Choi, and C. H. Ahn, ‘A disposable polymer field effect transistor (FET) for pH measurement’, *TRANSDUCERS 2003 - 12th International Conference on Solid-State Sensors, Actuators and Microsystems, Digest of Technical Papers*, vol. 2, pp. 1172–1175, 2003.

[13] V. Sundaram, R. R. Tummala, F. Liu, P. A. Kohl, J. Li, S. A. Bidstrup-Allen, and Y. Fukuoka, ‘Next-generation microvia and global wiring technologies for SOP’, *IEEE Transactions on Advanced Packaging*, vol. 27, no. 2, pp. 315–325, 2004.

[14] J. H. Lau, C. Chang, C. World, and V. Iss, ‘An overview of microvia technology’, *Circuit World*, vol. 26, no. 2, pp. 22–32, 2000.

[15] G. Matijasevic, P. Gandhi, and C. Gallagher, ‘Vertical microvia connections achieved using a unique conductive composite material’, in *IEMT/IMC Proceedings*, 1998, pp. 306–311.

[16] J. Courbat, D. Briand, J. Wöllenstein, and N. F. De Rooij, ‘Polymeric foil optical waveguide with inkjet printed gas sensitive film for colorimetric sensing’, *Sensors and Actuators, B: Chemical*, vol. 160, no. 1. pp. 910–915, 2011.

[17] H. F. Lee, C. Y. Chan, and C. S. Tang, ‘Embedding capacitors and resistors into printed circuit boards using a sequential lamination technique’, *Journal of Materials Processing Technology*, vol. 207, no. 1–3, pp. 72–88, 2008.

[18] T. Sekitani, U. Zschieschang, H. Klauk, and T. Someya, ‘Flexible organic transistors and circuits with extreme bending stability.’, *Nature materials*, vol. 9, no. 12. pp. 1015–1022, 2010.

[19] M. Berggren, D. Nilsson, and N. D. Robinson, ‘Organic materials for printed electronics.’, *Nature materials*, vol. 6, no. 1, pp. 3–5, 2007.

[20] J. van den Brand, M. Saalmink, M. Barink, and A. Dietzel, ‘Novel lamination and interconnection technologies demonstrated in a flexible modular optical sensor array for wound monitoring’, *Microelectronic Engineering*, vol. 87, no. 5–8. pp. 769–772, 2010.

[21] Y. Li and C. P. Wong, ‘Recent advances of conductive adhesives as a lead-free alternative in electronic packaging: Materials, processing, reliability and applications’, *Materials Science and Engineering R: Reports*, vol. 51, no. 1–3. pp. 1–35, 2006.

[22] M. Catelani, V. L. Scarano, F. Bertocci, and R. Berni, ‘Optimization of the soldering process with ECAs in electronic equipment: Characterization measurement and experimental design’, *IEEE Transactions on Components, Packaging and Manufacturing Technology*, vol. 1, no. 10, pp. 1616–1626, 2011.

[23] I. Mir and D. Kumar, ‘Recent advances in isotropic conductive adhesives for electronics packaging applications’, *International Journal of Adhesion and Adhesives*, vol. 28, no. 7. pp. 362–371, 2008.

[24] E. Bosman, G. Van Steenberge, P. Geerinck, W. Christiaens, J. Vanfleteren, and P. Van Daele, ‘Embedding of optical interconnections in flexible electronics’, *Proceedings - Electronic Components and Technology Conference*, pp. 1281–1287, 2007.

[25] M. Immonen, J. Wu, H. J. Yan, L. X. Zhu, P. Chen, and T. Rapala-Virtanen, ‘Development of electro-optical PCBs with embedded waveguides for data center and high performance computing applications’, *SPIE Photonics West 2014-OPTO: Optoelectronic Devices and Materials*, vol. 8991, p. 899113, 2014.

[26] M. Immonen, J. Wu, H. J. Yan, P. Chen, J. X. Xu, and T. Rapala-Virtanen, ‘Development of electro-optical PCBs with polymer waveguides for high-speed intra-system interconnects’, *Circuit World*, vol. 38, no. 3, pp. 104–112, 2012.

[27] B. H. Ma, A. K. Jen, and L. R. Dalton, ‘Polymer-Based Optical Waveguides : Materials , Processing , and Devices’, *Advanced Materials*, vol. 14, no. 19, pp. 1339–1365, 2002.

[28] S. Kopetz, E. Rabe, and A. Neyer, ‘High-temperature stable flexible polymer waveguide laminates’, *Electronics Letters*, vol. 42, no. 11, p. 634, 2006.

[29] J. K. Park, ‘Lab-on-a-chip technology for integrative bioengineering’, in *2010 10th IEEE Conference on Nanotechnology, NANO 2010*, 2010, pp. 156–159.

[30] J. Wu and M. Gu, ‘Microfluidic sensing: state of the art fabrication and detection techniques.’, *Journal of biomedical optics*, vol. 16, no. 8. p. 80901, 2011.

[31] ‘Bioengineering-Lawrence Livermore National Laboratory’. [Online]. Available: https://www-eng.llnl.gov/bio_tech/bio_tech_sample.html. [Accessed: 05-Jun-2012].

[32] J. L. Fu, Q. Fang, T. Zhang, X. H. Jin, and Z. L. Fang, ‘Laser-induced fluorescence detection system for microfluidic chips based on an orthogonal optical arrangement’, *Analytical Chemistry*, vol. 78, no. 11. pp. 3827–3834, 2006.

[33] F. B. Myers and L. P. Lee, ‘Innovations in optical microfluidic technologies for point-of-care diagnostics.’, *Lab on a chip*, vol. 8, no. 12, pp. 2015–2031, 2008.

[34] O. Mudanyali, S. Dimitrov, U. Sikora, S. Padmanabhan, I. Navruz, and A. Ozcan, ‘Integrated rapid-diagnostic-test reader platform on a cellphone.’, *Lab on a chip*, vol. 12, no. 15, pp. 2678–86, 2012.

[35] P. Shi, V. A. Peris, A. Echiadis, J. Zheng, Y. S. Zhu, P. Y. S. Cheang, and S. J. Hu, ‘Non-contact Reflection Photoplethysmography Towards Effective Human Physiological Monitoring’, *Journal of Medical and Biological Engineering*, vol. 30, no. 3. pp. 161–167, 2010.

[36] Y. Wan, X. Sun, and J. Yao, ‘Design of a Photoplethysmographic Sensor for Biometric Identification’, in *ICCAS 2007 - International Conference on Control, Automation and Systems*, 2007, vol. 47, pp. 1897–1900.

[37] J. Allen, ‘Photoplethysmography and its application in clinical’, *Physiological Measurement*, vol. 28, no. 3. p. R1, 2007.

[38] R. Erts, E. Kviesis-Kipge, J. Zaharans, E. Zaharans, and J. Spigulis, ‘Wireless photoplethysmography finger sensor probe’, in *BEC 2010 - 2010 12th Biennial Baltic Electronics Conference, Proceedings of the 12th Biennial Baltic Electronics Conference*, 2010, pp. 283–284.

[39] J. A. C. Patterson, D. G. McIlwraith, and Y. Guang-Zhong, ‘A Flexible, Low Noise Reflective PPG Sensor Platform for Ear-Worn Heart Rate Monitoring’. 2009.

[40] B. Jönsson, C. Laurent, T. Skau, and L. G. Lindberg, ‘A new probe for ankle systolic pressure measurement using Photoplethysmography (PPG)’, *Annals of Biomedical Engineering*, vol. 33, no. 2, pp. 232–239, 2005.

[41] C. P. C. Park, J.-C. S. J.-C. Sohn, J.-H. K. J.-H. Kim, and H.-J. C. H.-J. Choi, ‘Artifact-resistant design of a wrist-type heart rate monitoring device’, *2009 11th International Conference on Advanced Communication Technology*, vol. 3, pp. 2313–2316, 2009.

[42] Y. Lee, H. Shin, J. Jo, and Y. K. Lee, ‘Development of a wristwatch-type PPG array sensor module’, in *Digest of Technical Papers - IEEE International Conference on Consumer Electronics*, 2011, pp. 168–171.

[43] S. Rhee, B. H. Yang, and H. H. Asada, ‘Artifact-resistant power-efficient design of finger-ring plethysmographic sensors’, *IEEE Transactions on Biomedical Engineering*, vol. 48, no. 7. pp. 795–805, 2001.

[44] S. Hu, J. Zheng, and V. A. Peris, ‘A study of opto-physiological modeling to quantify tissue absorbance in imaging photoplethysmography’, *2010 Annual International Conference of the IEEE Engineering in Medicine and Biology Society, EMBC’10*. pp. 5776–5779, 2010.

[45] Y. Sun, S. Hu, V. Azorin-Peris, S. Greenwald, J. Chambers, and Y. Zhu, ‘Motion-compensated noncontact imaging photoplethysmography to monitor cardiorespiratory status during exercise.’, *Journal of biomedical optics*, vol. 16, no. 7, p. 77010, 2011.

[46] Y. Sun and N. Thakor, ‘Photoplethysmography Revisited: From Contact to Noncontact, from Point to Imaging’, *IEEE Transactions on Biomedical Engineering*, vol. 63, no. 3. pp. 463–477, 2016.

[47] J. Zheng, S. Hu, V. Azorin-Peris, A. Echiadis, V. Chouliaras, and R. Summers, ‘Remote simultaneous dual wavelength imaging photoplethysmography: a further step towards 3-D mapping of skin blood microcirculation’, *Proceedings of SPIE*, vol. 6850, no. Multimodal Biomedical Imaging III, p. 68500S--1--8, 2008.

[48] D. J. Lipomi, M. Vosgueritchian, B. C.-K. Tee, S. L. Hellstrom, J. a Lee, C. H. Fox, and Z. Bao, 'Skin-like pressure and strain sensors based on transparent elastic films of carbon nanotubes.', *Nature nanotechnology*, vol. 6, no. 12, pp. 788–92, 2011.

[49] F. R. Fan, L. Lin, G. Zhu, W. Wu, R. Zhang, and Z. L. Wang, 'Transparent triboelectric nanogenerators and self-powered pressure sensors based on micropatterned plastic films', *Nano Letters*, vol. 12, no. 6, pp. 3109–3114, 2012.

[50] M.-Y. Cheng, X.-H. Huang, C.-W. Ma, and Y.-J. Yang, 'A flexible capacitive tactile sensing array with floating electrodes', *Journal of Micromechanics and Microengineering*, vol. 19, no. July, p. 115001, 2009.

[51] C. Pang, G.-Y. Lee, T. Kim, S. M. Kim, H. N. Kim, S.-H. Ahn, and K.-Y. Suh, 'A flexible and highly sensitive strain-gauge sensor using reversible interlocking of nanofibres', *Nature Materials*, vol. 11, no. 9, pp. 795–801, 2012.

[52] L. F. Wang, J. Q. Liu, B. Yang, X. Chen, and C. S. Yang, 'Fabrication and characterization of a dry electrode integrated Gecko-inspired dry adhesive medical patch for long-term ECG measurement', *Microsystem Technologies*, vol. 21, no. 5, pp. 1093–1100, 2015.

[53] W. G. Bae, D. Kim, M. K. Kwak, L. Ha, S. M. Kang, and K. Y. Suh, 'Enhanced Skin Adhesive Patch with Modulus-Tunable Composite Micropillars', *Advanced Healthcare Materials*, vol. 2, no. 1, pp. 109–113, 2013.

[54] D.-H. Kim, J. Viventi, J. J. Amsden, J. Xiao, L. Vigeland, Y.-S. Kim, J. A. Blanco, B. Panilaitis, E. S. Frechette, D. Contreras, D. L. Kaplan, F. G. Omenetto, Y. Huang, K.-C. Hwang, M. R. Zakin, B. Litt, and J. A. Rogers, 'Dissolvable films of silk fibroin for ultrathin conformal bio-integrated electronics', *Nature Materials*, vol. 9, no. 6, pp. 511–517, 2010.

[55] F. Axisa, D. Brosteaux, E. De Leersnyder, F. Bossuyt, M. Gonzalez, N. De Smet, E. Schacht, M. Rymarczyk-Machal, and J. Vanfleteren, 'Low cost, biocompatible elastic and conformable electronic technologies using mid in stretchable polymer', *Annual International Conference of the IEEE Engineering in Medicine and Biology - Proceedings*, pp. 6592–6595, 2007.

[56] M. Lee, C. Y. Chen, S. Wang, S. N. Cha, Y. J. Park, J. M. Kim, L. J. Chou, and Z. L. Wang, 'A hybrid piezoelectric structure for wearable nanogenerators', *Advanced Materials*, vol. 24, no. 13, pp. 1759–1764, 2012.

[57] A. Nathan, A. Ahnood, M. T. Cole, S. Lee, Y. Suzuki, P. Hiralal, F. Bonaccorso, T. Hasan, L. Garcia-Gancedo, A. Dyadyusha, S. Haque, P. Andrew, S. Hofmann, J. Moultrie, D. Chu, A. J. Flewitt, A. C. Ferrari, M. J. Kelly, J. Robertson, G. A. J. Amaratunga, and W. I. Milne, 'Flexible electronics: The next ubiquitous platform', *Proceedings of the IEEE*, vol. 100, no. SPL CONTENT, pp. 1486–1517, 2012.

[58] W. a MacDonald, M. K. Looney, D. MacKerron, R. Eveson, R. Adam, K. Hashimoto, and K. Rakos, 'Latest advances in substrates for flexible electronics', *Journal of the Society for Information Display*, vol. 15, no. 12, pp. 1075–1083, 2007.

[59] J. A. Davis, R. Venkatesan, A. Kaloyeros, M. Beylansky, S. J. Souri, K. Banerjee, K. C. Saraswat, A. Rahman, R. Reif, and J. D. Meindl, 'Interconnect limits on gigascale integration (GSI) in the 21st century', *Proceedings of the IEEE*, vol. 89, no. 3, pp. 305–322, 2001.

[60] A. C. Hübler, G. C. Schmidt, H. Kempa, K. Reuter, M. Hambsch, and M. Bellmann, 'Three-dimensional integrated circuit using printed electronics', *Organic Electronics*, vol. 12, no. 3, pp. 419–423, 2011.

[61] C. Q. Cui and K. Pun, 'Cu fully filled ultra-fine blind via on flexible substrate for high density interconnect', *Proceedings of the IEEE/CPMT International Electronics Manufacturing Technology (IEMT) Symposium*. pp. 13–19, 2006.

[62] C. W. P. Shi, X. S. X. Shan, G. Tarapata, R. Jachhowicz, C. W. Lu, and H. T. Hui, 'Fabrication of wireless sensor platform on transparent flexible film using screen printing and via interconnect', *Design Test Integration and Packaging of MEMS/MOEMS (DTIP), 2010 Symposium on*, no. May, pp. 9–14, 2010.

[63] G. Wang, E. C. Folk, F. Barlow, and A. Elshabini, 'Fabrication of microvias for multilayer LTCC substrates', *IEEE Transactions on Electronics Packaging Manufacturing*, vol. 29, no. 1, pp. 32–41, 2006.

[64] K. Pun, C. Q. Cui, and T. F. Chung, ‘Ultra-fine via pitch on flexible substrate for High Density Interconnect (HDI)’, *Proceedings, 2008 International Conference on Electronic Packaging Technology and High Density Packaging, ICEPT-HDP 2008*, 2008.

[65] R. Mandamparambil, H. Fledderus, J. Van Den Brand, M. Saalmink, R. Kusters, T. Podprocky, G. Van Steenberge, J. De Baets, and A. Dietzel, ‘A comparative study of via drilling and scribing on PEN and PET substrates for flexible electronic applications using excimer and Nd:YAG laser sources’, in *2009 Flexible Electronics and Displays Conference and Exhibition, FLEX 2009*, 2009.

[66] E. Beyne, ‘Multilayer thin-film technology enabling technology for solving high-density interconnect and assembly problems’, *Nuclear Instruments and Methods in Physics Research, Section A: Accelerators, Spectrometers, Detectors and Associated Equipment*, vol. 509, no. 1–3, pp. 191–199, 2003.

[67] K. Jain, M. Klosner, M. Zemel, and S. Raghunandan, ‘Flexible electronics and displays: High-resolution, roll-to-roll, projection lithography and photoablation processing technologies for high-throughput production’, *Proceedings of the IEEE*, vol. 93, no. 8, pp. 1500–1510, 2005.

[68] H. Holden, ‘Microvias: the next generation of substrates and packages’, *IEEE Micro*, vol. 18, no. 4, pp. 10–16, 1998.

[69] W. P. Dow, M. Y. Yen, S. Z. Liao, Y. Da Chiu, and H. C. Huang, ‘Filling mechanism in microvia metallization by copper electroplating’, *Electrochimica Acta*, vol. 53, no. 28, pp. 8228–8237, 2008.

[70] S. Q. Huang, K. C. Yung, and B. Sun, ‘A finite element model and experimental analysis of PTH reliability in rigid-flex printed circuits using the Taguchi method’, *International Journal of Fatigue*, vol. 40. pp. 84–96, 2012.

[71] R. Ghaffarian, ‘Reliability of PWB microvias for high density package assembly’, *International Journal of Materials and Structural Integrity*, vol. 2, no. 1/2, p. 47, 2008.

[72] R. Kisiel, ‘Polymers for electrical connections in printed circuit boards’, *Proceedings of SPIE*, vol. 6347, no. 63471U, 2006.

[73] R. Kisiel, J. Felba, J. Borecki, and A. Moscicki, ‘Problems of PCB microvias filling by conductive paste’, *Microelectronics Reliability*, vol. 47, no. 2–3. pp. 335–341, 2007.

[74] T. Falat, J. Felba, A. Moscicki, and J. Borecki, ‘Nano-silver inkjet printed interconnections through the microvias for flexible electronics’, in *Proceedings of the IEEE Conference on Nanotechnology*, 2011, pp. 473–477.

[75] L. Xie, M. Mäntysalo, A. L. Cabezas, Y. Feng, F. Jonsson, and L. R. Zheng, ‘Electrical performance and reliability evaluation of inkjet-printed Ag interconnections on paper substrates’, *Materials Letters*, vol. 88, pp. 68–72, 2012.

[76] J. W. Goodman, F. I. Leonberger, S. Y. Kung, and R. A. Athale, ‘Optical Interconnections for VLSI Systems’, *Proceedings of the IEEE*, vol. 72, no. 7, pp. 850–866, 1984.

[77] D. A. B. Miller, ‘Physical Reasons for Optical Interconnection’, *Journal of Optoelectronics*, vol. 11, pp. 155–168, 1997.

[78] J. Gourlay, M. Forbes, and M. Desmulliez, ‘Optically interconnected electronic chips: a tutorial and review of the technology’, *Electronics & Communication Engineering Journal*, vol. 13, no. 5, pp. 221–232, 2001.

[79] D. A. B. Miller, ‘Rationale and challenges for optical interconnects to electronic chips’, *Proceedings of the IEEE*, vol. 88, no. 6, pp. 728–749, 2000.

[80] D. a. B. Miller and H. M. Ozaktas, ‘Limit to the Bit-Rate Capacity of Electrical Interconnects from the Aspect Ratio of the System Architecture’, *Journal of Parallel and Distributed Computing*, vol. 41, no. 1, pp. 42–52, 1997.

[81] M. Horowitz, C. K. K. Yang, and S. Sidiropoulos, ‘High-speed electrical signaling: Overview and limitations’, *IEEE Micro*, vol. 18, no. 1. pp. 12–24, 1998.

[82] R. Tricker, *Optoelectronic and Fiber Optic Technology*. Newnes, 2002.

[83] ‘Guidelines On What Loss To Expect When Testing Fiber Optic Cables’. [Online]. Available: http://www.thefoa.org/tech/loss-est.htm. [Accessed: 01-Nov-2016].

[84] J. Hecht, *Understanding Fiber Optics*, 5th ed. Prentice Hall, 2005.

[85] J. M. Senior, *Optical Fiber Communications : Principles and Practice*, 3rd ed. Pearson, 2008.

[86] P. S. Guilfoyle, J. M. Hessenbruch, and R. V. Stone, 'Free-space interconnects for high-performance optoelectronic switching', *Computer*, vol. 31, no. 2, pp. 69–75, 1998.

[87] W. Gaberl and H. Zimmermann, 'Integrated optical receiver for lens-less free-space communication', in *European Conference on Optical Communication, ECOC*, 2008.

[88] G. Q. Li, D. W. Huang, E. Yuceturk, P. J. Marchand, S. C. Esener, V. H. Ozguz, and L. Yue, 'Three-dimensional optoelectronic stacked processor by use of free-space optical interconnection and three-dimensinoal VLSI chip stacks', *Applied Optics*, vol. 41, no. 2, pp. 348–360, 2002.

[89] S. Oktyabrsky, J. Castracane, and A. E. Kaloyeros, 'Emerging technologies for chip-level optical interconnects.', *Proceedings of SPIE*, vol. 4652, no. Optoelectronic Interconnects, Integrated Circuits, and Packaging, pp. 213–224, 2002.

[90] D. V. Plant and A. G. Kirk, 'Optical interconnects at the chip and board level: Challenges and solutions', *Proceedings of the IEEE*, vol. 88, no. 6, pp. 806–818, 2000.

[91] X. Zheng, P. J. Marchand, D. Huang, O. Kibar, and S. C. Esener, 'Cross talk and ghost talk in a microbeam free-space optical interconnect system with vertical-cavity surface-emitting lasers, microlenses, and metal-semiconductor-metal detectors', *Appl Opt*, vol. 39, no. 26, pp. 4834–4841, 2000.

[92] S. Pasricha and N. Dutt, 'Trends in Emerging On-Chip Interconnect Technologies', *Transactions on System Lsi Design Methodology*, vol. 1, pp. 2–17, 2008.

[93] T. Shibata, T. Makino, A. Takahahsi, Y. Matsuoka, and T. Sugawara, 'Optical waveguide materials with high thermal reliability and their applications for high-density optical interconnections', *2010 IEEE CPMT Symposium Japan, ICSJ10*. 2010.

[94] V. Francois and F. Laramee, 'Multicore fiber optimization for application to chip-to-chip optical interconnects', *Journal of Lightwave Technology*, vol. 31, no. 24, pp. 4022–4028, 2013.

[95] G. Kim, X. Han, and R. T. Chen, ‘Crosstalk and interconnection distance considerations for board-to-board optical interconnects using 2-D VCSEL and microlens array’, *IEEE Photonics Technology Letters*, vol. 12, no. 6, pp. 743–745, 2000.

[96] B. Jalali and S. Fathpour, ‘Silicon photonics’, *Journal of Lightwave Technology*, vol. 24, no. 12, pp. 4600–4615, 2006.

[97] F. X. Kärtner, S. Akiyama, G. Barbastathis, T. Barwicz, H. Byun, D. T. Danielson, F. Gan, F. Grawert, C. W. Holzwarth, J. L. Hoyt, E. P. Ippen, M. Kim, L. C. Kimerling, J. Liu, J. Michel, O. O. Olubuyide, J. S. Orcutt, M. Park, M. Perrott, M. a. Popovic, P. T. Rackich, R. J. Ram, H. I. Smith, and M. R. Watts, ‘Electronic photonic integrated circuits for high speed, high resolution, analog to digital conversion’, *Proceedings of SPIE*, vol. 6125, no. Silicon Photonics, pp. 203–205, 2006.

[98] J. Hankey, *Optical Data Communication*. PRIME Faraday Partnership, 2004.

[99] R. Zhang, J. C. Agar, and C. P. Wong, ‘Recent Advances on Electrically Conductive Adhesives’, *12th Electronics Packaging Technology Conference (EPTC)*, no. c. pp. 696–704, 2010.

[100] J. Liu, Z. Lai, H. Kristiansen, and C. Khoo, ‘Overview of conductive adhesive joining technology in electronics packaging applications’, *Proceedings of 3rd International Conference on Adhesive Joining and Coating Technology in Electronics Manufacturing 1998 (Cat. No.98EX180)*, pp. 1–18, 1998.

[101] J. E. Morris, ‘Isotropic conductive adhesives in electronics’, in *Advanced Adhesives in Electronics: Materials, Properties and Applications*, 2011, pp. 105–136.

[102] Y. Li, K. S. Moon, and C. P. Wong, ‘Stabilizing contact resistance of conductive adhesives on Sn surface by novel corrosion inhibitors’, *Proceedings of the International Symposium and Exhibition on Advanced Packaging Materials Processes, Properties and Interfaces*, vol. 2005. pp. 85–89, 2005.

[103] D. Lu, Q. K. Tong, and C. P. Wong, ‘Mechanisms underlying the unstable contact resistance of conductive adhesives’, *IEEE Transactions on Electronics Packaging Manufacturing*, vol. 22, no. 3, pp. 228–232, 1999.

[104] J. Liu, O. Salmela, J. Särkkä, J. E. Morris, P. E. Tegehall, and C. Andersson, *Reliability of microtechnology: Interconnects, devices and systems*. Springer, 2011.

[105] Q. K. Tong, S. A. Vona, R. Kuder, and D. Shenfeld, 'The Recent Advances in Surface Mount Conductive Adhesives', *Proceedings of 3rd international Conference on Adhesive Joining and Coating Technology in Electronics Manufacturing*, pp. 272–277, 1998.

[106] D. Lu and C. P. Wong, 'Development of solder replacement conductive adhesives with stable resistance and superior impact performance', *4th International Conference on Adhesive Joining and Coating Technology in Electronics Manufacturing, Proceedings - Presented at Adhesives in Electronics 2000*, pp. 110–116, 2000.

[107] U. Ali, K. J. B. A. Karim, and N. A. Buang, 'A Review of the Properties and Applications of Poly (Methyl Methacrylate) (PMMA)', *Polymer Reviews*, vol. 55, no. 4, pp. 678–705, 2015.

[108] C. a. Harper and E. M. Petrie, *Plastics materials and processes- A concise encyclopedia*, vol. 20, no. 3. 2003.

[109] D. W. Van Krevelen and K. Te Nijenhuis, *Properties of Polymers*, 4th ed. Elsevier, 2009.

[110] C. A. Haper, *Handbook of Plastics Processes*. Wiley-Interscience, 2006.

[111] L. Chang and E. M. Woo, 'Tacticity effects on glass transition and phase behavior in binary blends of poly(methyl methacrylate)s of three different configurations', *Polym. Chem.*, vol. 1, no. 2, pp. 198–202, 2010.

[112] D. Geschke, *Physical Properties of Polymers Handbook*, vol. 199, no. Part_1. Zeitschrift für Physikalische Chemie, 2007.

[113] H. P. A. Van Den Boom, W. Li, P. K. Van Bennekom, I. Tafur Monroy, and G. D. Khoe, 'High-capacity transmission over polymer optical fiber', *IEEE Journal on Selected Topics in Quantum Electronics*, vol. 7, no. 3, pp. 461–470, 2001.

[114] R. T. Schermer and J. H. Cole, 'Improved bend loss formula verified for optical fiber by simulation and experiment', *IEEE Journal of Quantum Electronics*, vol. 43, no. 10, pp. 899–909, 2007.

[115] Q. You, Y. Huang, and Y. Lin, ‘Polymer optical fiber large strain sensing technology’, *Proceedings of SPIE*, vol. 8199, p. 81991M–1, 2011.

[116] P. G. Laye, S. B. Warrington, T. M. Group, G. R. Heal, D. M. Price, and R. Wilson, *Principles of Thermal Analysis and Calorimetry*. The Royal Society of Chemistry, 2002.

[117] T. Hatakeyama and Z. Liu, *Handbook of thermal analysis*. Jonh Wiley & Sons Ltd., 1998.

[118] T. Hatakeyama and F. X. Quinn, *Thermal Analysis: Fundamentals and Applications to Polymer Science*, 2nd ed. Wiley, 1999.

[119] M. Mündlein and J. Nicolics, ‘Electrical resistance modeling of isotropically conductive adhesive joints’, *28th International Spring Seminar on Electronics Technology: Meeting the Challenges of Electronics Technology Progress, 2005*, vol. 2005. pp. 144–149, 2005.

[120] R. F. Saraf and J. M. Roldan, ‘Evaluation of Contact Resistance for Isotropic Electrically Conductive Adhesives’, *IEEE Transactions on Components Packaging and Manufacturing Technology Part B*, vol. 18, no. 2. pp. 299–304, 1995.

[121] P. J. Haines, ‘Principles of Thermal Analysis and Calorimetry (RSC Paperbacks)’, *Journal of Chemical Information and Modeling*, vol. 53, no. 9, pp. 55–92, 2002.

[122] ‘Silver (576832 ALDRICH)’. [Online]. Available: http://www.sigmaaldrich.com/catalog/product/aldrich/576832?lang=en&region=GB. [Accessed: 05-Jan-2016].

[123] ‘Poly(Bisphenol A-co-epichlorohydrin) (181196 ALDRICH)’. [Online]. Available: http://www.sigmaaldrich.com/catalog/product/aldrich/181196?lang=en&region=GB. [Accessed: 05-Jan-2016].

[124] ‘Triethylenetetramine (90460 ALDRICH)’. [Online]. Available: http://www.sigmaaldrich.com/catalog/product/aldrich/90460?lang=en&region=GB. [Accessed: 05-Jan-2016].

[125] ‘Specific Heat of common Substances’. [Online]. Available: http://www.engineeringtoolbox.com/specific-heat-capacity-d_391.html. [Accessed: 01-Nov-2016].

[126] I. M. Smallwood, *Handbook of Organic Solvent Properties*. Butterworth-Heinemann, 1996.

[127] Y. Zhang and S. Vyazovkin, 'Effect of substituents in aromatic amines on the activation energy of epoxy-amine reaction', *Journal of Physical Chemistry B*, vol. 111, no. 25, pp. 7098–7104, 2007.

[128] W. Zhao, Z. Zhang, Z. Sun, and D. Zhang, 'Cure kinetics of TGDDM/DDS system studied by non-isothermal method', *Acta Polymerica Sinica*, vol. 6, no. 4, pp. 564–568, 2010.

[129] J. . Lee, H. . Choi, M. . Shim, and S. . Kim, 'Kinetic studies of an epoxy cure reaction by isothermal DSC analysis', *Thermochimica Acta*, vol. 343, pp. 111–117, 2000.

[130] D. Rosu, C. N. Cascaval, F. Mustata, and C. Ciobanu, 'Cure Kinetics of Epoxy Resins Studied by Non-isothermal DSC Data', *Thermochimica Acta*, vol. 383, pp. 119–127, 2002.

[131] X. Jing, Y. Liu, Y. Liu, Z. Liu, and H. Tan, 'Toughening-modified epoxy-amine system: Cure kinetics, mechanical behavior, and shape memory performances', *Journal of Applied Polymer Science*, vol. 131, no. 19, pp. 1–7, 2014.

[132] Y. Cao, L. Zhou, X. Wang, X. Li, and X. Zeng, 'MicroPen direct-write deposition of polyimide', *Microelectronic Engineering*, vol. 86, no. 10, pp. 1989–1993, 2009.

[133] Australian Institute of Health and Welfare, *Cardiovascular disease: Australian facts 2011*. 2011.

[134] WHO, 'Good Health Adds Life to Years.Global brief for World Health Day 2012', *World Health Organization*, vol. 1, pp. 1–30, 2012.

[135] C. Robertson, *Printed Circuit Board Designer's Reference : Basics*. Prentice Hall, 2003.

[136] D. Brooks, *Signal Integrity Issues and Printed Circuit Board design*. Prentice Hall, 2003.

[137] E. P. Wood and K. L. Nimmo, 'In search of new lead-free electronic solders', *Journal of Electronic Materials*, vol. 23, no. 8. pp. 709–713, 1994.

[138] X. Zhang, S. Hu, C. Liu, V. Azorin-Peris, and R. Imms, ‘Electrically conductive adhesive enable to manufacture high performance patch probe for non-invasive physiological assessment’, *Electronic System-Integration Technology Conference (ESTC), 2012 4th*. pp. 1–4, 2012.

[139] A. Alzahrani, S. Hu, V. Azorin-Peris, R. Kalawsky, X. Zhang, and C. Liu, ‘A novel yet effective motion artefact reduction method for continuous physiological monitoring’, *Progress in Biomedical Optics and Imaging - Proceedings of SPIE*, vol. 8936, p. 89360G–89360G–16, 2014.

Appendices 1: Flow chart of the generation of spheres' locations

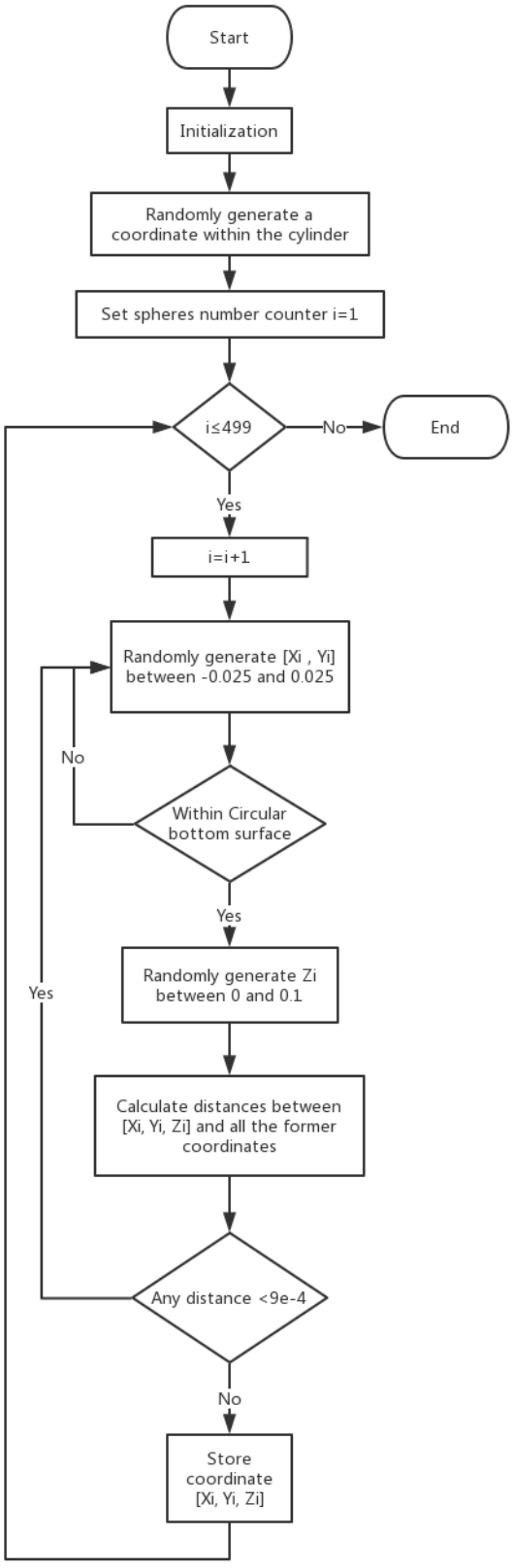

Appendices 2: Flow chart of the ICA via model generation

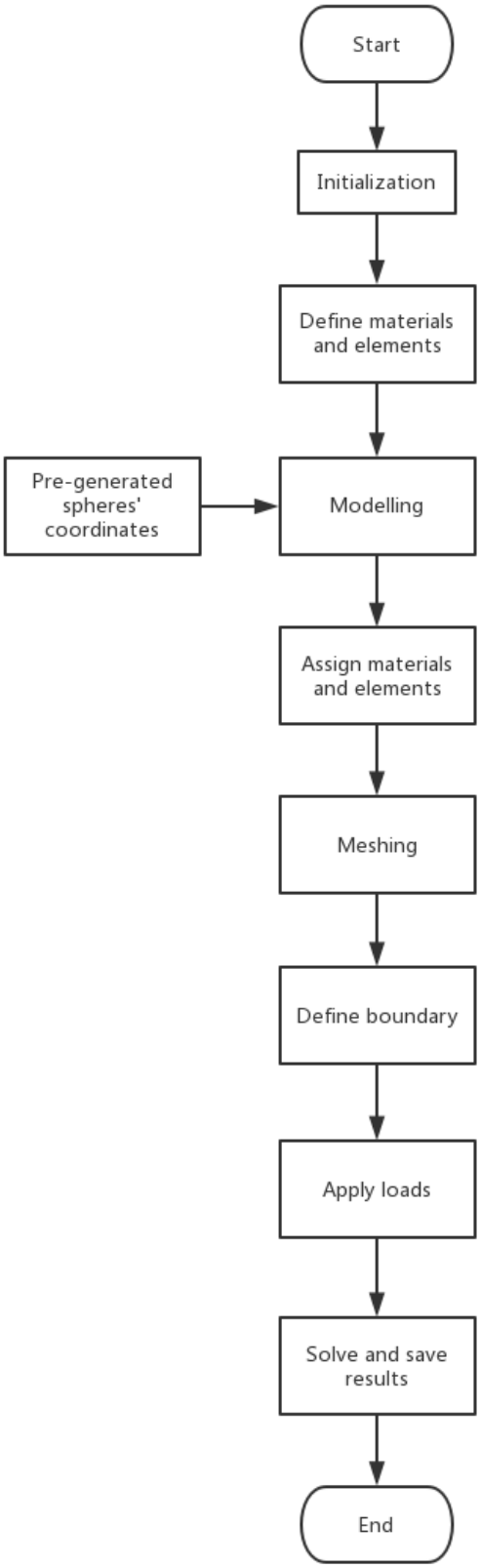

Appendices 3: Specifications of the ICA used in the work

CHEMTRONICS®
Technical Data Sheet **TDS # CW2400**

CircuitWorks® Conductive Epoxy

PRODUCT DESCRIPTION

CircuitWorks® Conductive Epoxy is a two part, silver epoxy used in prototype, repair and general conductive bonding applications. CW2400 features strong mechanical bonds, excellent electrical conductivity, and quick room temperature curing. CircuitWorks® Conductive Epoxy bonds aggressively to a wide variety of materials.

- Two-component product
- Simple mixing ratios
- Excellent electrical conductivity
- Fast curing
- High strength bond
- Bonds dissimilar surfaces
- Operating temperature range from
- -91°C (-131°F) to 100°C (212°F)

TYPICAL APPLICATIONS

CircuitWorks® Conductive Epoxy may be used for electronics applications including:

- Conductive Bonds Between Heat Sensitive Components
- Solderless Surface Mount Connections
- Circuit Board Trace Repair
- Static Discharge and Grounding
- Solder Repair
- Conductive Structural Adhesions

TYPICAL PRODUCT DATA AND PHYSICAL PROPERTIES

Composition		
Material	Part A Part B	Epoxy Hardener
Specific Gravity (Parts A & B Mixed)		2.85
Cured Compound		
Volume Resistivity		<0.001 ohm-cm
Thermal Conductivity		
Cal-cm/sec-cm^2 -°C		3.8 x 10^{-3}
BTU-in/hr-ft^2 -°F		11.0
W/m°K		1.6
Operating Temperature Range		-131 to 212°F (-91 to 100°C)
Lap Shear (ASTM D-1002)		>1200 lbs/in
Shore Hardness		>70
Adhesion		Excellent
Cured Flexibility		Excellent
Chemical Resistance		Excellent
Moisture Resistance		Good
Typical Thickness		5 mil
Shelflife		12 months
Conditions: Store at temperatures below 120° F		

COMPATIBILITY

CircuitWorks® Conductive Epoxy is generally compatible with most materials used in printed circuit board fabrication. As with any adhesive/sealant, compatibility with substrate should be determined on a non-critical area prior to use.

USAGE INSTRUCTIONS

Read MSDS carefully prior to use.

Cleaning: For best results, clean the board with one of Chemtronics® Electro-Wash® or Pow-R-Wash® cleaners in order to remove any surface contamination which may prevent adequate material contact.

Mixing: Mix equal amounts (1:1) by weight or volume of Part A and Part B. Mix thoroughly for 2 minutes and apply within 8 minutes.

Thinning: Do not attempt to thin.

Curing: Curing times and electrical conductivity depend primarily on temperature. For fastest curing times, maximum conductivity and adhesion, cure the bond between 150-250°F (65-121°C) for 5-10 minutes. CircuitWorks® Conductive Epoxy can be room temperature cured at or above 75°F (25°C), for 4 hours. Maximum conductivity and bond strength are achieved in 24 hours. *Curing at temperatures below 75°F (25°C) will result in a loss of conductivity and adhesion.*

Pot Life: 8-10 Minutes at 75°F (25°C) after mixing.

AVAILABILITY

CW2400	7g/ 0.25 oz. Adhesive & 7g/ 0.25 oz. Hardener

TECHNICAL & APPLICATION ASSISTANCE

Chemtronics® provides a technical hotline to answer your technical and application related questions. The toll free number is: **1-800-TECH-401.**

NOTE:

This information is believed to be accurate. It is intended for professional end users having the skills to evaluate and use the data properly. CHEMTRONICS® does not guarantee the accuracy of the data and assumes no liability in connection with damages incurred while using it.

MANUFACTURED BY:

ITW CHEMTRONICS®
8125 COBB CENTER DRIVE
KENNESAW, GA 30152
1-770-424-4888

REV. F (04/06)

DISTRIBUTED BY:

Conforms to Regulation (EC) No. 1907/2006 (REACH), Annex II - Europe

SAFETY DATA SHEET

Conductive Epoxy - Part A

1. IDENTIFICATION OF THE SUBSTANCE/MIXTURE AND OF THE COMPANY/UNDERTAKING

Identification of the substance or mixture

Product name : Conductive Epoxy - Part A

Chemical name : CW2400-A

Synonyms : Conductive Epoxy - Part A

Product type : Solid.

Use of the substance/mixture : Adhesives

Company/undertaking identification

Manufacturer : ITW Chemtronics
8125 Cobb Center Drive
Kennesaw, GA 30152

Tel. 770-424-4888 or toll free 800-645-5244

Distributor :

Importer : ITW Contamination Control BV
Saffierlaan 5
VZ-2132 Hoofddorp
The Netherlands

Email: info@itw-cc.com

Tel: +31 88 1307 400
FAX: +31 88 1307 499

e-mail address of person responsible for this SDS : askchemtronics@chemtronics.com

Emergency telephone number (with hours of operation) : Chemtrec - 1-800-424-9300 or collect 703-527-3887

2. HAZARDS IDENTIFICATION

The product is classified as dangerous according to Directive 1999/45/EC and its amendments.

Classification : Xi; R36/38
R43
N; R50/53

Human health hazards : Irritating to eyes and skin. May cause sensitisation by skin contact.

Environmental hazards : Very toxic to aquatic organisms, may cause long-term adverse effects in the aquatic environment.

See Section 11 for more detailed information on health effects and symptoms.

3. COMPOSITION/INFORMATION ON INGREDIENTS

Substance/preparation : Mixture

Ingredient name	CAS number	%	EC number	Classification	
silver	7440-22-4	60 - 90	231-131-3	N; R50	[1] [2]
reaction product: bisphenol-A-(epichlorhydrin); epoxy resin (number average molecular weight ≤ 700)	25068-38-6	10 - 25	500-033-5	Xi; R36/38 R43 N; R51/53	[1]
See Section 16 for the full text of the R-phrases declared above.					

There are no additional ingredients present which, within the current knowledge of the supplier and in the concentrations applicable, are classified as hazardous to health or the environment and hence require reporting in this section.

[1] Substance classified with a health or environmental hazard

[2] Substance with a workplace exposure limit

Conforms to Regulation (EC) No. 1907/2006 (REACH), Annex II - Europe

SAFETY DATA SHEET

Conductive Epoxy - CW2400-B

1. IDENTIFICATION OF THE SUBSTANCE/MIXTURE AND OF THE COMPANY/UNDERTAKING

Identification of the substance or mixture

Product name : Conductive Epoxy - CW2400-B

Chemical name : CW2400-B

Synonyms : Conductive Epoxy - Part B

Product type : Solid.

Use of the substance/mixture : Adhesives

Company/undertaking identification

Manufacturer : ITW Chemtronics
8125 Cobb Center Drive
Kennesaw, GA 30152

Tel. 770-424-4888 or toll free 800-645-5244

Distributor :

Importer : ITW Contamination Control BV
Saffierlaan 5
VZ-2132 Hoofddorp
The Netherlands

Email: info@itw-cc.com

Tel: +31 88 1307 400
FAX: +31 88 1307 499

e-mail address of person responsible for this SDS : askchemtronics@chemtronics.com

Emergency telephone number (with hours of operation) : Chemtrec - 1-800-424-9300 or collect 703-527-3887

2. HAZARDS IDENTIFICATION

The product is classified as dangerous according to Directive 1999/45/EC and its amendments.

Classification : C; R34
R43
N; R50

Human health hazards : Causes burns. May cause sensitisation by skin contact.

Environmental hazards : Very toxic to aquatic organisms.

See Section 11 for more detailed information on health effects and symptoms.

3. COMPOSITION/INFORMATION ON INGREDIENTS

Substance/preparation : Mixture

Ingredient name	CAS number	%	EC number	Classification	
silver	7440-22-4	60 - 90	231-131-3	N; R50	[1] [2]
2-piperazin-1-ylethylamine	140-31-8	10 - 25	205-411-0	Xn; R21/22 C; R34 R43 R52/53	[1]
See Section 16 for the full text of the R-phrases declared above.					

There are no additional ingredients present which, within the current knowledge of the supplier and in the concentrations applicable, are classified as hazardous to health or the environment and hence require reporting in this section.

[1] Substance classified with a health or environmental hazard

[2] Substance with a workplace exposure limit